Dissertation
submitted to the
Combined Faculties for the Natural Sciences
and for Mathematics
of the Ruperto-Carola University of Heidelberg, Germany
for the degree of
Doctor of Natural Sciences

presented by
Dipl.-Phys. Marc Schumann
born in Göppingen

Oral examination: May 9th, 2007

Measurement of Neutrino and Proton Asymmetry in the Decay of polarized Neutrons
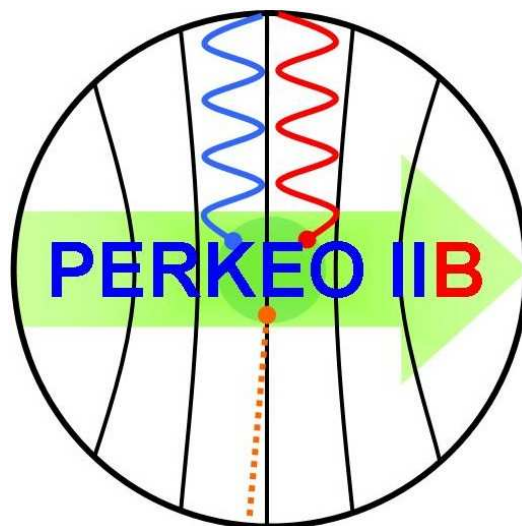
Referees: Prof. Dr. Hartmut Abele
              Prof. Dr. Karlheinz Meier

Measurement of Neutrino and Proton Asymmetry in the Decay of polarized Neutrons

The Standard Model of Particle Physics is in excellent agreement with all experimental results. However, it is not believed to be the most fundamental theory. It requires, for example, too many free parameters and is not able to explain the existence of effects such as parity-violation or CP-violation. Thus measurements have to be performed to probe the Standard Model and to search for "new physics". An ideal laboratory for this is the decay of the free polarized neutron.

In this thesis, we present measurements of the neutrino asymmetry B and the proton asymmetry C in neutron decay. These coefficients describe the correlation between neutron spin and momentum of the respective particle, and provide detailed information on the structure of the underlying theory. The experiment was performed using the electron spectrometer PERKEO II installed at the Institut Laue-Langevin (ILL). It was equipped with a combined electron-proton detector to reconstruct the neutrino in a coincidence measurement.

The uncertainty of our neutrino asymmetry result, $B = 0.9802(50)$, is comparable to the present best measurement, and, for the first time ever, we obtained a precise value for the proton asymmetry, $C = -0.2377(36)$. Both results are used to analyze neutron decay for hints on "Physics beyond the Standard Model" by studying possible admixtures of right-handed currents and of scalar and tensor couplings to the interaction.

Messung der Neutrino- und Proton-Asymmetrie im Zerfall polarisierter Neutronen

Das Standardmodell der Teilchenphysik liefert eine hervorragende Beschreibung für alle experimentellen Beobachtungen. Dennoch geht man davon aus, dass es nicht die fundamentale Theorie der Teilchenphysik ist, unter anderem da es sehr viele freie Parameter benötigt und keine Begründung für Phänomene wie etwa Paritäts- oder CP-Verletzung liefert. Daher wird es ständig experimentellen Tests unterzogen, in denen auch nach "Physik jenseits des Standardmodells" gesucht wird. Hierzu bietet der Zerfall freier, polarisierter Neutronen ideale Rahmenbedingungen.

In dieser Arbeit wird eine Messung der Neutrino-Asymmetrie B und der Proton-Asymmetrie C im Neutronenzerfall vorgestellt. Diese beschreiben Korrelationen zwischen dem Neutronenspin und dem Impuls des jeweiligen Teilchens und können präzise Informationen über die Struktur der schwachen Wechselwirkung liefern. Das Experiment wurde mit dem Elektronen-Spektrometer PERKEO II am Institut Laue-Langevin (ILL) durchgeführt. Um das Neutrino aus einer koinzidenten Messung von Elektron und Proton zu rekonstruieren, wurde ein kombinierter Elektron-Proton-Detektor verwendet.

Das Ergebnis der Neutrino-Asymmetrie $B = 0.9802(50)$ hat eine Genauigkeit, die mit der bislang besten Messung vergleichbar ist. Weiterhin ist im Rahmen dieser Arbeit die erste Präzisionsmessung der Proton-Asymmetrie gelungen, das Resultat ist $C = -0.2377(36)$. Beide Werte werden verwendet, um den Neutronenzerfall nach Hinweisen auf "neue Physik" zu untersuchen. Das Hauptaugenmerk liegt dabei auf rechtshändigen Strömen und neuen Kopplungen.

Contents

Chapter 1

Introduction

"Experiments in [...] β decay have significantly contributed in the past to the determination of basic aspects of the weak interaction. They continue to be a powerful tool to test the underlying symmetries, to determine the structure in more detail, and to search for physics beyond the standard model."

N. Severijns et al. [Sev06]

Usually, elementary particle physics is considered to be a synonym for high energy physics, and now, at the beginning of the year 2007, the physics community yearns for the start of the Large Hadron Collider (LHC) at CERN. Four experiments are dedicated to study nature at the highest available energies. They should find the Higgs-boson – the missing part of the Standard Model of particle physics – and hopefully also new (supersymmetric?) particles. Once these particles are detected, they should be examined precisely with the planned International Linear Collider (ILC). In this giant instrument of about 40 km length, electrons and positrons will collide at center of mass energies of $500-1000$ GeV.

However, particle physics can also be done at much lower energies. No new particles will be found here, but low energy experiments are an ideal suited environment to do precision physics. Significant contributions to the knowledge about the structure of weak interactions and the role of the underlying symmetries have been determined from experiments studying β-decay. And when experimental results of very precise measurements differ from Standard Model expectations, this may suggest evidence for new physics, i.e. physics that is not described by the Standard Model. The expected effects are tiny but they are accessible due to the high precision achievable at low energies.

The subject of this thesis is a precision experiment in low energy particle physics: We measured emission anisotropies of decay products in the decay of free polarized neutrons, in particular the so-called neutrino asymmetry B and the proton asymmetry C. These are correlations between neutron spin and momentum of the respective particles. In combination with other parameters, these quantities can be used to study fundamental properties of the electroweak interaction, such as the origin of parity violation or the general structure of the weak Lagrangian.

We used Heidelberg's electron spectrometer PERKEO II for the experiment. Compared to the high energy physics instruments mentioned above, this is a rather small device, however, it constitutes probably one of the largest mobile experiments at all. Although it has an overall weight of almost 20 tons, it was regularly moved to the Institut Laue-Langevin (ILL) that operates one of the largest scientific neutron sources in the world. Here, in Grenoble (France), the measurement of the asymmetries was performed in summer 2004.

Neutrons are mostly used to obtain information about materials in scattering experiments, especially for samples where synchrotron light is not applicable. Hence it is not surprising, that the vast majority of experiments conducted at the ILL are related to solid state physics, material science, but also chemistry and biology. Only a small scientific community studies the neutron itself and tries to answer basic questions in particle physics via precision measurements. PERKEO IIB, the experiment described in this thesis, is an excellent example for this.

In the experiment, it was neccessary to detect electrons and protons in coincidence to reconstruct the neutrino. We had the possibility to measure altogether eight electron spectra generated with different conditions on the emission direction of the charged particles with respect to the neutron spin, and on the detector giving the first trigger signal. These spectra provide many different informations and can be analyzed in several ways to obtain the neutrino asymmetry B and the proton asymmetry C.

The experimental setup and the measurements will be described extensively in chapter 3, followed by data analysis in chapter 4, where we also present the results for the asymmetries. Implications following from these and the analysis regarding new physics can be found in chapter 5, followed by a summary and a brief look into PERKEO's future. Some impressions of the experiment PERKEO IIB are shown at the end of the thesis, on page 123. First of all, we will give an introduction to the weak interaction at low energies and to possible extensions of the Standard Model in the following chapter.

Chapter 2

The Weak Interaction in the Standard Model

The decay of the free neutron into electron, proton, and anti-neutrino

$$n \rightarrow e^- + p + \bar{\nu}_e \tag{2.1}$$

is probably the best-known example of a weak semi-leptonic decay. In this chapter, we will give a brief introduction into the theory of weak interactions as described within the Standard Model of Particle Physics. However, limits of this model and possible extensions will be also mentioned, in particular left-right symmetric models.

The main part of the chapter covers the theory of neutron decay relevant to the measurement that was performed within the framework of this thesis.

2.1 Weak Interaction and Neutron Decay

Standard Model of Particle Physics: In the 1860s, Maxwell realized that electric and magnetic forces have the same origin; the so-called Maxwell Equations are the basic equations of the unified theory of electromagnetism. 100 years later, Weinberg and Salam were able to show that electromagnetic and weak interactions of leptons could be regared as manifestations of a single *electroweak* interaction; Glashow then managed to extent this theory to the hadronic sector. Just as in QED (quantum electrodynamics), the field theoretical formulation of relativistic quantum mechanics, this new theory - called QFD (quantum flavor dynamics) - is based on the request of local gauge invariance of the Dirac spinor. This automatically leads to the existence of vector fields that couple to the spinor. The corresponding particles are the gauge bosons γ, W^+, W^-, and Z^0.

Together with the theory of strong interactions, quantum chromodynamics (QCD), QFD constitutes the so-called Standard Model of Particle Physics. It is based on the gauge group

$$\text{SU}(2)_L \;\otimes\; \text{U}(1) \;\otimes\; \text{SU}(3)_c \tag{2.2}$$

and describes the weak, electromagetic, and strong interaction of the six leptons

$$\begin{pmatrix} \nu_e \\ e^- \end{pmatrix}, \quad \begin{pmatrix} \nu_\mu \\ \mu_- \end{pmatrix}, \quad \begin{pmatrix} \nu_\tau \\ \tau_- \end{pmatrix}, \tag{2.3}$$

and six quarks

$$\begin{pmatrix} u \\ d \end{pmatrix}, \qquad \begin{pmatrix} c \\ s \end{pmatrix}, \qquad \begin{pmatrix} t \\ b \end{pmatrix} \tag{2.4}$$

by exchange of the four electroweak gauge bosons mentioned above and eight additional QCD gluons g^α.

Weak Interaction: We will now focus on the weak interaction, the only force that is not flavor invariant, i.e. that can change quark flavors. We distinguish interactions mediated by weak neutral currents, corresponding to the exchange of a Z^0-boson, and charged current interactions. In the latter, a W^+ or W^- boson is exchanged and the charge of the initial state changes by one elementary charge e. Neutron decay, where - on the quark level - a down-quark ($q_d = -\frac{1}{3}$) is transformed into an up-quark ($q_u = +\frac{2}{3}$), is governed by the charged current.

Parity Violation: In the year 1956, Lee and Yang [Lee56] realized that the weak interactions is not neccessarily invariant under parity transformation

$$P : (t, \mathbf{r}) \ \rightarrow (t, -\mathbf{r}) \tag{2.5}$$

describing a reflection of the spatial coordinates at the origin. In 1957, Wu [Wu57] experimentally confirmed this parity violation in the decay of polarized ^{60}Co

$$^{60}\text{Co} \ \rightarrow \ ^{60}\text{Ni} + e^- + \overline{\nu}_e \tag{2.6}$$
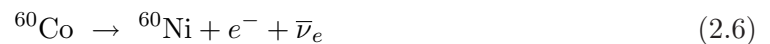
by measuring an anisotropy in the electron emission direction. The PERKEO experiment described in this thesis is in some sense a modern and very precise version of the Wu-experiment for neutrons.

All experimental results on parity violation indicate that (massless) neutrinos are always left-handed, i.e. that their spin is aligned antiparallel to their momentum, their helicity is $H = -1$. Anti-neutrinos found in β^--decays are always right-handed. Nowadays, it is known from the observation of neutrino oscillations that neutrinos must have a mass. But at least the electron neutrino seems to be very light, and the assumption of a masseless neutrino works quite well. The massive leptons (e^-, μ^-, τ^-) are also left-handed, however, their helicity is only $H = -\frac{v}{c}$ as one can always find a frame of reference moving faster than the particle itself. To account for the experimental results, maximal parity violation is included in the Standard Model of weak interactions: Massless leptons are always left-handed.

In 1964, not even ten years after the discovery of parity violation, Christensen et al. found experimentally that also CP, the combination of a parity P and a charge conjugation $C : q \rightarrow -q$ transformation, is violated in weak K-decays [Chr64]. However, the combination CPT including additionally the time reversal transformation $T : (t, \mathbf{r}) \rightarrow (-t, \mathbf{r})$ must be a symmetry in a Lorentz invariant field theory with arbitrary interactions [Lue54]. Thus time reversal T must also be violated in weak interactions since CP violation has been observed and evidence for T non-invariance was found in the neutral kaon system [Ang98].
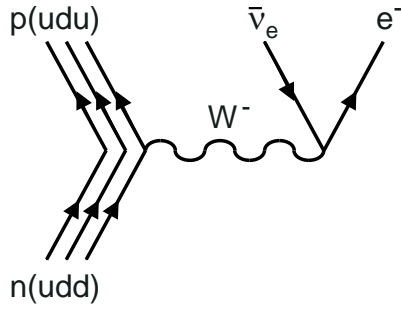
Figure 2.1: Feynman diagram of neutron β-decay: On the quark level, a down quark decays into an up quark; the interaction is mediated by a charged W-boson.
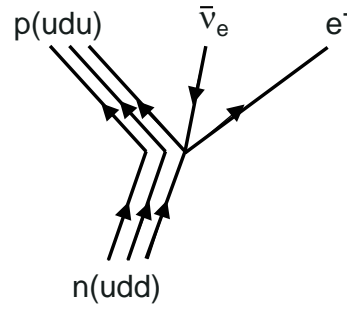
Figure 2.2: In the low energy limit, the W-boson mass in the propagator dominates the momentum tranfer q, and the interaction can be described as a four-fermion point interaction.

From the Feynman Diagram to V−A Theory: From the Feynman diagram describing neutron decay (figure 2.1) one can calculate the transition matrix matrix

$$T_{fi} = -\frac{g^2}{2}\,\bar{e}\gamma^\mu\,\frac{1-\gamma^5}{2}\,\nu_e\,\left(\frac{-g_{\mu\nu}+q_\mu q_\nu m_W^{-2}}{q^2-m_W^2}\right)\,\langle p|\bar{u}\gamma^\nu\,\frac{1-\gamma^5}{2}\,d|n\rangle \tag{2.7}$$

where e, ν_e, p, n, u, and d denote the Dirac spinors af the respective particles, m_W is the W-boson mass, g the weak coupling constant, $g_{\mu\nu}$ the metric tensor, and q the momentum transfer. The hadronic part is written in bra-ket notation to account for hadronic structure.

Maximal parity violation is included in the theory using the projection operator $h = \frac{1}{2}(1-\gamma^5)$. The application of h to a spinor ψ yields only the left-handed part ψ_L of the field:

$$\psi_L = h\psi = \frac{1-\gamma^5}{2}\,\psi. \tag{2.8}$$

In the limit of massless particles, only the left-handed $\mathrm{SU}(2)_L$ doublets

$$\begin{pmatrix}\nu_e\\e_L\end{pmatrix},\quad\begin{pmatrix}\nu_\mu\\\mu_L\end{pmatrix},\quad\begin{pmatrix}\nu_\tau\\\tau_L\end{pmatrix},\quad\begin{pmatrix}u_L\\d_L\end{pmatrix},\quad\begin{pmatrix}c_L\\s_L\end{pmatrix},\quad\text{and}\quad\begin{pmatrix}t_L\\b_L\end{pmatrix} \tag{2.9}$$

participate in the interaction, the right handed particles are singlets under $\mathrm{SU}(2)_L$ transformations and do not interact weakly at all.

Due to the high W-boson mass $m_W = 80.4$ GeV, and the rather low momentum transfer q given by the mass difference between neutron and proton, we have $|q^2| \ll m_W^2$, and equation (2.7) can be simplified to

$$T_{fi} = -\frac{g^2}{8m_W^2}\,\bar{e}\gamma^\mu(1-\gamma^5)\nu_e\,\langle p|\bar{u}\gamma_\mu(1-\gamma^5)d|n\rangle. \tag{2.10}$$

This corresponds to Feynman graph 2.2, a four-fermion-coupling where the two vertices coincide and the four fermion lines meet in one point; the coupling constant in this case is $G_F/\sqrt{2}$, where G_F is the Fermi constant. By comparing the constants one gets the relation

$$\frac{g^2}{8m_W^2} = \frac{G_F}{\sqrt{2}} = \frac{1.16\cdot10^{-5}\text{ GeV}^2}{\sqrt{2}}. \tag{2.11}$$

The reason for the "weakness" of the weak interaction is not due to a small coupling constant g, which is of the order of magnitude of the electromagnetic coupling e, but due to the high mass m_W in the denominator.

Equation (2.10) provides a perfect description of all weak processes at low energies and is also referred to as $V - A$ formulation of β-decay: The vector part (γ^μ) in the matrix element has the same size as the axial-vector part $(-\gamma^\mu\gamma^5)$ but an opposite sign.

To account for processes like strangeness violating decays, i.e. decays between the three quark families, and to preserve universality, the quark fields d, s, and b have to be replaced by the weak eigenstates d', s', b' that are linear combinations of the mass eigenstates:

$$\begin{pmatrix} d' \\ s' \\ b' \end{pmatrix} = \begin{pmatrix} V_{ud} & V_{us} & V_{ub} \\ V_{cd} & V_{cs} & V_{cb} \\ V_{td} & V_{ts} & V_{tb} \end{pmatrix} \begin{pmatrix} d \\ s \\ b \end{pmatrix}. \tag{2.12}$$

The transformation between the two bases is achieved with the unitary 3×3 quark mixing matrix (CKM-matrix[1]) V.

If we separate the matrix element between the nucleon states into a vector and an axial-vector part to account for hadronic structure (assuming exact isospin invariance of the strong interaction, i.e. $m_n = m_p$)

$$\langle p|\overline{u}\gamma_\mu(1-\gamma^5)d|n\rangle = \langle p|\overline{u}\gamma_\mu d|n\rangle - \langle p|\overline{u}\gamma_\mu\gamma^5 d|n\rangle = g_V\ \overline{p}\gamma_\mu n + g_A\ \overline{p}\gamma_\mu\gamma^5 n, \tag{2.13}$$

and include quark mixing, the full transition matrix of neutron decay reads:

$$T_{fi} = -\frac{G_F}{\sqrt{2}}\ V_{ud}\ \overline{e}\gamma^\mu(1-\gamma^5)\nu_e\ \overline{p}\gamma_\mu\left(1+\frac{g_A}{g_V}\gamma^5\right)n. \tag{2.14}$$

The ratio of axial-vector g_A to vector coupling constant g_V is often denoted by

$$\lambda = \frac{g_A}{g_V}. \tag{2.15}$$

Most General Description of Weak Interaction: We conclude that the weak interaction in neutron decay and at low energies in general can be perfectly described by a four-fermion point interaction. The currents show a $V - A$ structure that was first proposed by Feynman and Gell-Mann [Fey58].

However, if we only assume Lorentz-invariance and (for simplicity) only linear couplings, the most general Lagrangian reads

$$\mathcal{L} = \sum_k (\overline{p}\Omega_k n)\ (\overline{e}\Omega_k(g_k + g_k'\gamma^5)\nu_e) + \text{h.c.}, \tag{2.16}$$

where the operator Ω_k describes the type of interaction: Scalar $\Omega_S = 1$, vector $\Omega_V = \gamma^\mu$, tensor $\Omega_T = \sigma^{\mu\nu}/\sqrt{2} = -i\ 2^{-\frac{3}{2}}(\gamma^\mu\gamma^\nu - \gamma^\nu\gamma^\mu)$, axial-vector $\Omega_A = \gamma^\mu\gamma^5$, and pseudo-scalar $\Omega_P = \gamma^5$. The coefficients g_k, g_k' determine its relative strength. Which interactions are actually realized in nature cannot be concluded from the spectral shape or life time τ of a weak process. Additional information is needed, and very important experiments for this purpose are measurements of angular distributions in the decay of a particle, the topic of this thesis. However, up to now no deviations from the $V - A$ structure have been found [Sev06].

---

[1]Cabbibo-Kobayashi-Maskawa-matrix

2.2   Limits of the Standard Model

The Standard Model of electroweak interactions, whose low-energy description of the weak force was introduced in the last section, is a well established theory. It had some great successes by predicting the existence of formerly unknown particles (e.g. Z^0, top-quark), and up to now no experiment is known that cannot be explained within this model. (To some extent with slight adjustments as in case of the finite neutrino masses and lepton number non-conservation known from neutrino oscillation experiments.) However, scientists do not assume it to be the "final" theory of particle physics since it is unsatisfactory in many aspects:

- It has a vast amount of free parameters: The "original" standard model needs 18 parameters to describe interactions and observed masses, seven more are neccessary to account for massive neutrinos. Although it is unlikely (but not undesirable) that the next generation of theories will predict all particle masses, they should at least reduce the number of coupling constants.

- There are two separate theories covering electroweak and strong processes. Gravity, the fourth fundamental interaction, is not included in the Standard Model at all.

- There is no intrinsic motivation for the left-handedness of the weak interaction leading to parity violation. The origin of CP-violation remains unclear, too.

- The Standard Model gives no explanation for the existence of the three generations of quarks and leptons. Another property not understood is the equality of proton and electron absolute charge; the deviation being smaller than $1.0 \cdot 10^{-21}$ [PDG06].

- Finally there is a cosmological reason: We know the matter content of the universe from nuclear synthesis and very precisely from the WMAP observation of the cosmic microwave background [Spe06]. Less that 5 % are due to baryonic matter as described within the Standard Model. There is neither an explanation for the additional 20 % of dark matter nor for the remanining dark energy.

Therefore the Standard Model is constantly tested experimentally, and searches for "Physics beyond the Standard Model" are very important to obtain a starting-point to approach the problems mentioned above. Many theoretical extensions have been proposed, some of them will be sketched in the following sections. In doing so, we will focus on left-right symmetric models that address the question of the origin of parity violation. A measurement of the neutrino asymmetry B in neutron decay, as described in this thesis, is very sensitive to possible right-handed currents.

2.2.1   Grand Unified Theories and Supersymmetry

The three interactions included in the Standard Model have three coupling constants, the fine structure constant α_{em}, the strong coupling constant α_s, and the Fermi-constant G_F (cf. equation 2.11)[2]. After electroweak unification at energies $m_Z \approx 10^2$ GeV, we still have three coupling constants α_s, g and g', where the latter two are linked by the Weinberg-angle

---

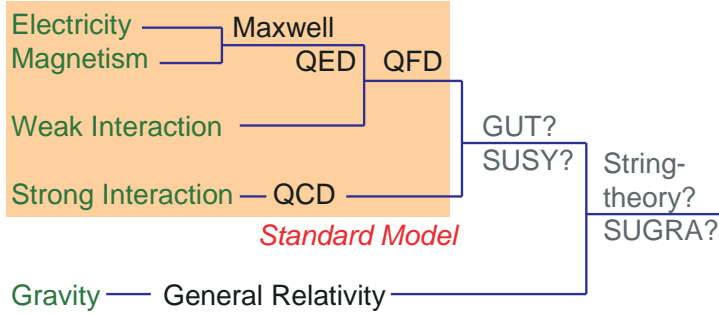[2]In this overview, we closely follow [Gro90].

Figure 2.3: The figure illustrates the unification of the fundamental interactions: The shaded region - before the unification of electroweak and strong interaction - is referred to as the Standard Model. Possible extensions including QCD are Grand Unified Theories (GUTs), Supersymmetry, or String Theory. (Figure based on [Gro90]).

θ_W. Thus, the overall number of parameters has not decreased. Only the explanation of all interactions based on gauge invariance with respect to a *simple* group G leads to a single coupling constant. A simple group G cannot be written as a direct product of two subgroups, as it is the case in QFD

$$G_{\mathrm{QFD}} = \mathrm{SU}(2)_L \otimes \mathrm{U}(1), \tag{2.17}$$

where we still have two couplings.

To reduce the number of free parameters by unification of electroweak theory and QCD (cf. figure 2.3), one therefore has to look for a simple group G with

$$G \supset \mathrm{SU}(2)_L \otimes \mathrm{U}(1) \otimes \mathrm{SU}(3)_c \tag{2.18}$$

since the new theory has to include the Standard Model. The smallest group satisfying this condition is SU(5), the so-called "Minimal Solution" of a Grand Unifying Theory (GUT): To obtain three different interactions from a fundamental simple group G, the corresponding symmetry must be spontaneously broken at a mass scale $m_X \approx 10^{15}$ GeV. Above this energy, only one interaction mediated by "X-bosons" exists, and after symmetry breaking the gauge bosons of the Standard Model occur:

$$G \xrightarrow{m_X} \mathrm{SU}(3)_c \otimes \mathrm{SU}(2)_L \otimes \mathrm{U}(1) \xrightarrow{m_Z} \mathrm{SU}(3)_c \otimes \mathrm{U}(1)_{em} \tag{2.19}$$

An implication of this scenario is that the coupling constants $g_s(q^2)$, $g(q^2)$, and $g'(q^2)$, depending on momentum tranfer q, have to coincide at m_X.

At first, the simple SU(5)-GUT was quite successful since it managed to explain some points in the list given above: It unified all three interactions, was able to calculate the Weinberg-angle θ_W, and explained the equality of electron and proton charge in a natural way. In SU(5), however, there are still almost 20 free parameters, neither the origin of parity violation is explained nor the existence of the three quarks and lepton generations, and gravity is again not included. On the experimental side, the model predicts the proton to decay via X-boson emission in positron and pion,

$$p \xrightarrow{X} e^+ + \pi^0, \tag{2.20}$$

with a lifetime of $\tau_{\mathrm{GUT}} \approx 10^{30}$ years. However, the actual limit is already two orders of magnitude larger: $\tau_p > 1.6 \cdot 10^{32}$ years [PDG06]. Therefore the simple SU(5) model seems to be refuted and more complicated extensions had to be conceived.

SO(10) with Intermediate Symmetries: The next simple group including SU(5) as subgroup is SO(10). Now, there may be intermediate symmetries for energies $M > m_X$, and many possible models based on this approach exist. In these, neutrinos appear as massive particles (as found in the oscillation experiments), and the proton lifetime can be longer. Furthermore, the existence of intermediate symmetries, i.e. more than one symmetry breaking from SO(10) to the observed $SU(3)_c \otimes SU(2)_L \otimes U(1)$, allows that the three coupling constants do not coincide at one particular energy m_X [Fuk03].

Among the most prominent theories based on SO(10) are the so-called Left-Right-Symmetric models [Pat74, Moh75]: At energy $M > m_X$, these break down the symmetry group into an "extended color" (EC) group, identifying the leptons as fourth color charge, and a left-handed and a right-handed SU(2) group:

$$\mathrm{SO}(10) \xrightarrow{M} \mathrm{SU}(4)_{EC} \otimes \mathrm{SU}(2)_L \otimes \mathrm{SU}(2)_R \xrightarrow{m_{W_R}} \mathrm{SU}(3)_c \otimes \mathrm{SU}(2)_L \otimes \mathrm{U}(1) \xrightarrow{m_{W_L} \approx m_Z} \cdots . \quad (2.21)$$

The interaction corresponding to $SU(2)_R$ is mediated by heavy right-handed W_R-bosons; at its mass scale m_{W_R}, symmetry is again spontaneously broken into the Standard Model groups. This model will be discussed in more detail in section 2.2.2.

Supersymmetry (SUSY):   The alternative to SO(10) is the introduction of supersymmetry into SU(5), generating a symmetry between fermions and bosons by arranging them in "supermultipletts". To do so, a "superpartner" has to be introduced for every particle; unfortunately none of the known particles can be linked together, so many new particles have to be invented: For example six spin-0 squarks as superpartners for the quarks and spin-$\frac{1}{2}$ bosinos for the bosons. Until now, no new SUSY-particles were detected, but maybe the neccessary energies will be reached in the LHC (CERN). In exact supersymmetry, the masses of particle and sparticle would be degenerate. Since this is not the case, SUSY is broken at the mass scale m_{SUSY}; this scale, however, is not predicted by the theory itself.

In general, supersymmetry can explain the coarse structure in the particle mass spectrum and yields a longer proton lifetime. There are many SUSY versions, amongst others local SUSY models that intrinsically include gravity (SUGRA), and supersymmetric left-right models based on the group

$$\mathrm{SU}(3)_c \otimes \mathrm{SU}(2)_L \otimes \mathrm{SU}(2)_R \mathrm{U}(1)_{\mathrm{BL}}, \quad (2.22)$$

where BL denotes baryon-lepton symmetry [Aul97].

2.2.2   Left-Right Symmetric Models

It is assumed that the universe was in a left-right symmetric state at the high energies just after the big bang. The Standard Model, valid at much lower energies, is not left-right symmetric at all and provides no information on the origin of parity violation.

This was one of the reasons to develop the so-called left-right symmetric models [Pat74, Moh75]: They assume that parity is an exact symmetry of the weak interaction Lagrangian above an energy m_{W_R} that is much larger than the electroweak breaking scale m_Z. A left- and a right-handed group SU(2) are spontaneously broken into the well-known $SU(2)_L \otimes U(1)$ when temperature drops below m_{W_R} due to the cooling of the expanding universe.

Analogous to mass generation in the Higgs-mechanism, parity violation can now be explained as a consequence of spontaneous symmetry breaking in a transition to lower energies. Below m_{W_R}, weak interaction is mediated by the "normal" $W_L^{\pm}$-bosons that only couple to the left-handed particle doublets, however, there should be additional bosons $W_R^{\pm}$, remnants from the right-handed $SU(2)_R$ group. The model also requires massive right-handed neutrinos as needed in the "seesaw-mechanism" to explain the smallness of the neutrino masses.

Manifest Left-Right Symmetry: Left- and right-handed coupling constants are assumed to be equal in the manifest left-right symmetric model [Beg77], $g'^L_V = g'^R_V$, $g'^L_A = g'^R_A$, the same holds for quark mixing. In left-right symmetric theories considering a minimal Higgs sector, with only one complex Higgs doublet and a single physical Higgs boson, manifest left-right symmetry is approximately realized [Bab06, Bar02]. Similar to quark-mixing, the weak eigenstates of the $W_{L,R}$-bosons are given by a linear combination of the mass eigenstates $W_{1,2}$:

$$\begin{pmatrix} W_L \\ W_R \end{pmatrix} = \begin{pmatrix} \cos\zeta & -\sin\zeta \\ e^{i\phi}\sin\zeta & e^{i\phi}\cos\zeta \end{pmatrix} \begin{pmatrix} W_1 \\ W_2 \end{pmatrix}, \tag{2.23}$$

with mixing angle ζ and a CP violating[3] phase ϕ. (We will neglect ϕ in the following since it has no observable effect.) Further parameters of the manifest left-right symmetric theory are the ratios

$$\delta = \frac{m_1^2}{m_2^2} \qquad \text{and} \qquad \lambda' = \frac{g'_A}{g'_V}. \tag{2.24}$$

However, λ' may be different from the Standard Model value.

Until now, there is no experimental evidence for currents mediated by right-handed W_R-bosons. Therefore W_R (and W_2) have to be very heavy. One expects values in the order of $m_{W_R} \approx 10^4$ GeV [Nac86], what is also assumed to be the symmetry breaking scale. The Standard Model is restored from the theory when no mixing occurs ($\zeta = 0$) and the W_2 boson is infinitely heavy ($\delta = 0$).

Right-Handed Currents in Neutron Decay: We can deduce limits on the parameters λ', ζ, and δ from three independent experimental quantities, e.g. the correlation coefficients A, B, and the lifetime τ_n (cf. chapter 2.3). In 2004, when we started to work on this thesis, the status of right-handed currents in neutron decay was as shown in figure 2.4, which gives the 50 %, 90 %, and 95 % confidence levels for ζ and δ projected along the λ' axis. The input parameters are the mean values given by the Particle Data Group (PDG) [PDG04]. Obviously, data is fully consistent with the Standard Model.

However, if one halves the error on the neutrino asymmetry B, the quantity we have measured within this thesis, one obtains figure 2.5: The Standard Model in not included anymore in the 90 % confidence level, emphasizing the sensitivity of this parameter to right-handed currents and "physics beyond".

---

[3]It is interesting to note that in left-right symmetric models CP is violated even with only two generations, whereas the Standard Model needs three [Bab06].
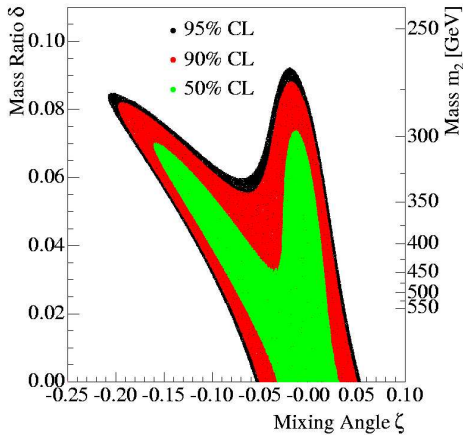
Figure 2.4: Exclusion plot for possible right-handed currents in neutron decay obatained with experimental values from 2004 [PDG04]. The Standard Model $\delta = \zeta = 0$ is consitent with the experimental situation.
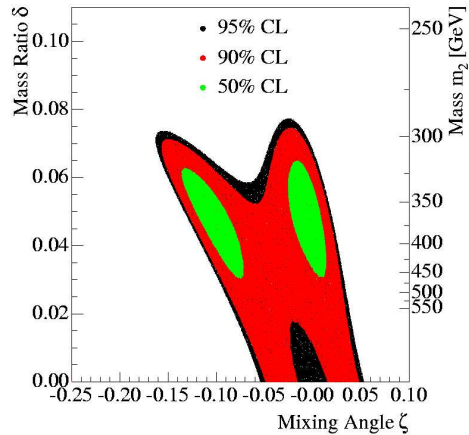
Figure 2.5: Exclusion plot with the values used in figure 2.4 but an halved error on the neutrino asymmetry B. This shows the sensitivity of this quantity on possible right-handed currents and the mass m_2 of the right-handed boson.

2.2.3 Measurements of Right-Handed Currents

Many experiments have been performed to get constraints on the mixing angle ζ and the mass m_2 of the right-handed boson W_R. In this section, we only give a brief overview following closely the Particle Data Group Summary [Bab06]: It suggests a limit of $m_2 > 715$ GeV obtained from a simultaneous fit to electroweak data, but does not give a value for ζ at all since the experimental situation is quite unclear.

Direct Search Limits: Direct search for the W_2-boson depends on the energy available to produce the particle and on the accessible decay channels. These are heavily model dependent and one has to make assumptions in order to get constraints: For example in the limit of small ζ and $m_{\nu_R} > m_2$, where the decay

$$W_2^+ \to \ell_R^+ + \nu_R \tag{2.25}$$

is forbidden by energy conservation, the DØ experiment at Tevatron excludes a mass range from 300 to 800 GeV [Aba04]. Other experiments, however, yield considerably lower values. If one assumes a light right-handed neutrino the decay (2.25) is possible, and the DØ limit reduces to $m_2 > 720$ GeV ($m_{\nu_R} \ll m_2$)) or $m_2 > 650$ GeV ($m_{\nu_R} = m_2/2$)) [Aba96]. Although all these limits already assume simple manifest left-right symmetry or pseudo-manifest left-right symmetry[4], they heavily depend on assumptions on particle masses etc.

Indirect Constraints: These are obtained from experiments that precisely measure electroweak quantities, since right-handed remnants would cause small deviations from the Standard Model values. Limits on the angle ζ can be derived from nonleptonic K-decays, from the transition $b \to s + \gamma$ in radiative B-meson decays, and from β-decays. However, they also

---

[4]In pseudo-manifest left-right symmetric models the quark mixing matrices V are related via $V_L = (V_R)^*$.

depend on assumptions on single parameters (ζ small, m_{ν_R} heavy, etc.) and published results differ partly by more than one order of magnitude.

If the mass of the right-handed neutrino is small enough to allow its emission in muon or β-decay, limits on m_2 can be derived. A polarized muon decay experiment [Bar97] yields the constraint $m_2 > 549$ GeV in the $\zeta = 0$ limit. Futher contraints come from astrophysics and cosmology, but again special assumptions have to be made: With a light ν_R, nucleosynthesis and supernova models give limits of several TeV, however, a heavy right-handed neutrino is required in the see-saw mechanism. Neutrinoless double beta decay experiments, assuming the neutrino to be a Majorana-particle, also give high limits $m_2 > 1.1$ TeV if there exists an heavy right-handed neutrino (see references in [Bab06]).

We conclude that every measurement providing limits without the need of a very specific set of parameters can give further insight into the question of left-right symmetry.

2.3   Neutron Decay

The neutron is the heavier of both nucleons ($m_n c^2 = 939.565$ MeV) and has the quark content udd. If not bound in a nucleus it decays into proton p, electron e^-, and anti-neutrino $\overline{\nu}_e$

$$n \rightarrow p + e^- + \overline{\nu}_e \tag{2.26}$$

with a lifetime $\tau = 885.7(8)$ s (all values taken from [PDG06]). The q-value of the process is given by the mass difference

$$q = (m_n - m_p - m_e - m_\nu)c^2 = 782.32 \text{ keV}. \tag{2.27}$$

If we consider proton recoil and a massless neutrino, this corresponds to an endpoint energy $E_0 = 781.57$ keV of the contiuous electron spectrum.

Low Energy Particle Physics: Compared to high energy physics with center of mass energies in the TeV-range, neutron decay with its tiny q-value is a perfect example of low energy particle physics. Needless to say, no new particles will be found at these energies, however, many insights into the structure of electroweak interactions (and also into QCD that enters via small corrections) can be obtained from very precise experiments. Therefore, low energy physics is an important subarea of particle physics. And if the next generation accelerators (LHC, ILC) will not find new particles, maybe the only way to discover new physics will be to study low energy processes[5] very carefully to find its remnants causing small deviations from well established parameters.

In principle, if a new physics process takes place at an energy scale $M^* \approx 10^{6\ldots19}$ GeV that is much too high to be directly accessible, it makes no difference if the experiments are carried out at energies $p = \mathcal{O}(1 \text{ neV})$ or $\mathcal{O}(1000 \text{ GeV})$; their influence on the propagator

$$\frac{1}{p^2 + M^{*2}} \rightarrow \frac{1}{M^{*2}} \tag{2.28}$$

is negligible in both cases [Dub07].

---

[5]In this sense, "low energy" spans a rather wide range from peV-neutrons trapped in the earth's gravitational potential to LEP energies.

The neutron delivers a perfect environment for precision measurements since it is available in large numbers at powerful sources, and all quarks and leptons of the first generation participate in its decay. Compared to studies of nuclear β-decay, where similar observables can be measured, it has the advantage that no corrections with large uncertainties due to nuclear structure arise.

Decay Probability: The neutron's decay probability ω can be calculated using Fermi's "Golden Rule"

$$d\omega(E) = \frac{2\pi}{\hbar} \; |T_{fi}|^2 \; \frac{d\phi(E)}{dE} \; dE, \tag{2.29}$$

where the number of possible final states is given by the phase space factor

$$d\phi(E) = \frac{1}{4\pi^4(\hbar c)^6} \; (E + m_e c^2) \; \sqrt{(E + m_e c^2)^2 - m_e^2 c^4} \; (E_0 - E)^2 \; dE = F'(E) \; dE. \tag{2.30}$$

Throughout this text, E denotes the kinetic energy of the electron, m_e its mass, and E_0 the endpoint energy of its spectrum. Additional small corrections have to be applied to the phase space factor $F'(E)$, plotted in figure 2.6, to account for Coulomb interaction between electron and proton, proton recoil, and radiative corrections (cf. chapter 4.5.1 for details).

From equation (2.14) we can calculate the transition matrix element T_{fi} in (2.29) and obtain the transition probability

$$d\omega \propto G_F^2 \; |V_{ud}|^2 \; F(E) \; (g_V^2 + 3g_A^2) \; dE \tag{2.31}$$

for unpolarized neutrons. $F(E)$ denotes the phase space factor with corrections.

Parity Violation in Neutron Decay: Within standard $V - A$ theory, there are two possible β-decay transitions: Fermi-transitions via vector currents conserve the orientation of the hadronic spin since the lepton spins are in a singlet state $S = 0$. As illustrated in figure 2.7, particle emission is isotropic here.

Axial-vector or Gamow-Teller transitions couple the lepton spins to the triplett state $S = 1$ and may flip the hadron spin. Parity violation becomes visible in this case since the spin orientation of the leptons is determined by angular momentum conservation, and the positive anti-neutrino helicity requests its momentum to be aligned in spin direction. Therefore emission of electrons and neutrinos is not isotropic; the same holds for protons since they are kinematically coupled to the two leptons.
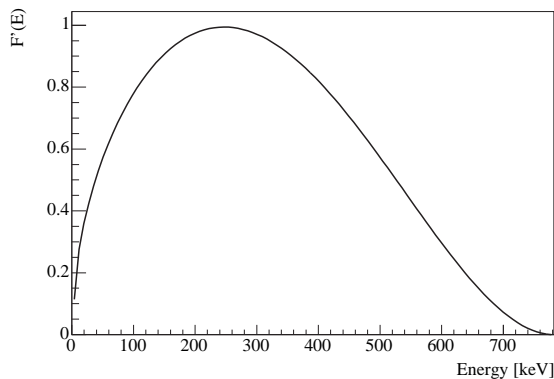

Figure 2.6: The "Fermi-function", the uncorrected phase space factor $F'(E)$ of the electron spectrum. Small corrections still have to be applied to account for Coulomb interaction between the charged decay products, proton recoil, and radiative corrections. The endpoint energy of the spectrum is at $E_0 = 781.57$ keV.

$$\text{F:}\quad \Uparrow \quad \longrightarrow \quad \Uparrow \qquad \left(\underset{e^-}{\Uparrow^{\downarrow}}\,\underset{\bar{\nu}_e}{\Downarrow^{\downarrow}} \;-\; \underset{e^-}{\Downarrow^{\uparrow}}\,\underset{\bar{\nu}_e}{\Uparrow^{\uparrow}} \right)$$
$$\underset{n}{} \qquad\qquad \underset{p}{}$$

$$\text{GT:}\quad \Uparrow \quad \longrightarrow \quad \Uparrow \qquad \left(\underset{e^-}{\Uparrow^{\downarrow}}\,\underset{\bar{\nu}_e}{\Downarrow^{\downarrow}} \;+\; \underset{e^-}{\Downarrow^{\uparrow}}\,\underset{\bar{\nu}_e}{\Uparrow^{\uparrow}} \right)$$
$$\underset{n}{} \qquad\qquad \underset{p}{}$$

$$\Uparrow \quad \longrightarrow \quad \Downarrow \quad \underset{e^-}{\Uparrow^{\downarrow}} \quad \underset{\bar{\nu}_e}{\Uparrow^{\uparrow}}$$
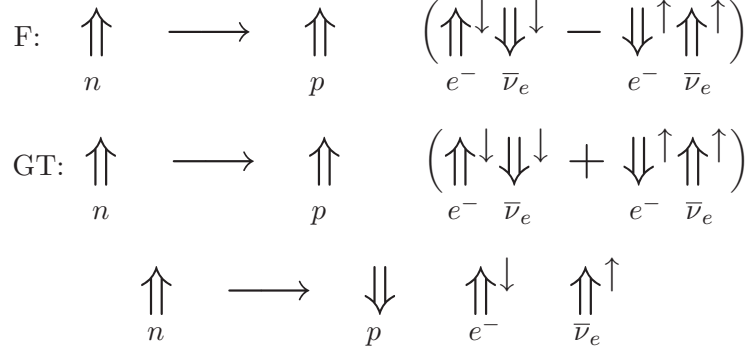$$\underset{n}{}$$

Figure 2.7: Fermi- (F) and Gamow-Teller transitions (GT): The double arrows represent the spin, the superscript arrow the momentum. The last GT-transition is the only one violating parity since the anti-neutrino is fully right-handed in $V - A$ theory, resulting in a non-isotropic emission of the decay products. (Figure based on [Rei99].)

2.3.1   Correlation Coefficients

As it is evident from figure 2.7, the neutron spin has to be aliged in a certain direction in order to detect the emission asymmetries of the decay products, i.e. the neutrons have to be polarized. In this case, the transition probability ω can be expressed in terms of measurable quantities, the so-called correlation coefficients [Jac57]:

$$
\begin{aligned}
\mathrm{d}\omega \quad \propto \quad & G_F^2\,|V_{ud}|^2\,F(E)\,(g_V^2 + 3g_A^2)\,\mathrm{d}E\,\mathrm{d}\Omega_e\,\mathrm{d}\Omega_\nu \\
& \times \left(1 + a\,\frac{\mathbf{p}_e \mathbf{p}_\nu}{E E_\nu} + b\,\frac{m_e}{E} + \langle \mathbf{s}_n \rangle \left[A\,\frac{\mathbf{p}_e}{E} + B\,\frac{\mathbf{p}_\nu}{E_\nu} + D\,\frac{\mathbf{p}_e \times \mathbf{p}_\nu}{E E_\nu} \right] \right),
\end{aligned}
\qquad (2.32)
$$

where $\mathbf{p}_e$, $\mathbf{p}_\nu$, E, E_ν are momentum and energy of electron and neutrino respectively. $\langle \mathbf{s}_n \rangle$ is the neutron spin direction, the Ω_i denote solid angles, and the parameters a, b, A, B, and D are the correlation coefficients, also referred to as "asymmetries": a is the correlation between the momenta of electron and neutrino. A non-vanishing Fierz interference term b would indicate the existence of scalar and tensor interactions, thus it is zero in the Standard Model. The parameters A and B are parity violating since they correlate the neutron spin with the momentum of electron and neutrino respectively. A non-vanishing triple-coefficient D would violate time reversal invariance.

In $V - A$ theory, all coefficients are functions of $\lambda = \frac{g_A}{g_V}$:

$$
a = \frac{1 - |\lambda|^2}{1 + 3|\lambda|^2}, \quad A = -2\,\frac{|\lambda|^2 + \mathrm{Re}(\lambda)}{1 + 3|\lambda|^2}, \quad B = 2\,\frac{|\lambda|^2 - \mathrm{Re}(\lambda)}{1 + 3|\lambda|^2}, \quad D = \frac{2\,\mathrm{Im}(\lambda)}{1 + 3|\lambda|^2}. \qquad (2.33)
$$

The proton does not occur in equation (2.32). However, since it is kinematically coupled to electron and neutrino energies and momenta, one can give a relation between the correlation coefficients A and B and the proton asymmetry C, and describe the latter in terms of λ [Glu95, Glu96]:

$$
C = x_C(A + B) \qquad \text{and} \qquad C = x_C\,\frac{4\,\mathrm{Re}(\lambda)}{1 + 3|\lambda|^2}, \qquad (2.34)
$$

Quantity		Value
Lifetime	τ_n	885.7(8) s
Coupling Ratio	λ	$-1.2695(29)$
Electron Asymmetry	A	$-0.1173(13)$
$e - \nu$ Correlation	a	$-0.103(4)$
Neutrino Asymmetry	B	$0.981(4)$
Proton Asymmetry	C	not listed
Triple Coefficient	D	$-4(6) \cdot 10^{-4}$

Figure 2.8: Average values of τ_n, λ, and the correlation coefficients in neutron decay as published by the Particle Data Group [PDG06].
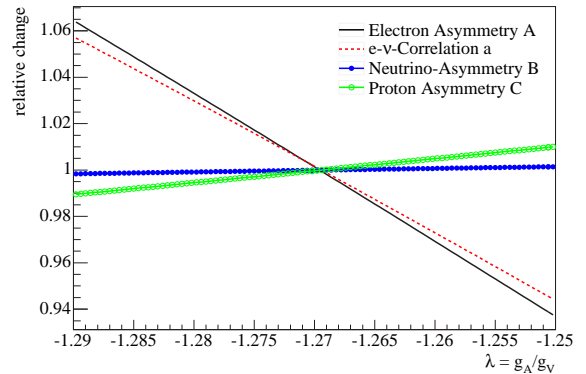
Figure 2.9: Sensitivity of the correlation coefficients a, A, B, and C on λ, the ratio of axial-vector to vector coupling constant.

where $x_C = 0.27484$ is a kinematical factor[6]. We present the 2006 average values of the various neutron decay coefficients in figure 2.8.

The precise knowledge of λ is important for calculations within the quark model and to compute neutrino cross sections. Moreover it is an essential ingredient in many astrophysical and cosmologial models describing the sun, supernovae, or nucleosynthesis after the big-bang. However, the sensitivity of the correlation coefficients to λ is quite diverse (cf. figure 2.9): The favoured observable to determine λ is the electron asymmetry A, and already many experiments have been performed on this topic [Abe02, Mun06]. Experiments to obtain λ via a are currently performed [Bae03] or developed [Wie05]. The sensitivity of the neutrino asymmetry B is rather poor; the proton asymmetry C looks somewhat better, up to now, however, it has never been tried to obtain λ in this way.

Within the framework of this thesis we measured both asymmetries, B and C, to search for physics beyond the Standard Model. In the following sections, we will discuss how these observables can be accessed experimentally.

2.3.2   Neutrino Asymmetry B

In polarized neutron decay, the neutron spin defines a plane that divides the full solid angle into two hemispheres: One in neutron spin direction and one against it. The basic quantities we measure in the experiment are the energy resolved electron spectra $N^\uparrow(E)$, $N^\downarrow(E)$. Therein the arrow denotes the emission direction with respect to the neutron spin ($\uparrow$: parallel, $\downarrow$: anti-parallel), corresponding to the hemisphere in which the electron was detected. For the measurements presented here, a coincident detection of the proton hemisphere is additionally required, and a second arrow is introduced in the notation to represent this: $N^{\uparrow\uparrow}(E)$, $N^{\downarrow\downarrow}(E)$, $N^{\uparrow\downarrow}(E)$, and $N^{\downarrow\uparrow}(E)$. The proton energy is not measured.

---

[6]Please note that we define the proton asymmetry C with opposite sign compared to [Glu95]. This retains the convention that a positive asymmetry indicates more particles to be emitted in spin direction.

Electron Spectra without Proton Information: We will just briefly mention the case where the proton is not detected. The sum S of the two electron spectra

$$S(E) = N^\uparrow(E) + N^\downarrow(E) \propto F(E) \tag{2.35}$$

is then given by the corrected Fermi-function defined in (2.30). The difference D scales with the electron velocity v:

$$D(E) = N^\downarrow(E) - N^\uparrow(E) \propto \frac{v}{c} F(E). \tag{2.36}$$

The experimental electron asymmetry $A_{\exp}(E)$ a function of energy E and is related to the scalar correlation coefficient A from equation (2.32) via

$$A_{\exp}(E) = \frac{N^\downarrow(E) - N^\uparrow(E)}{N^\downarrow(E) + N^\uparrow(E)} = \frac{1}{2}\frac{v}{c} A F(E), \tag{2.37}$$

where the factor $\frac{1}{2}$ stems from integration over the solid angle of one hemisphere. One can see nicely here, how the energy dependent experimental asymmetry $A_{\exp}(E)$ is related to the scalar (integal) asymmetry or correlation coefficient A. The relations for the neutrino asymmetry are not that simple.

Coincident Spectra in the Same Hemisphere: One aim of this thesis was the measurement of the neutrino asymmetry B. As the neutrino cannot be detected easily, we have to deduce its emission direction from a coincident measurement of electron and proton emitted into the two hemispheres defined by the neutron spin.

The first - statistically as well as systematically favoured - case comprises events where electron and proton are emitted into the same hemisphere as illustrated in figure 2.10. The corresponding electron spectra $N^{\uparrow\uparrow}(E)$, $N^{\downarrow\downarrow}(E)$ can be written as follows:

$$N^{\uparrow\uparrow}(E) = Q^{++}(E) F(E) \tag{2.38}$$
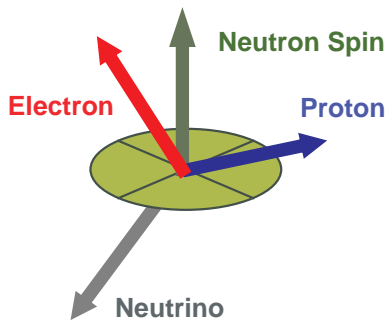$$N^{\downarrow\downarrow}(E) = Q^{--}(E) F(E). \tag{2.39}$$

Figure 2.10: Illustration of a same-hemisphere-event: The neutron spin divides space into two hemispheres, electron and proton are emitted into the same hemisphere. The neutrino is restricted to the opposite hemisphere due to momentum conservation.
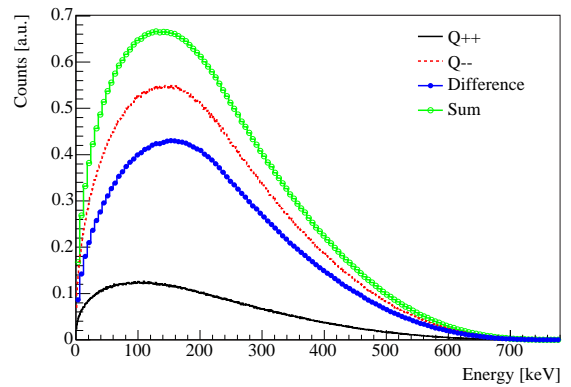
Figure 2.11: Simulation of the functions Q^{++} and Q^{--} (multiplied with the Fermi-function $F(E)$), where electron and proton are measured in coincidence in the same hemisphere. A + indicates emission in neutron spin direction. Sum S and difference D of the spectra are also shown.

Glück et al. [Glu95] calculated the Q-functions by integrating the transition probability (2.32) with respect to the observed particles:

$$Q^{++}(E) = \begin{cases} 1 - \frac{r}{2} + \frac{a\beta}{4}\left(\frac{r^2}{2} - 1\right) + PA\beta\left(\frac{1}{2} - \frac{r}{3}\right) + P\frac{B}{2}\left(\frac{r^2}{3} - 1\right) & \text{for } r < 1 \\ \frac{1}{2r}\left(1 - \frac{a\beta}{4r} + \frac{PA\beta}{3r} - \frac{2PB}{3}\right) & \text{for } r \geq 1 \end{cases} \tag{2.40}$$

$$Q^{--}(E) = Q^{++}(E)[P \rightarrow -P]. \tag{2.41}$$

The definition is separated into two regions by the energy dependent parameter

$$r = \beta\frac{E + m_e}{E_0 - (E + m_e)} \tag{2.42}$$

which is unity at $E = 236$ keV. a, A, and B are the correlation coefficients, $\beta = \frac{v}{c}$, and P is the neutron spin polarization that has to be changed to $-P$ to describe the Q^{--} spectrum. Both functions are shown in figure 2.11.

Sum $S_{\text{same}}(E)$, difference $D_{\text{same}}(E)$, and asymmetry $B_{\text{same}}(E)$ built out of spectra satisfying the "same hemisphere" condition can be easily described using the Q-functions defined above:

$$D_{\text{same}}(E) = N^{\downarrow\downarrow}(E) - N^{\uparrow\uparrow}(E) = (Q^{--}(E) - Q^{++}(E))\, F(E) \tag{2.43}$$

$$S_{\text{same}}(E) = N^{\downarrow\downarrow}(E) + N^{\uparrow\uparrow}(E) = (Q^{--}(E) + Q^{++}(E))\, F(E) \tag{2.44}$$

$$B_{\text{same}}(E) = \frac{N^{\downarrow\downarrow}(E) - N^{\uparrow\uparrow}(E)}{N^{\downarrow\downarrow}(E) + N^{\uparrow\uparrow}(E)} = \frac{Q^{--}(E) - Q^{++}(E)}{Q^{--}(E) + Q^{++}(E)}. \tag{2.45}$$

From a fit of expression (2.45) to the measured asymmetry spectrum $B_{\text{exp}}(E)$ we obtain the value of the neutrino asymmetry B. Figure 2.12 shows the energy dependence of $B_{\text{same}}(E)$: At energies greater than 200 keV it is almost flat, a very appealing feature since energy calibration of the detectors is less important in this case. Futhermore the curve is located at relatively large values (≈ 0.65) leading to a high statistical significance. The determination of B from electrons and protons emitted in the same hemisphere is statistically and systematically favoured.

Opposite Hemispheres: The second possibility to determine the neutrino asymmetry B is to analyze the spectra $N^{\uparrow\downarrow}(E)$ and $N^{\downarrow\uparrow}(E)$. These contain events measured under the condition that electron and proton have been emitted into opposite hemispheres, a situation
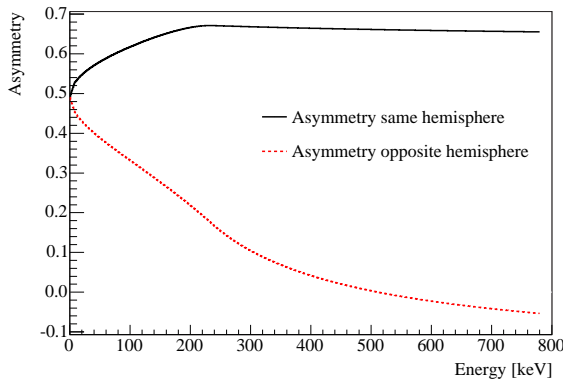

Figure 2.12: Energy dependence of the experimental asymmetries measured in the same hemisphere $B_{\text{same}}(E)$ and in opposite hemispheres $B_{\text{opp}}(E)$ (lower curve). The first is systematically favoured since its characteristics is flat above 200 keV which leads to almost no dependence on the detector calibration uncertainty. Unfortunately, this is not the case for the rather steep $B_{\text{opp}}(E)$ where detector calibration plays a crucial role.
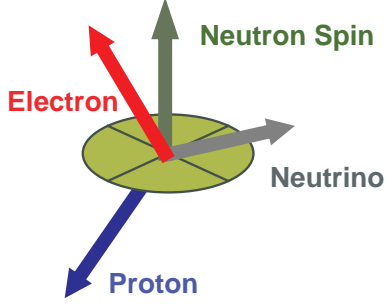
Figure 2.13: Illustration of an event with elec-
tron and proton in opposite hemispheres. This
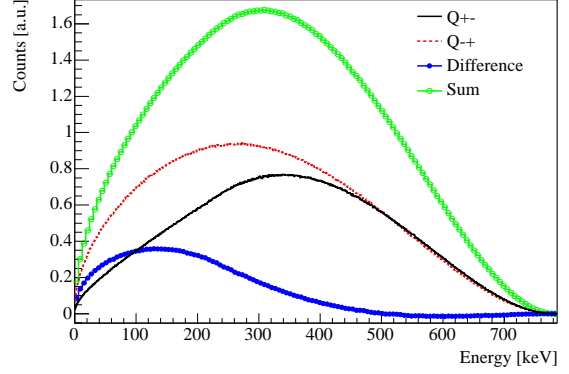provides more possibilities for the $\bar{\nu}_e$-direction.

Figure 2.14: Simulation of the theoretical func-
tions Q^{+-}, Q^{-+}, D_{opp}, and S_{opp} where electron
and proton are detected in opposite hemispheres.

depicted in figure 2.13. The analytical expressions make use of the functions Q^{+-} and Q^{-+}
[Glu95]

$$Q^{+-}(E) \;=\; 2 + PA\beta - Q^{++}(E) \tag{2.46}$$
$$Q^{-+}(E) \;=\; 2 - PA\beta - Q^{--}(E) \tag{2.47}$$

(cf. figure 2.14) and read

$$N^{\uparrow\downarrow}(E) \;=\; Q^{+-}(E)\, F(E) \tag{2.48}$$
$$N^{\downarrow\uparrow}(E) \;=\; Q^{-+}(E)\, F(E). \tag{2.49}$$

From equations (2.46) and (2.47) we can again get expressions for difference $D_{\mathrm{opp}}(E)$, sum
$S_{\mathrm{opp}}(E)$, and asymmetry spectrum $B_{\mathrm{opp}}(E)$. The resulting equations are lengthy and show
nothing new, therefore we do not write them down here.

The energy dependence of the experimental asymmetry $B_{\mathrm{opp}}(E)$ is also shown in figure 2.12.
Although it is the kinematically favoured type of event - approximately 78 % of all decays
have electron and proton emitted in opposite hemispheres - its statistical significance is rather
low: It reaches the highest sensitivity on B at very low energies where electron spectroscopy
is very difficult and suffers from threshold and backscattering effects. Additionally, $B_{\mathrm{opp}}(E)$
strongly depends on the electron energy E requiring a very well known detector calibration.

2.3.3 Proton Asymmetry C

Having determined the experimental spectra $N^{\uparrow\uparrow}$, $N^{\downarrow\downarrow}$, $N^{\uparrow\downarrow}$, and $N^{\downarrow\uparrow}$ corresponding to the
various Q-functions (multiplied with the Fermi-function F), we can use them to obtain the
proton asymmetry C. Figure 2.15 shows the spectra

$$\rho^{\uparrow}(E) \;=\; Q^{++}(E) + Q^{-+}(E) \tag{2.50}$$
$$\rho^{\downarrow}(E) \;=\; Q^{--}(E) + Q^{+-}(E) \tag{2.51}$$

including only events where the proton is emitted into a particular hemisphere, the electron
direction is not considered. The arrow refers to the proton momentum. From these, the
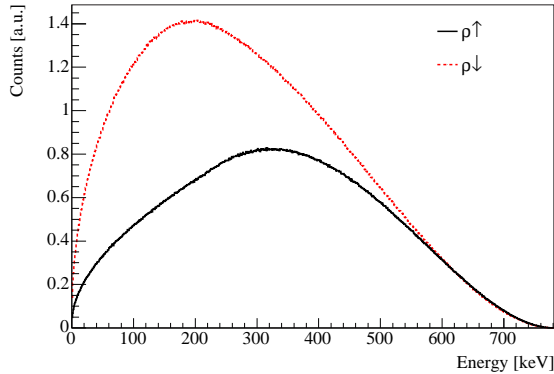
Figure 2.15: The functions $\rho^\uparrow = Q^{++} + Q^{-+}$ and $\rho^\downarrow = Q^{--} + Q^{+-}$ that include all events with a proton emitted into a particular hemisphere. The asymmetry built from their integrals is called the proton asymmetry C.
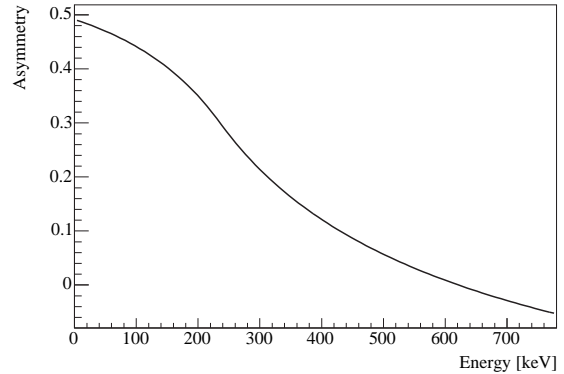
Figure 2.16: Graph of the experimental proton asymmetry C_{exp}. However, since there is no analytical description for this function based on C, the integral proton asymmetry, we can only obtain the neutrino asymmetry B from a fit.

electron energy dependent experimental proton asymmetry

$$C_{\mathrm{exp}}(E) = \frac{\rho^\uparrow(E) - \rho^\downarrow(E)}{\rho^\uparrow(E) + \rho^\downarrow(E)} \tag{2.52}$$

can be constructed (cf. figure 2.16). However, since the decay probability ω, equation (2.32), is expressed in terms of electron and neutrino parameters, there is no analytical expression based on the scalar proton asymmetry C to describe C_{exp}. Thus we cannot obtain C from a fit to this data, however, it can be used as a third method to determine the neutrino asymmetry B, since C_{exp} can be described using a combination of all four Q-spectra. Please note that the result from this approach is not independent of the B-values obtained in measurements of B_{same} and B_{opp} since it uses the same data.

The only way to determine the proton asymmetry C itself from the measured spectra N^{ij} is an integral method: C defines the asymmetry in proton emission with respect to the neutron spin. Mathematically this reads

$$C = \frac{\int \rho^\uparrow(E)\mathrm{d}E - \int \rho^\downarrow(E)\mathrm{d}E}{\int \rho^\uparrow(E)\mathrm{d}E + \int \rho^\downarrow(E)\mathrm{d}E}, \tag{2.53}$$

where the integration is performed over all electron energies. In other words, C can be obtained by calculating the asymmetry in the area below the functions $\rho^\uparrow(E)$ and $\rho^\downarrow(E)$ in figure 2.15. Due to linearity of integration we can also integrate the four Q-functions themselves and get the same result. This approach will be persued in the final analysis, however, we will have to extrapolate from an integration interval at medium energies to lower values, since a precise measurement of Q^{ij} is impossible at low energies due to the finite detector threshold.

2.3.4 Previous Measurements of Correlation Coefficients B and C

Up to now, five measurements of the neutrino asymmetry B in neutron decay have been performed. Their results are shown in the table:

$B =$	Year	Authors
0.995(34)	1970	Erozolimsky et al. [Ero70]
1.00(5)	1970	Christensen et al. [Chr70]
0.9894(83)	1995	Kuznetsov et al. [Kuz95]
0.9801(46)	1998	Serebrov et al. [Ser98]
0.967(6)	2005	Kreuz et al. [Kre05b]

The experiments of the 70s are not competitive anymore as they suffered from large uncertainties and corrections. The measurements in the 90s, dominating the current world average, were done by one Russian collaboration using the same instrument (cf. figure 2.17): It only allowed a detection of electron and proton in opposite hemispheres, however, the statistical sensitivity was improved by an additional determination of the proton's momentum projection onto the axis defined by the neutron spin. This was achieved using a time-of-flight method. The corrections Δ that had to be applied to obtain the final value were significantly larger than the errors: $\Delta \approx 33$ % in [Kuz95] and $\Delta \approx 5$ % in [Ser98].

All experiments mentioned so far were only able to measure in opposite hemispheres, but could be analyzed differently since no integration over hemispheres was performed. However, this gives rise to uncertainties due to solid angle corrections. The first experiment allowing an analyis of B_{same} was the latest B-measurement published by the PERKEO collaboration (Kreuz et al. [Kre05b]), using the same spectrometer PERKEO II that we have used in the experiment described in this text. The uncertainty is quite large due to severe statistical problems, however, it was shown for the first time that a determination of B_{same} is feasible.

Since all four spectra N^{ij} are needed to get the proton asymmetry, only the last measurement could be analyzed in this way. A value for C was obtained with a rather large uncertainty of 5 % [Kre04b, Abe05].
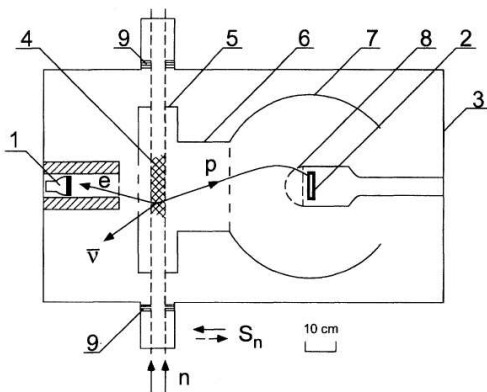

Figure 2.17: Sketch of the Gatchina instrument to measure the neutrino asymmetry B using opposite hemispheres. However, a analysis method different to PERKEO II could be used since the proton momentum was additionally measured using a time-of-flight technique. The polarized neutrons enter the vacuum chamber (3) from the bottom. Shown are (1) electron detector, (2) proton detector, (4) decay region, (5,7) electrodes, (6) TOF electrode, (8) spherical grid, (9) LiF diaphragm. Figure from [Kuz95].

2.3.5   Right-Handed Currents in Neutron Decay

We close the introductory part of this thesis with the discussion how possible right-handed contributions can be derived from neutron decay data: Admixtures of right-handed currents will change the Standard Model relations (2.33) between the correlation coefficients and $\lambda = \frac{g_a}{g_V}$, and two more parameters, the mixing angle ζ and the mass ratio δ introduced in section 2.2.2, have to be considered. Therefore, we need three experimental input values, e.g. A, B, and the lifetime τ_n, in order to obtain these three parameters:

$$(A, B, \tau_n) \rightarrow (\lambda', \zeta, \delta = \frac{m_1^2}{m_2^2}). \tag{2.54}$$

The Left-Right-Symmetric Lagrangian: To calculate the dependence of the correlation coefficients on the left-right-symmetric (LR) parameters, we need to know the LR-symmetric Lagrangian. Here, we will only sketch the important steps of the derivation, which is presented in detail in [Beg77, Hol77, Doe90].

Starting point is the usual four-fermion $V - A$ current-current interaction, equation (2.14):

$$\mathcal{L}_{V-A} = -\frac{G_F}{\sqrt{2}} \, \overline{p}\gamma^\mu(1 - \lambda\gamma^5)n \, \overline{e}\gamma_\mu(1 - \gamma^5)\nu_e. \tag{2.55}$$

When we use equation (2.11), and introduce a shortened notation for the hadronic and leptonic vector and axial-vector currents, $V_h = \overline{p}\gamma^\mu n$, $A_h = \overline{p}\gamma^\mu\gamma^5 n$, $V_\ell = \overline{e}\gamma_\mu\nu_e$, $A_\ell = \overline{e}\gamma_\mu\gamma^5\nu_e$ omitting the Lorentz indices, the equation can be rewritten:

$$\mathcal{L}_{V-A} = -\frac{g^2}{8m_W^2} \, (V_h - \lambda A_h) \, (V_\ell - A_\ell) = -\frac{g^2}{8m_W^2} \, (J_h \, J_\ell). \tag{2.56}$$

This expression is still pure $V - A$ theory, where the interaction is mediated by a left-handed W_L-boson. If we now introduce LR-symmetry and an additional right-handed boson W_R, mixing occurs according to equation (2.23) with the mass eigenstates W_1 and W_2, given by

$$W_1 = W_L \cos\zeta - W_R \sin\zeta, \qquad W_2 = W_L \sin\zeta + W_R \cos\zeta, \tag{2.57}$$

and we can write down the Lagragian of the LR-symmetric model

$$\mathcal{L}_{LR} = -\frac{g^2}{8m_1^2} \, (J_{h_1} \, J_{\ell_1}) - \frac{g^2}{8m_2^2} \, (J_{h_2} \, J_{\ell_2}). \tag{2.58}$$

The currents J_{h_1} etc. are compositions of left- and right-handed currents, e.g.

$$J_{h_1} = J_h^L \, \cos\zeta - J_h^R \, \sin\zeta = (V_h - \lambda A_h) \, \cos\zeta - (V_h + \lambda A_h) \, \sin\zeta \tag{2.59}$$

$$J_{\ell_1} = J_\ell^L \, \cos\zeta - J_\ell^R \, \sin\zeta = (V_\ell - A_\ell) \, \cos\zeta - (V_\ell + \lambda A_\ell) \, \sin\zeta, \text{ etc.} \tag{2.60}$$

The operator $(1+\gamma^5)$ gives the right-handed part (RH) of a spinor, thus there is only a simple sign change in the currents J^R to account for the right-handed contributions.

Using relations (2.59), (2.60), and the corresponding expressions for J_{h_2} and J_{ℓ_2}, equation (2.58) can be transformed into

$$\mathcal{L}_{LR} = -\frac{G'}{\sqrt{2}} \, (V_h V_\ell + \eta_{AA} \, \lambda A_h A_\ell + \eta_{VA} \, (V_h A_\ell + \lambda A_h V_\ell)), \tag{2.61}$$

an expression first given in [Beg77], with the definitions

$$
\eta_{AA} = \frac{\epsilon^2 m_2^2 + m_1^2}{\epsilon^2 m_1^2 + m_2^2} = \frac{\epsilon^2 + \delta}{\epsilon^2 \delta + 1}, \tag{2.62}
$$

$$
\eta_{VA} = \frac{-\epsilon(m_2^2 - m_1^2)}{\epsilon^2 m_1^2 + m_2^2} = \frac{-\epsilon(1 - \delta)}{\epsilon^2 \delta + 1}, \tag{2.63}
$$

$$
\epsilon = \frac{1 + \tan\zeta}{1 - \tan\zeta}, \qquad \text{and} \tag{2.64}
$$

$$
\frac{G'}{\sqrt{2}} = \frac{g^2}{8 m_1^2} \left(\cos\zeta - \sin\zeta\right)^2 + \frac{g^2}{8 m_2^2} \left(\cos\zeta + \sin\zeta\right)^2. \tag{2.65}
$$

Reorganization in terms of the hadronic vector V_h and axial-vector A_h currents yields

$$
\begin{aligned}
\mathcal{L}_{\mathrm{LR}} = & -\frac{G'}{\sqrt{2}} \left[V_h \left(V_\ell + \eta_{VA} A_\ell\right) + \lambda A_h \left(\eta_{AA} A_\ell + \eta_{VA} V_\ell\right)\right] \\
= & -\frac{G'}{\sqrt{2}} \left[V_h \left(\frac{1 - \eta_{VA}}{2}(V_\ell - A_\ell) + \frac{1 + \eta_{VA}}{2}(V_\ell + A_\ell)\right) \right. \\
& \left. + \lambda A_h \left(\frac{\eta_{AA} - \eta_{VA}}{2}(V_\ell - A_\ell) + \frac{\eta_{AA} + \eta_{VA}}{2}(V_\ell + A_\ell)\right)\right],
\end{aligned} \tag{2.66}
$$

therefore the admixture of right-handed relative to the much larger left-handed currents is given by

$$
r_V = \frac{1 + \eta_{VA}}{1 - \eta_{VA}} \qquad \text{and} \qquad r_A = \frac{\eta_{AA} + \eta_{VA}}{\eta_{AA} - \eta_{VA}} \tag{2.67}
$$

for the vector and the axial-vector parts respectively.

Effects of Right-Handed Currents on Observables: We can use these results to calculate wave functions of final states in neutron decay. For this purpose, we assume the leptons to be massless, thus in helicity eigenstates, however, the results agree with the exact solutions [Beg77, Hol77]. Within $V - A$ theory, the wave function of the neutron final state of a Gamow-Teller transition, for example, would be

$$
|\psi_{\mathrm{V-A}}\rangle = g_A\, M_{\mathrm{GT}}\, \sqrt{\frac{2}{3}}\, |\Uparrow^\downarrow \Uparrow^\uparrow\rangle, \tag{2.68}
$$

where g_A is the coupling constant, $M_{\mathrm{GT}} = \sqrt{3}$ the matrix element, and $\sqrt{\frac{2}{3}}$ the Clebsch-Gordan coefficient from angular momentum coupling. This state corresponds to the last row of figure 2.7 on page 18, the arrows indicate spin ($\Uparrow$) and momentum ($\uparrow$) of electron and neutrino respectively. The states are orthogonal, i.e. $\langle \Uparrow^\uparrow \Uparrow^\downarrow\, |\, \Uparrow^\downarrow \Uparrow^\uparrow \rangle = 0$. Further details can be found in [Doe90].

Let us now account for right-handed currents added with the relative admixture r_A: They turn the lepton's momenta since the spin directions are fixed by angular momentum conservation, thus we get for the example above

$$
|\psi_{\mathrm{LR}}\rangle = g_A'\, M_{\mathrm{GT}}\, \sqrt{\frac{2}{3}}\, \left(|\, \Uparrow^\downarrow \Uparrow^\uparrow\rangle + r_A |\, \Uparrow^\uparrow \Uparrow^\downarrow\rangle\right). \tag{2.69}
$$

In this way, we obtain wave functions of all states we are interested in, e.g. $|\nu^\uparrow\rangle$ and $|\nu^\downarrow\rangle$, where the neutrino is emitted in or against neutron spin direction respectively, in order to calculate the expression for the neutrino asymmetry B. Using the probabilities

$$P_{\nu\uparrow} = \langle\nu^\uparrow|\nu^\uparrow\rangle \qquad \text{and} \qquad P_{\nu\downarrow} = \langle\nu^\downarrow|\nu^\downarrow\rangle \tag{2.70}$$

the asymmetry can be defined and evaluated:

$$B = \frac{P_{\nu\uparrow} - P_{\nu\downarrow}}{P_{\nu\uparrow} + P_{\nu\downarrow}} = \frac{2g'_A(g'_A(1-r_A^2) + g'_V(r_V r_A - 1))}{g'^2_V(1+r_V^2) + 3g'_A(1+r_A^2)}. \tag{2.71}$$

The primed coupling constants g'_A, g'_V do not necessarily correspond to the $V-A$ constants g_A, g_V, however, since the conserved vector current hypothesis (CVC) is also valid here we can still set $g'_V = g_V = 1$ [Hol77] and $\lambda' = \frac{g'_A}{g'_V} = g'_A$. In general, we are interested in ζ and δ and look for limits on these values for arbitrary λ'.

When we apply this notation to (2.71), and furthermore calculate the corresponding expressions for the electron-asymmetry A, the $e\nu$-correlation a, and the rate function

$$R_{ft} = \frac{f^R \tau_n \ln(2)}{ft_{0^+ \to 0^+}}, \tag{2.72}$$

which is the ratio of the neutron's ft-value[7] and the same expression for superallowed nuclear decays[8], we get the following terms[9]:

$$A = 2\frac{\lambda'(r_V r_A - 1) + \lambda'^2(r_A^2 - 1)}{(1 + r_V^2) + 3\lambda'^2(1 + r_A^2)} \tag{2.73}$$

$$B = 2\frac{\lambda'^2(1 - r_A^2) + \lambda'(r_V r_A - 1)}{(1 + r_V^2) + 3\lambda'^2(1 + r_A^2)} \tag{2.74}$$

$$a = \frac{(1 + r_V^2) - \lambda'^2(1 + r_A^2)}{(1 + r_V^2) + 3\lambda'^2(1 + r_A^2)} \tag{2.75}$$

$$R_{ft} = \frac{2(1 + r_V^2)}{(1 + r_V^2) + 3\lambda'^2(1 + r_A^2)}. \tag{2.76}$$

Now, we can relate measured correlation coefficients to limits on right-handed contributions to the weak interaction by using these equations. In the Standard Model case, $r_V = r_A = 0$ and $\lambda' = \lambda$, and equations (2.73)−(2.76) are equivalent to (2.33).

---

[7]The ft-value

$$ft = \text{const.} \frac{\ln 2}{g_V^2 M_{\mathrm{F}}^2 + g_A^2 M_{GT}^2}$$

is a measure for nuclear matrix elements and coupling constants. It can be determined by measuring life-time τ and q-value of a β-decay. [May94]

[8]Superallowed nuclear $0^+ \to 0^+$ decays, making pure Fermi-transitions with matrix element $M_F = \sqrt{2}$, are used to normalize the neutron's $f^R t$ value to get rid of proportionality constants. $f^R = 1.71335(15)$ already includes radiative corrections [Wil82]; a sign error is mentioned in [Abe04].

[9]The expressions for A and R_{ft} can also be found in [Hol77]. [Doe90] and [Abe98] present all four equations but include some misprints.

Chapter 3

Measurement of Correlation Coefficients B and C

The experiment to determine the correlation coefficients B and C in the decay of polarized neutrons – called PERKEO IIB – was done in summer 2004. We decided to tackle this measurement and applied for beamtime in spring 2004, hence there was only little time for preparations. But since a determination of the electron asymmetry A was performed by our group from winter 2003 to summer 2004 [Mun06], we were able to reuse large parts of the already existing installations. Nevertheless many important parts – detection system, data acquisition, beam collimation, etc. – had to be prepared for the B and C measurement.

This chapter presents the details of the measurement, introduces the electron spectrometer PERKEO II and the experimental setup. In section 3.4, we describe the detection system in-depth and give some comments on background and shielding in section 3.5.

3.1 The Spectrometer PERKEO II

The central part of the electron spectrometer PERKEO II (cf. figure 3.1) consists of two superconducting coils with an inner diameter of 890 mm. They are arranged in a near-Helmholtz configuration which produces a magnetic field with a slight gradient on the central axis. We us a maximum field strength of $B = 1.03$ T between the coils. The neutron beam passes the center of the spectrometer perpendicular to the field lines, and charged particles that are created in neutron decays in the decay volume between the coils are guided onto the two detectors by the magnetic field. The uncharged neutrons are not affected by the field; Stern-Gerlach-effects occuring in an inhomogenious magnetic field are tiny and can be neglected for the asymmetry measurement [Kre04b].

Baffles are used to define the length of the decay volume: Only particles from decays in this region can be seen by the detectors, but for these we have a full $2 \times 2\pi$ solid angle detection since all charged particles are guided onto one of the two detectors by the magnetic field, independently of their initial emission direction. The particular detector is determined by the particle's momentum component $p_\parallel$ parallel to the field lines[1]: The decay volume is separated in two hemispheres.

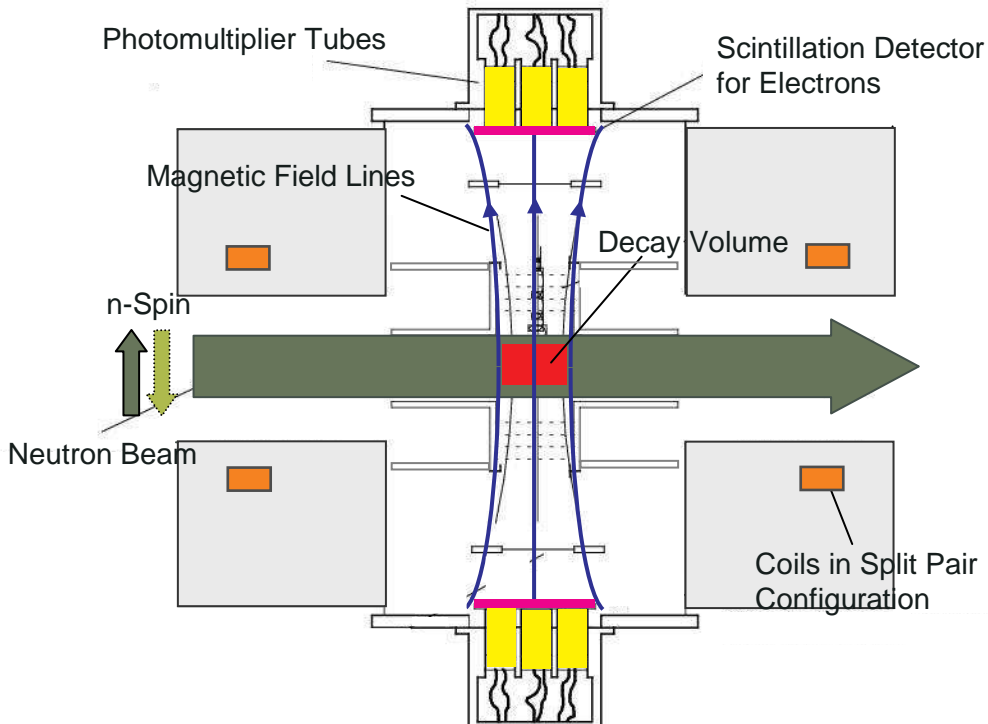[1]The magnetic mirror effect (cf. sections 3.3.3 and 4.5.2) is neglected here.

Figure 3.1: A schematic drawing of the electron spectrometer PERKEO II: The neutron beam enters the spectrometer from the left with the spin polarized parallel to the magnetic field which is created by two superconducting coils (diameter: 890 mm). The field guides the charged particles out of the decay volume, and separates the full solid angle into two hemispheres each covered by a detector.

Measuring Principle: In order to obtain the neutrino asymmetry B and the proton asymmetry C, we have to generate the spectra Q^{ij} by measuring the number of particles emitted in and against spin direction. Hence we use the magnetic separation in hemispheres by aligning the spin of the polarized neutrons (cf. section 3.3.2) with the field lines in the decay volume. Now the full solid angle is divided into hemisphere in spin direction and hemisphere opposite to the spin direction.

One big advantage of PERKEO II is its possibility to measure the electron's energy spectrum. Compared to an integral measurement of the asymmetries, this allows many additional systematic checks and limits the uncertainties due to detector effects.

3.2 The Beam Position PF1B at ILL

We performed the experiment at the cold neutron beam position PF1b of the High Flux Neutron Source operated by the Institut Laue-Langvin (ILL) from June to August 2004. The ILL is located in Grenoble (France) and houses one of the strongest neutron sources for scientific use in the world (flux $\phi = 1.5 \cdot 10^{15}$ cm^{-2} s^{-1}). Scientific interest of ILL users is usually located in the area of solid state physics, soft matter physics, chemistry, and bio sciences where the neutron is used as a "tool" to examine matter. Only a small group of

scientists studies the neutron as a physical "object" – this work is an example for these activities.

ILL-Reactor: In principle, the reactor has a thermal power of 58.3 MW and consumes about 1 kg of ^{235}U-fuel during a continuous reactor cycle of 50 days. Due to modifications of beam tubes the reactivity has decreased and reactor power is reduced to 54 MW for 50 days operation. This was also the situation when our experiment was done. Initially, the fission neutrons have high energies (several MeV, "fast neutrons") but are quickly thermalized by interacting with the cooling water surrounding the fuel element. These thermal neutrons with energies of $E \approx \frac{1}{40}$ eV still have velocities $v \approx 2200$ m s^{-1} what is much too fast for particle physics experiments, where the number of neutrons decaying within the apparatus is inversely proportional to their velocity. Therefore some of the neutrons are moderated in a vessel filled with liquid deuterium at 25 K, the so-called "cold source". These cold neutrons[2] have velocities of about 1000 m s^{-1} corresponding to a wavelength of $\lambda \approx 4$ Å, since the velocity v is related to the wavelength via

$$\lambda = \frac{3956}{v} \text{ m s}^{-1} \text{ Å}. \tag{3.1}$$

Beam Position PF1b: We find an excellent environment for our experiments with PERKEO at the fundamental physics beam position PF1b. It consists merely of free experimental space (10×3 m^2) with infrastructure (electricity, water, air, etc.) where the user can build up his own experimental setup. The supermirror neutron guide H113 with a cross section of 60×200 mm^2 ends right in front of the beam position and delivers the virtually most intense beam of cold neutrons in the world. Its capture flux ϕ_c at the entrance is $\phi_c = 1.4 \cdot 10^{10}$ cm^{-2} s^{-1} [Sch04, Abe06]. This is the particle flux

$$\phi = \int_v \phi(v) \, \mathrm{d}v \tag{3.2}$$

weighted with the velocity v, thus

$$\phi_c = \int_v \phi(v) \, \frac{v_0}{v} \, \mathrm{d}v, \tag{3.3}$$

with the thermal velocity $v_0 = 2200$ m s^{-1}. In the type of experiments described here, the capture flux is more interesting than the normal flux since neutron detectors often have a $\frac{1}{v}$-detection efficiency and the neutron decay rate at a given location is also inversely proportional to the velocity. For cold neutrons, the absolute flux is lower than the capture flux since $v < v_0$.

The beam position is located at about 80 m from the reactor core. Nevertheless, a very high flux is delivered since neutrons can be efficiently transported through supermirror neutron guides by reflection. Supermirrors consist of typically 100 double layers of nickel and titanium to increase the critical angle of reflection by a factor of two compared to the standard guides. Details on the properties of the ballistic supermirror guide H113 can be found in [Hae02] and [Abe06].

---

[2]Besides their advantages in particle physics experiments, cold neutrons are also easier to transport in neutron guides, polarization is facilitated, and they are better suited for some scattering experiments.
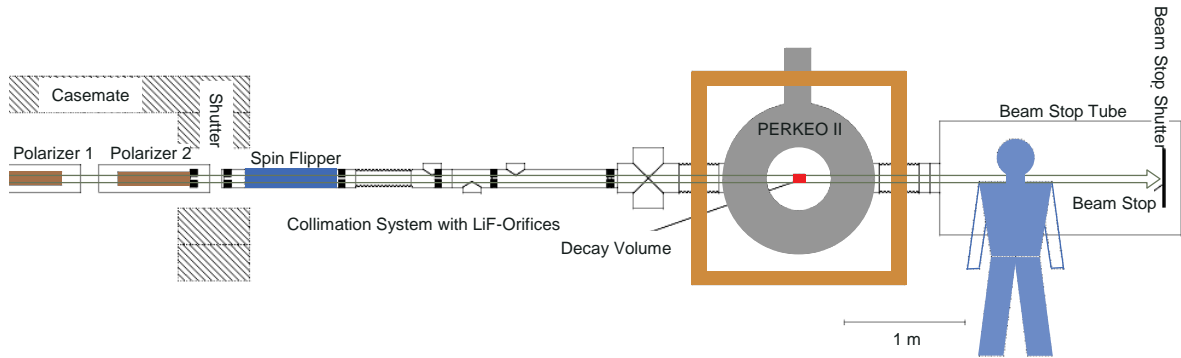
Figure 3.2: The experimental setup of PERKEO IIB: Neutrons enter from the left, are polarized and collimated and transit the spectrometer. The beam is disposed in a beam stop made out of ^{6}LiF-tiles.

3.3 Experimental Setup

In this section, we describe the installations that was built up at the beam position PF1b in order to perform the asymmetry measurement. Figure 3.2 shows the whole experimental setup drawn to scale. For clarity, the lead, boron, and polyethylene shieldings protecting from γ-radiaton and neutrons are not displayed.

3.3.1 Beamline

When the neutrons have left the supermirror neutron guide, they entered the PERKEO IIB setup and pass several important parts of the experiment. These are briefly described in this section:

Polarizers: Two supermirror polarizers in crossed geometry [Kre05] were used to spin polarize the neutrons perpendicular to their direction of motion. Since we measure correlations with the neutron spin, polarization is a crucial topic of this measurement and explained in more detail in section 3.3.2. Both polarizers were housed in the casemate, a small building with concrete walls of 60 cm thickness, and were additionally surrounded by 10 cm of lead to absorb the γ-radiation emerging in the polarization process.

Neutron Shielding: In this experiment, all areas intensively hit by neutrons were covered with ^{6}LiF since ^{6}Li has a high absorption cross section for neutrons ($\sigma_{n,\alpha} = 949$ b [Nuc95]) in the reaction

$$^6\text{Li} + \text{n} \rightarrow {}^4\text{He} + {}^3\text{H}. \tag{3.4}$$

In some of these reactions an additional γ-quant is emitted but this effect is suppressed by 10^{-4} what makes ^{6}Li the ideal material for low background neutron shielding. However, fast neutrons are also produced with almost the same supression factor. Unfortunately these neutrons are very difficult to shield. We used sintered ^{6}LiF-tiles [Kre04] with a thickness up to 6 mm on heavily irradiated surfaces and ^{6}LiF-rubber (2 mm) to protect from scattered neutrons.

Boron (^{10}B) has an even higher absorption cross section ($\sigma_{n,\alpha} = 3840$ b) but emits a photon in every reaction. For this reason we used boron only in the casemate, far away from the detectors and in areas of the setup where no direct neutron irradiation was present.

Shutter: A beam shutter was placed right after the second polarizer. It consisted of a ^{6}LiF-tile of 5 mm thickness, and was used to close the neutron beam automatically to allow background and calibration measurements.

Vacuum System: Now, the polarized neutrons entered the vacuum system through an 150 μm thick aluminium window. Vacuum is necessary to avoid neutron scattering in air (≈ 5 % per meter) and to enlarge the mean free path of the charged decay products.

Two large turbomolecular pumps (1500 l s^{-1}) were installed on the beamstop tube, one small turbopump was used to evacuate the beamline. An additional cryopump was placed right in front of the spectrometer, but due to technical problems this pump further reduced the pressure only by a factor of two.

The evacuated beamline was surrounded by a weak orthogonal magnetic guiding field to keep the neutrons polarized. Near the spectrometer the guiding field is not neccessary due to the presence of its own field. However, since we wanted to monitor the beam polarization, another guiding field had to be installed around the beamstop tube behind PERKEO II.

Radiofrequency Spinflipper: The spinflipper was the first part of the evacuated beamline used to reverse the neutron spin by 180° on a regular basis. This allowed for a polarization measurement and to reduce detector related effects in the experiment, since it was possible to make the asymmetry measurement with one single detector (the spinflipper provides both spin directions) which is a systematically cleaner method compared to the measurement with both detectors and a fixed spin direction.

Beyond a certain threshold, the flipping efficiency of a radiofrequency (RF) spinflipper [Baz93] is independent of the neutron wavelength and close to unity. This is achieved by a superposition of an oscillating RF-field with an orthogonal static magnetic field that exhibits a field gradient. In the rest frame of the neutron, rotating with the Larmor frequency

$$\Omega = \frac{2}{\hbar}\,\mu_n\mu_N B_0 = \gamma B_0 = -1.832 \cdot 10^8 B_0\,\frac{\text{rad}}{\text{s T}}, \tag{3.5}$$

where $\mu_n\mu_N = -1.913\mu_N$ is the magnetic moment of the neutron, μ_N the nuclear magneton, and B_0 a value of the static field, this superposition leads to a spin rotation.

Collimation System: We had to collimate and shape the neutron beam to guide it through the setup without collisions that would cause severe background problems. Furthermore, it was necessary to limit the beam width in the decay volume to reduce the magnetic mirror effect (cf. chapter 4.5.2). This was achieved by placing five orifices made out of ^{6}LiF-tiles glued onto a lead support in the beam tubes. The first four orifices were installed such that the background produced in the collimation systems is almost invisible in the detectors [Mun06]. However, a fifth orifice closer to PERKEO II had to be installed for this

measurement since the neutron beam was far too broad for a B-measurement. (The initial collimation system was designed for an A-measurement where a larger beam cross-section could be accepted.)

Decay Volume: In the center of PERKEO II the beam had a cross section of $(x \times y) = (53 \times 58)$ mm^2, aluminium baffles limited the decay volume length to $z = 90$ mm. Here we use the standard coordinate system for neutron guides: The neutrons propagate in z-direction, x is the horizontal and y the vertical coordinate; the system is right-handed. The (slightly divergent) neutron beam was homogenious over the length of the decay volume what had been checked using copper-foil activation, a method to directly measure neutron beam profiles (cf. section 3.3.3).

Beamstop: Behind the spectrometer, a large beamstop tube (length: 2.5 m, diameter: 0.8 m), housing the ^{6}LiF-beamstop to annihilate the remaining neutrons, was installed. A shutter opeing a small aperture in the beamstop allowed to monitor the degree of polarization during the measurement.

3.3.2   Neutron Polarization

A neutron beam is called polarized if there is a vector $\mathbf{a}$ with $\langle \mathbf{a} \cdot \boldsymbol{\sigma}_n \rangle \neq 0$, where $\boldsymbol{\sigma}_n$ denotes the neutron spin. In the laboratory frame, polarization P can be treated as a classical vector [NDB02] and the polarization in the direction $\mathbf{a}$ is defined by the relation

$$P_{\mathbf{a}} = \frac{N^{+\frac{1}{2}} - N^{-\frac{1}{2}}}{N^{+\frac{1}{2}} + N^{-\frac{1}{2}}}. \tag{3.6}$$

$N^{+\frac{1}{2}}$ is the number of particles with spin eigenstate $+\frac{1}{2}$ and $N^{-\frac{1}{2}}$ the number with eigenstate $-\frac{1}{2}$. There are two commonly used methods to polarize cold neutrons, we will briefly discuss them in the following. The same methods can be used to analyze the degree of polarization.

Supermirror Polarizers: Cold neutrons can be totally reflected at the surface of most materials (e.g. Nickel) since the vacuum has a higher optical density for neutrons than the materials. Reflection occurs if the incident angle is smaller than a critical angle θ_c which depends on the neutron wavelength λ. This angle can be further increased in supermirrors: In a stack out of several thin layers of two materials with a high and a low neutron optical density respectively (e.g. Nickel and Titanium), assembled in alternating layers of varying thickness, neutrons get Bragg reflected by interference of the partial waves [Sch89]. The integral transmission is increased at the cost of a higher beam divergence.

Supermirror polarizers exploit that the magnetic field $B = \mu\mu_0 H$ inside magnetic materials is much higher than outside creating a potential well for one neutron spin component. If such a material is used as one part of the supermirror, one spin component is Bragg-reflected on the magnetic layer, while the other transits it and is absorbed in the last layer containing Gadolinium: The beam is polarized by sorting out the "wrong" spin direction. Since the neutron beam has a width of a few centimeters the polarizer consists of several supermirrors

next to each other, curved along the beam direction to avoid direct view. Now every neutron has to hit the polarizer at least once, and a previously unpolarized beam leaves polarized.

However, absorption of neutrons with the wrong spin direction in the polarizer (together with a certain fraction of neutrons with correct spin) lowers the neutron flux to 25 % of the incident value [Sch04] and is a strong source of γ-radiation that can cause severe background problems in the detectors. Hence the polarizers are placed inside the concrete casemate and shielded with a large amount of lead. For the B-measurement, we have no effect related to this background.

Polarizers in Crossed Geometry: This method was developed to increase the absolute value of neutron polarization and to gain a uniform polarization over the whole beam cross section and wavelength spectrum (see details in [Kre05]). A second supermirror polarizer is rotated by 90° and placed behind the first; the magnetic field between the polarizers is turned adiabatically to ensure that the neutron spins can follow. Now, the polarizers are independent of each other and polarize in perpendicular directions. A neutron with the wrong spin component that is still reflected in the first polarizer has thus a much higher probability to get absorbed in the rotated polarizer compared to another one in parallel orientation. The second polarizer reduced the beam intensity by another factor of two.

^{3}He-Cells: Another possibility to polarize cold neutrons is to use polarized ^{3}He-cells as opaque spin filters [Sur97, Zim99]: Such a cell is transparent only for neutrons which have their spins aligned parallel to the nuclear helium-spins due to a strongly spin dependent absorption cross section. Unfortunately, this also depends on the neutron wavelength λ and the cell pressure p, thus a "white" neutron beam has to be restricted to a small wavelength band by using a monochromator to be polarized.

Approaching the opaque wavelenth region of the ^{3}He spin filter, neutron transmission gets very poor but the polarization P given by

$$P(\lambda) = \tanh(\mathcal{P} k p \ell \lambda) \tag{3.7}$$

increases up to unity. $\mathcal{P}$ is the helium polarization, $k = 0.0733$ bar^{-1} Å^{-1} cm^{-1}, p the cell pressure, and ℓ the cell length. For example, typical numbers would be $\mathcal{P} = 50$ %, $p = 3.5$ bar, $\ell = 10$ cm resulting in $P(4\text{Å}) = 0.99993$. This makes ^{3}He-cells an ideal analyzing tool for absolute polarization measurements.

Polarization in this Experiment: For the PERKEO IIB experiment we used two supermirror polarizers in crossed geometry and a radiofrequency spinflipper. Beam polarization was measured with a second radiofrequency spinflipper and two smaller supermirror polarizers ("analyzers"), again in crossed geometry. For the precise measurement of the polarization, several opaque polarized ^{3}He cells were used. A mechanical chopper allowed for a wavelength dependent analysis; polarization homogeneity over the full beam was measured by moving the whole analysis setup.

With two supermirror analyzers one can only obtain APF, the product of polarization P, analyzer strength A, and flipper efficiency F. The latter can be measured independently,
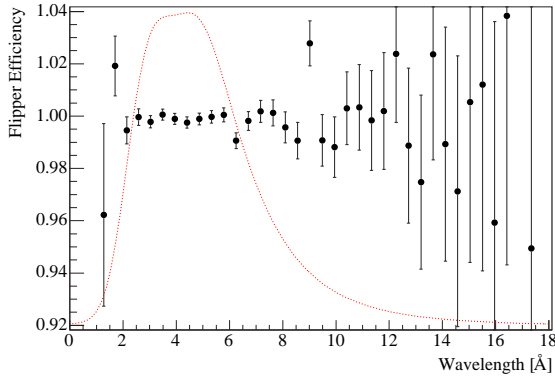
Figure 3.3: Efficiency of the radiofrequency spin-flipper used in the experiment: It is $F = 1.000(1)$ in the range from 2 to 12 Å. The dottet curve indicates the $1/v$-weighted neutron spectrum in arbitrary units.

however, since we do not know the analyzer efficiency A, we only get an approximate result:

$$P \approx \sqrt{AP}. \tag{3.8}$$

This relative measurement was supplemented by an absolute polarization measurement using several ^{3}He-cells (for different wavelengths) with $A = 1$ in a certain wavelength range. During the asymmetry measurements the spin flip ratio

$$R = \frac{N_{\text{on}}}{N_{\text{off}}} \tag{3.9}$$

was monitored using one supermirror analyzer (which is only transparent for neutrons with a certain polarization) and a ^{3}He neutron counter; N_i is the number of neutrons measured with the spinflipper on or off respectively: A ratio R changing in time is a signal for a changing degree of polarization. During this experiment R was constant.

Since the mathematical description of the polarization analysis was already discussed in detail in many theses (e.g. [Rei99, Sch04, Kre04b]) we will skip this here and just give the results.
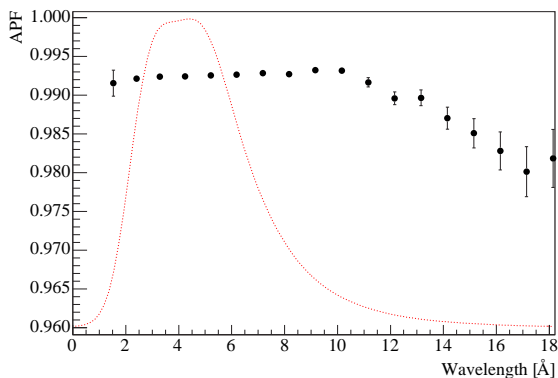

Figure 3.4: Product of polarization P, analyzer efficiency A, and flipper efficiency F measured in the center of the beam. Since $P \approx A$ and $F = 1$, $\sqrt{APF}$ is a good measure for the polarization P. It is flat in the neutrons' wavelength band.
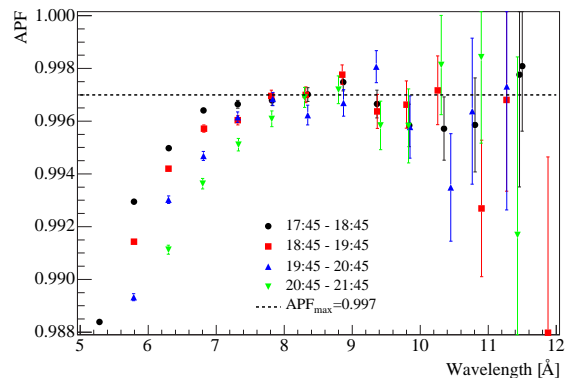
Figure 3.5: Typical APF measurement with a single ^{3}He-cell in different time intervals. According to eq. (3.7), the analyzing efficiency is $A \rightarrow 1$ for $\lambda \rightarrow \infty$, which yields $P_{\text{max}} = 0.997$ with $F = 1$. Several cells were used to analyze the whole spectrum.

Some plots of the measurements are shown in figures 3.3−3.5: The flipping efficiency is $F = 1.000(1)$ between 2 and 12 Å, the polarization was measured to be $P = 0.997(1)$ in the same wavelength region. Furthermore polarization is constant over the full beam cross section. With two supermirror polarizers in crossed geometry, neutron beam polarization is no longer a limiting factor in correlation coefficient measurements.

Influence on the measured Spectra: In an experiment with ideal polarizer ($P = 1$) and ideal spinflipper ($F = 1$) the electron count rates[3] $N_{\mathrm{on/off}}$ for the two flipper modes coincide with the count rates $N_{\uparrow/\downarrow}$ of certain neutron spin directions:

$$N_{\mathrm{off}} = N_\uparrow \quad \text{and} \quad N_{\mathrm{on}} = N_\downarrow. \tag{3.10}$$

For the opposite detector, $N_\uparrow$ and $N_\downarrow$ have to be interchanged, however, since the formalism is identical we will omit it here. The detailed derivation can be found in [Kre04b].

The experimental asymmetry B_{exp} is defined by the ratio of difference D and sum S of these count rates:

$$B_{\mathrm{exp}} = \frac{D}{S} = \frac{N_\uparrow - N_\downarrow}{N_\uparrow + N_\downarrow} = \frac{N_{\mathrm{off}} - N_{\mathrm{on}}}{N_{\mathrm{off}} + N_{\mathrm{on}}}. \tag{3.11}$$

However, with $P \neq 1$ and $F \neq 1$, the equalities in (3.10) no longer hold and the measured spectra $N_{\mathrm{off/on}}$ become linear combinations of $N_{\uparrow/\downarrow}$:

$$N_{\mathrm{off}} = \frac{1}{2}\left((1+P)N_\uparrow + (1-P)N_\downarrow\right) \tag{3.12}$$

$$N_{\mathrm{on}} = \frac{1}{2}\left((1 - P(2F{-}1))N_\uparrow + (1 + P(2F{-}1))N_\downarrow\right). \tag{3.13}$$

If we insert this into equation (3.11) we obtain the expressions for the spectra measured with an imperfectly polarized neutron beam:

$$D = N_{\mathrm{off}} - N_{\mathrm{on}} = FP(N_\uparrow - N_\downarrow) \tag{3.14}$$

$$S = N_{\mathrm{off}} + N_{\mathrm{on}} = \left(1 + P(1{-}F)\frac{N_\uparrow - N_\downarrow}{N_\uparrow + N_\downarrow}\right)(N_\uparrow + N_\downarrow) \tag{3.15}$$

$$B_{\mathrm{exp}} = \frac{N_{\mathrm{off}} - N_{\mathrm{on}}}{N_{\mathrm{off}} + N_{\mathrm{on}}} = \frac{FP(N_\uparrow - N_\downarrow)}{(N_\uparrow + N_\downarrow) + P(1{-}F)(N_\uparrow - N_\downarrow)}. \tag{3.16}$$

The difference spectrum D just gains an additional scaling factor FP, but in case of the sum S and the asymmetry B_{exp} the spectral shape is altered due to the mixing of the two polarization states. This has to be taken into account in the fit functions for the asymmetry analysis (cf. sections 4.6 and 4.7).

3.3.3 Magnetic Mirror Effect and Neutron Beam Alignment

To measure the neutrino asymmetry with high-precision and small corrections it is necessary that neutron beam n and magnetic field B are aligned in the decay volume. To achieve this,

---

[3]In the experiment, the count rates $N_{\mathrm{off/on}}$ of the charged particles are functions of the electron's kinetic energy E, i.e $N_{\mathrm{off}}(E)$ and $N_{\mathrm{on}}(E)$. The same holds for the spectra D, S, and B_{exp}. For simplicity, we omit this dependence in the notation.
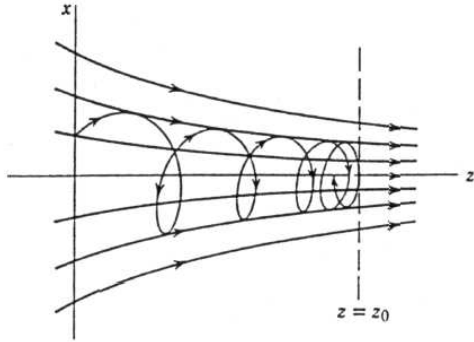
Figure 3.6: The magnetic mirror effect is a well known phenomenon occuring for charged particles moving in inhomogeneous magnetic fields: Particles emitted in a region of a low magnetic field, that move against a positive field gradient, may be reflected. The effect depends on the initial angle θ between particle momentum and magnetic field lines. Figure taken from [Jac02].

shape and maximum of the field were determined using a Hall-probe. The neutron beam profile, which could be changed in shape and position by varying the last collimation orifice, was measured with copper foil activation analysis and aligned with the magnetic field. This procedure is called *B-n-Scan*.

Magnetic Mirror Effect: The motivation for the laborious *B-n*-Scan is the magnetic mirror effect [Jac02], an important correction on the electron spectra in PERKEO II measurements: For a charged particle in an inhomogeneous magnetic field B the quantity

$$M = \frac{p_\perp^2}{B} \tag{3.17}$$

is an adiabatic invariant, where

$$p_\perp = \sin\theta \ \frac{1}{c} \ \sqrt{E^2 - m^2 c^4} \tag{3.18}$$

is the particle's momentum perpendicular to the magnetic field lines and θ the angle between field vector and momentum.

In a field decreasing from $B_{\max}$ to B_1 this results in a momentum transfer from the normal to the parallel component of motion, $p_\parallel$ gets larger, and the new angle is

$$\sin\theta_1 = \sin\theta_{\max} \ \sqrt{\frac{B_1}{B_{\max}}}. \tag{3.19}$$

If the particle moves in an increasing field, equation (3.19) is still valid but $p_\parallel$ decreases and, for initial angles

$$\theta_1 > \theta_{\mathrm{crit}} = \arcsin\sqrt{\frac{B_1}{B_{\max}}}, \tag{3.20}$$

$p_\parallel$ even changes sign: An electron emitted towards detector 1 can be reflected at the magnetic field and generate a signal in the opposite detector. This is illustrated in figure 3.6. In general, this does only depend on the initial angle θ and not on the particles energy. However, the spectra are angle dependent due to the anisotropic particle emission, and the mirror effect distorts them, what gives rise to corrections. Details on determination and implementation of the correction functions can be found in section 4.5.2.
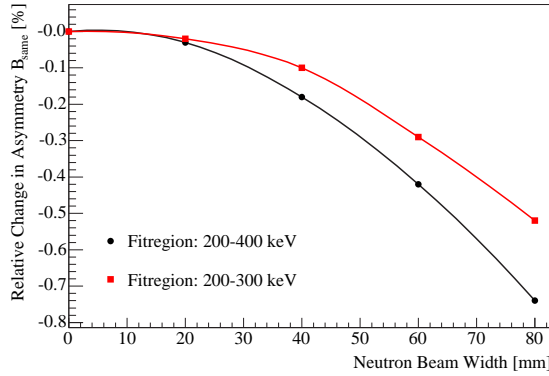
Figure 3.7: Impact of the neutron beam width on the neutrino asymmetry B_{same} (same hemisphere) due to the magnetic mirror effect. (Figure is based on data of [Rei99]).
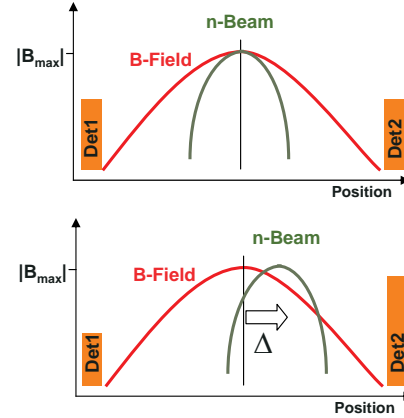

Figure 3.8: Illustration of the effect of a misalignment Δ between neutron beam and magnetic field: The number of electrons increases in the detector closer to the beam and decreases in the other one.

There are two kinds of corrections related to the magnetic mirror effect: The first is a relative change in the asymmetry since the magnetic field has a maximum in the spectrometer center and decreases over the neutron beam width d. Hence the mirror effect is always present – even if B and n are perfectly aligned – but can be diminished by reducing the overall beam width (see figure 3.7): We chose a medium width of $d = 50$ mm. The second correction occurs when magnetic field and neutron beam are not aligned but displaced by a distance Δ, e.g. consider the case where the whole beam is located next to the field maximum (figure 3.8). Now, the mirror effect is very different for both detectors: The count rate is increased in the first and lowered in the second detector. However, these relative changes cancel if we can average over both detectors. Moreover, as can be seen in figures 3.9 and 3.10, the mirror effect is only important for the asymmetry B_{same} where electron and proton are detected in
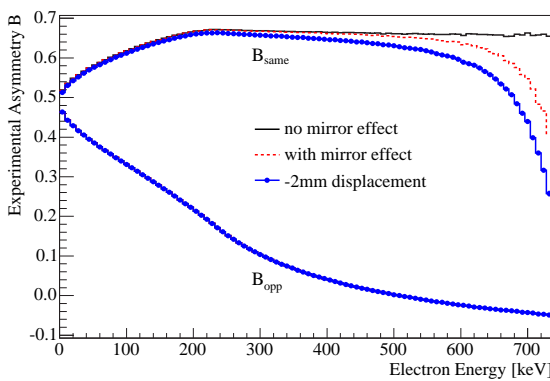

Figure 3.9: Simulation of the impact of the magnetic mirror effect on the experimental neutrino asymmetry B: The asymmetry B_{same} with electron and proton detected in the same hemisphere is strongly affected, whereas B_{opp} is hardly changed at all, all three curves coincide.
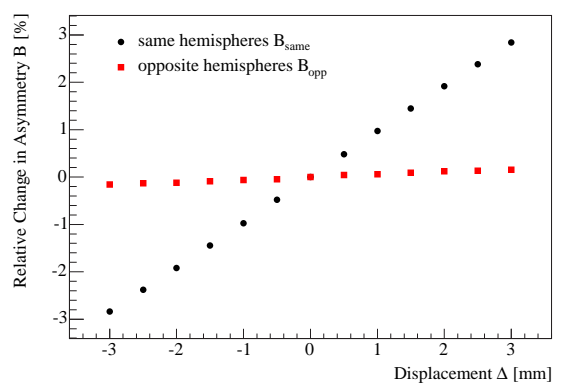

Figure 3.10: Effect of a displacement Δ between neutron beam and magnetic field: For B_{opp} it is negligible but B_{same} is strongly affected. However, since the effect on both detectors differs only in sign, it is canceled when averaging over both detectors.

the same hemisphere; it can be almost neglected for an asymmetry measurement in opposite hemispheres (B_{opp}). The impact on the proton asymmetry C is also small. Throughout this text, we use the convention that a positive displacement Δ indicates the beam to be closer to detector 2.

Magnetic Field Scan: To align magnetic field and neutron beam we had to determine the shape and the maximum of PERKEO's magnetic field first. This was done with a three axis Hall probe that could be moved in all three dimensions with step motors to scan the whole decay volume. Since it is not exactly known where the Hall plate is fixed in the probe the scan was repeated with the probe turned by 180°.

We measured a symmetric, parabula shaped magnetic field B with the expected maximum of $B_{\mathrm{max}} = 1.03$ T. Size and shape agree within 0.3 % with a finite elements calculation of PERKEO II [Mae05]. To simulate the magnetic mirror effect we use the quadratic expression for the field in the decay volume suggested by [Rei99],

$$B(x) = B_{\mathrm{max}} \left(1 - \left(\frac{x}{\ell} \right)^2 \right),$$ (3.21)

but choose the field parameter to be $\ell = 690$ mm [Dei05], which agrees much better with the measurements and the calculation than the values used in previous measurements. The value of the horizontal maximum determined from the measured data is independent of the vertical position (y).

Neutron Beam Scan: Copper foil activation (cf. e.g. [Kre04]) is a fast and precise way to determine the size and shape of a neutron beam: A thin ($\approx 150 \ \mu$m) copper foil is irradiated with neutrons for about 30 minutes to activate the nuclei ^{63}Cu and ^{65}Cu to ^{64}Cu ($\tau = 18.3$ h) and ^{66}Cu ($\tau = 7.4$ min). After activation, the foil stays untouched for half an hour to let the ^{66}Cu decay. Then it is put onto an imageplate. Electrons emitted in the decay of ^{64}Cu are recorded and generate a two-dimensional intensity picture of the neutron beam. As example, figure 3.11 shows the cross section of the neutron beam in the decay volume center.

x and y projections of figure 3.11 take into account the whole profile and allow a precise analysis of the neutron beam shape: The x-profile, figure 3.12, is almost symmetric and
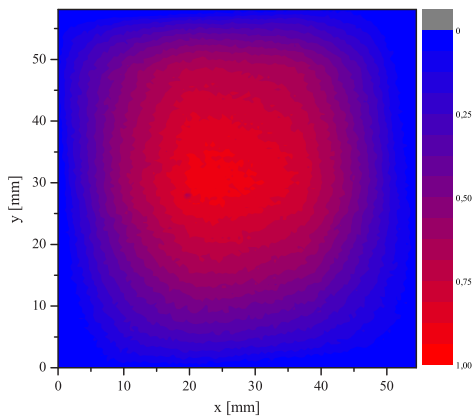

Figure 3.11:   Two-dimensional neutron beam profile in the decay volume center measured with copper foil activation. Cuts through the figure allow a quantitative determination of beam shape and barycenter.
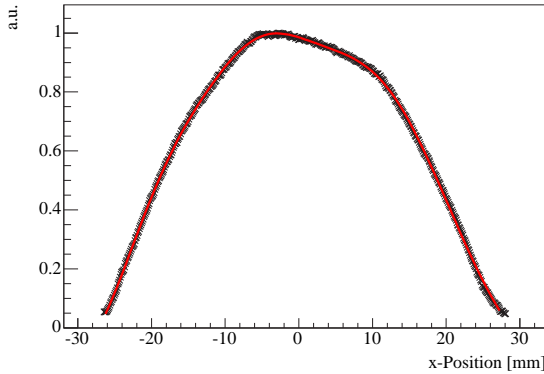
Figure 3.12: Projection onto the horizontal (x) axis of figure 3.11. The beam is symmetric within 0.4 % and can be well described by a sum of three Gauss functions (red curve). Its barycenter was shifted to the origin of the axis.
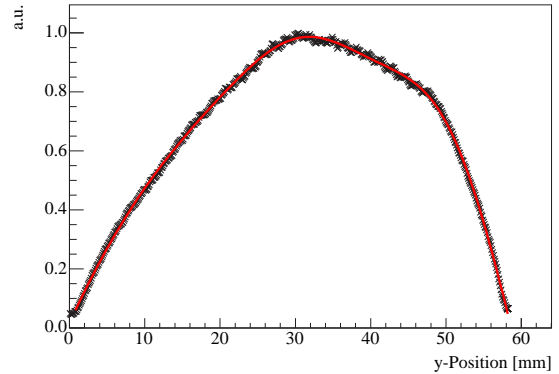
Figure 3.13: Projection onto the vertical (y) axis of fig. 3.11. Its asymmetric shape is not critical for the mirror effect but has to be taken into account for detector calibration. A sum of three Gauss functions is used for an analytical description.

shows only a tiny asymmetry of 0.4 % on the positive x-side (detector 2). However, instead of the beam maximum, the beam's barycenter x_0 has to be aligned with the maximum of the magnetic field.

We managed to align the neutron beam with the magnetic field with a final displacement of

$$\Delta = (1.0 \pm 1.4) \text{ mm}, \tag{3.22}$$

where the uncertainty is due to the size of the laser spot (1 mm) that was used to provide a fixed reference point in the spectrometer. A sum of three Gauss functions is used to describe the projections analytically. This is necessary to implement the beam shape in simulations of the magnetic mirror effect (see chapter 4.5.2). The asymmetry of the y-projection (fig. 3.13) is not critical for the mirror effect but very important for the electron detector calibration (cf. section 4.1.5).

3.4 Detection System

Since we cannot measure neutrinos directly to obtain the neutrino asymmetry B, we have to detect electrons and protons coincidently from the decay to reconstruct the neutrino's emission direction. This section describes the core of PERKEO IIB, the combined electron-proton detector, a setup that allows to detect electrons and protons using the same detector. Only this enables us to measure the statistically and systematically favoured correlation B_{same}.

3.4.1 Combined Electron-Proton Detector

The difficulty to detect electrons e^- and protons p with one single detector is their difference in kinetic energy of three orders of magnitude,

$$E_{\max}(e^-) = 782 \text{ keV} \quad \text{and} \quad E_{\max}(p) = 780 \text{ eV}. \tag{3.23}$$
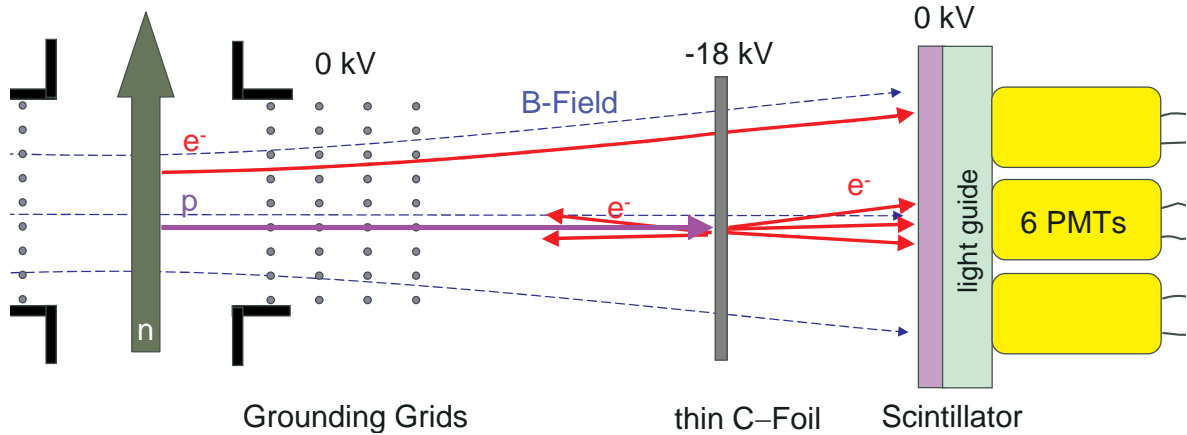
Figure 3.14: Sketch of the the combined electron-proton detector: Protons are converted into electrons by a thin carbon foil on negative high voltage. A large grounded plastic scintillator detects these secondary electrons and the electrons from the decay. Thin aluminium wires on ground (0 kV) shield the decay volume from a reach-through of the high voltage potential. Only one side of the symmetric detection system is drawn, and the particle trajectories omit the gyration around the field lines.

Commonly used proton detectors such as PiN-diodes, multichannel plates, and surface barrier detectors cannot detect electrons with sufficient energy resolution. Moreover, the detector has to be quite large (≈ 250 cm^2) to cover the whole decay volume. Futher requirements on the detector are a rather small proton time-of-flight to allow a coincident electron-proton measurement, a detection efficiency that is energy and angle independent for both charged particles, and last but not least, the system has to work in an evacuated environment with a strong magnetic field.

Our solution is a detector developed by [Rei99] and [Kre04b] applying a method described in [Kra66, Dob75, Str78]. Figure 3.14 illustrates the principle, displaying only one half of the symmetric detection system.

Electron Detector: We detected the electrons with a standard plastic scintillator (Bicron BC-404) of dimensions 130×190 mm^2. Its thickness of 5 mm was chosen to ensure that the 1 MeV-electrons of the calibration peak loose all their energy in the scintillator. A 30 mm thick lightguide made out of plexiglass (Bicron BC-810) with the same refraction index than the scintillator, directly glued to the scintillator with optical cement (Bicron BC-600), was used to distribute the scintillation light onto a larger area. Finally, the photons were detected in six mesh photomultipliers[4] (Hamamatsu R5504). These are the only photomultipliers (PMT) that work in magnetic fields greater than 0.5 T, provided that they are installed with the correct angle towards the magnetic field lines [Plo00]. All free detector surfaces at the side and the back were covered with diffuse reflecting paint (Bicron BC-620) to increase light output, and the whole setup including photomultipliers was placed within the vacuum vessel. It fulfilled our needs in terms of stability, linearity, homogeneity (cf. section 4.1),

---

[4]In contrast to ordinary photomultipliers employing a series of dynodes for electron amplification, mesh photomultipliers consist of several fine meshes directly behind each other to amplify the signal. This allows to use them in high magnetic fields, however, their quantum efficiency is usually lower than for dynode-tubes.

and low sensitivity to γ-radiation from the background. Furthermore, the fast scintillator-photomultiplier combination allowed a time resolution of about 1 ns.

Proton Detector: The protons were accelerated onto a thin $(15-30~\mu\mathrm{g}~\mathrm{cm}^{-2})$ carbon foil [Sto02] on negative high voltage (about -18 kV) that was placed between decay volume and scintillator. Whereas the electrons transit the foil almost unperturbed, the accelerated heavy protons have enough ionization power and total energy to release one or more secondary electrons from the foil. These get again accelerated by the negative potential U and depose the corresponding energy in the scintillator. Hence the foil works as a "proton to electron converter". Detailed studies have shown that the proton conversion is independent of energy and incident angle on the foil for values ocurring in the PERKEO II setup [Bra00]; the same holds for the electron detection in the scintillator.

Generally we applied a high voltage of $U = -18$ kV to both detector foils. However, the high voltage had to be ramped up slowly and sometimes the desired value was not reached due to severe high voltage related background accompanied by electric sparkovers. We even operated the system several days with different voltages on both sides $(\Delta U_{\mathrm{max}} = 2$ kV) for stability reasons. Although former tests with this setup were performed with voltages up to -30 kV [Rei99] we never succeeded to get beyond -20 kV. The difference is probably due to the strong magnetic field that was not present during the tests.

Scintillator and decay volume had to be grounded: The first to accelerate the secondary electrons towards the detector by repulsion from the foil, the second to inhibit changes of the initial angular distribution of the particles in the decay volume due to the electric potential. Additionally, the energy of the decay electrons should not be affected, they should therefore start and stop on the same potential.

We covered the scintillator front with a thin layer (50 nm) of aluminium and connected it to ground potential. In case of the decay volume, we used 4 layers of thin linear aluminium grids for shielding. The wires of the two inner grids (towards the neutron beam) had a diameter of $d = 10~\mu$m, the others $d = 25~\mu$m with a spatial distance of 6 mm between the wires on a grid and 15 mm between subsequent grids; the reason for this choice will be given in the next section. Figure 3.15 shows a photograph of the setup.
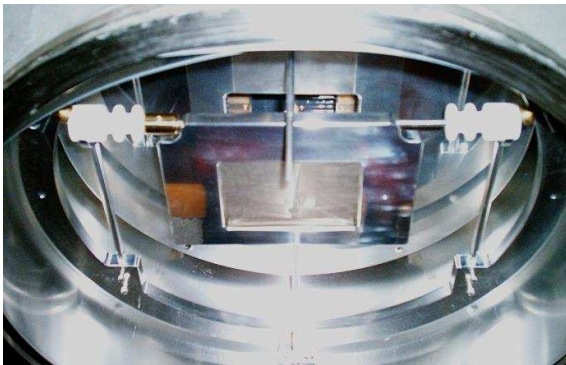

Figure 3.15: Photograph of the proton-to-electron converter: In the foreground one can see the thin carbon foil set to negative high voltage. The decay volume (not visible) is shielded with polished aluminium plates; only a small rectangular aperture allows the charged particles to reach the detector. Four grid-layers made out of thin aluminium wires ground the decay volume; the first is visible in the back. Behind the grids one can see the vertical baffles that define the decay volume length.
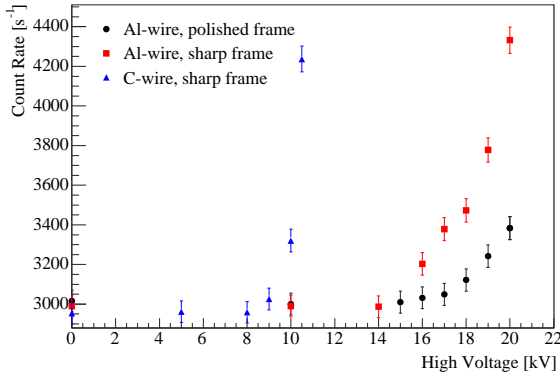
Figure 3.16: Results of test measurements for the detection system: Shown is count rate vs. high voltage for different setups. The high voltage related background depends not only on the type of wires used to shield the decay volume but also on the condition of their support. We chose 25 μm Al-wires in a specially prepared support for the real experiment (black dots).

3.4.2   High Voltage Test Measurements

The first experiment to measure B and C with PERKEO II was performed in the year 2000 [Kre04b, Kre05b]. It used the same detection principle but had to face some severe difficulties that limited the precision of the result significantly. One of the crucial points was the high voltage related background and its instabilities what may be caused by the extremely thin carbon wires that were used to ground the decay volume in that experiment: Very high electric fields occuring in the neighborhood of the wire surfaces may ionize residual gas atoms that then generate triggers in the detection system. Another problem arose due to the low proton efficiency: To increase it, the coincidence condition "2 out of 6", i.e. an event is only considered to be valid if at least two from the six photomultipliers per detector trigger, was omitted in the proton branch of the electronics (cf. also section 3.4.4). Unfortunately, the photomultipliers tend to show after pulses some time after an initial signal. These pulses were difficult to eliminate as they had the same signature as protons.

We have considered these experiences in the preparations for the new PERKEO IIB measurement, and therefore made some test measurements on the high voltage system at the ILL. The test setup was similar to the real one (without magnetic field) and consisted of an old electron detector from the last measurement that was read out by two photomultipliers, a carbon foil on high voltage, and a grid that was used for grounding purposes. A weak ^{207}Bi electron source allowed to calibrate the measurements.

Especially the grounding grids – the possible origin of the HV-background – were studied copiously. Some results are shown in figure 3.16: High voltage effects depend strongly on diameter and material of the wires, as well as on the condition of their support frame. We achieved the lowest count rates in a setup with 25 μm AlSi-wires[5] on a frame that was completely hidden in a polished aluminium cover. The difference to the much thinner (8 μm) carbon wires used in the year 2000 is quite remarkable, hence, for the real experiment, we decided to use 25 μm AlSi-wires for the two outer grids and 10 μm AlSi-wire for the inner ones, where the electric potential is already much lower. However, the effect of the finite wire size acting as an obstacle to the particles has to be taken into account; this is referred to as the grid effect (cf. section 4.5.6). To reduce the HV-background even further all parts of the new detection system that had direct sight to the high voltage foil were specially polished to avoid tiny metal spikes.

---

[5] 99 % Al, 1 % Si

3.4.3 Electric shielding of the Decay Volume

An important point regarding the combined electron-proton detection system is to shield the decay volume from the potential of the foils, since this could severely disturb (especially if the potential is asymmetric) the initial momenta of the charged particles. Detailed studies on this topic have been made in the past [Rei99, Bra00] generating the following results:

- In an **asymmetric setup**, i.e. different voltages applied to the foils, the overall change of the potential Φ in the decay volume should be below $\Delta\Phi = \Phi_{max} - \Phi_{min} < 1$ mV.

- For a **symmetric setup** the limit can be higher since the effect of deflecting charged particles onto the wrong detector is partly compensated by the second foil. Here the relative change should be $\Delta\Phi < 100$ mV in order to not have a significant effect on the asymmetry measurement. However, the absolute potential in the decay volume could be larger. For these reasons we operated the system only in the symmetric setup.

Anyhow, we repeated the old electrostatic simulations with enlarged CPU power to ensure that the electric field is no limiting factor in the PERKEO IIB experiment. Both, analytic calculation and direct measurement are not possible here.

Simulation of the electric reach-through is also very complicated due to the extremely small diameter of the grounding grids compared to the overall dimensions. Altogether three simulations of the realized setup (cf. section 3.4.1) have been done to tackle the problem:

- Ferenc Glück [Glu05] performed a simulation with his new method using surface charges.

- Torsten Soldner [Sol05] wrote a program to solve the Maxwell equations with the finite element method on a cubic grid and studied effects of the grid constant.

- We used the commercial finite element program *EM Studio* from CST[6] to simulate the setup (with the friendly assistance of Bastian Märkisch): In the most accurate simulation run we used approximately $3.6 \cdot 10^6$ three-dimensional mesh cells. Fortunately we only had to simulate one eighth of the interesting volume for symmetry reasons. The finest mesh (0.3 mm) was placed between the grounding wires, in the outer parts of the simulation it was rather coarse with equilibrated transitions between the different mesh sizes. But still even the finest mesh was 10 times larger than the wires used for grounding. Hence the absolute values obtained in the simulation are only lower borders.

Figure 3.17 shows the results of the latter simulation: It gives the absolute electric potential Φ on the symmetry axis connecting the detectors where we expect the highest values. The effect of the grounding grids can be clearly seen and the maximum potential at the decay volume border is below $\Phi = 8$ mV. The change in the potential is below $\Delta\Phi = 1$ mV what is two orders of magnitude smaller than demanded by the studies quoted above.

Since the other two simulations yield similar results we conclude that the relative change in the potential $\Delta\Phi$ and even the absolute potential Φ of our setup are well below $\Delta\Phi_{max} = 100$ mV. Of course we have to consider the numerical limitations of the simulations but we do not expect them to change the results by more than an order of magnitude what is still below the necessary threshold.
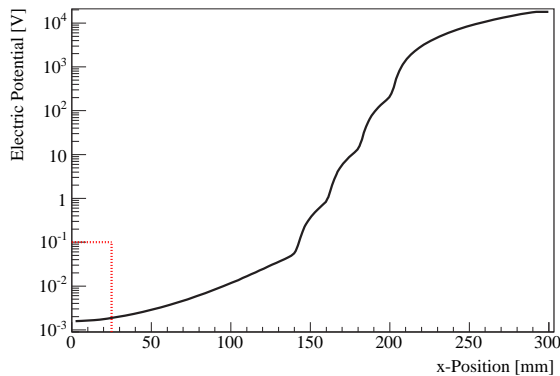
---

[6]CST GmbH, Darmstadt; `www.cst.de`

Figure 3.17: Reach-through of the electric potential: The result was obtained using *EM Studio*, a commercially available simulation program for electric and magnetic fields. It shows the absolute electric potential Φ on one half of the line connecting both detectors. In the decay volume (red box) the potential is well below the desired value. In the simulation, the foil is at $U = -18$ kV, the steps between 150 and 200 mm are due to the grounding grids. Please note the logarithmic scale.

3.4.4 Data Acquisition

We recall that the method of determing the neutrino asymmetry B is to measure the momenta of electron and proton from a single decay in coincidence. Hence data acquisition must fulfill certain conditions:

- To allow for different cuts and conditions in data analyis, each event should be recorded with all available information ("event mode data") instead of just measuring spectra.

- We have to detect the electron's energy signal which is also used as "start" signal of the coincidence measurement.

- Since the proton is heavier and moves slower than the electron, it occurs after the electron trigger: Thus is is detected it as "stop" signal within a certain coincidence window.

- To deal with high voltage background and accidential coincidences, several stop signals should be measurable within the coincidence window; the energy content of the first four should be stored.

- The global time of an event ocurring during the measurement should be recorded to be able to look for false periodic structures.

- A fast timing measurement within an event is necessary to measure electrons that depose only a part of their energy in the first detector and get backscattered to the other detector (guided by the magnetic field lines). For full energy reconstruction the ADCs of both detectors were read out simultaneously whenever a trigger occurs.

Data acquisition was realized with VME modules and PC readout, a CAMAC discriminator, and standard NIM logic devices[7]. The incoming signals to deal with were 12 analog photomultiplier signals that were split by a linear fan: One signal was delayed by 200 ns and fed to a charge integrating input of the ADC (CAEN V792N), the other entered a constant fraction discriminator (CAEN C808). The digital outputs for each detector were sent to a "2 out of 6" coincidence unit triggering only if at least two of the six photomultipliers per detector

---

[7]This are commonly used electronics standards: VME stands for *Versa Module Euro card*, CAMAC for *Computer Aided Measurement and Control*, and NIM for *Nuclear Instrument Module*.
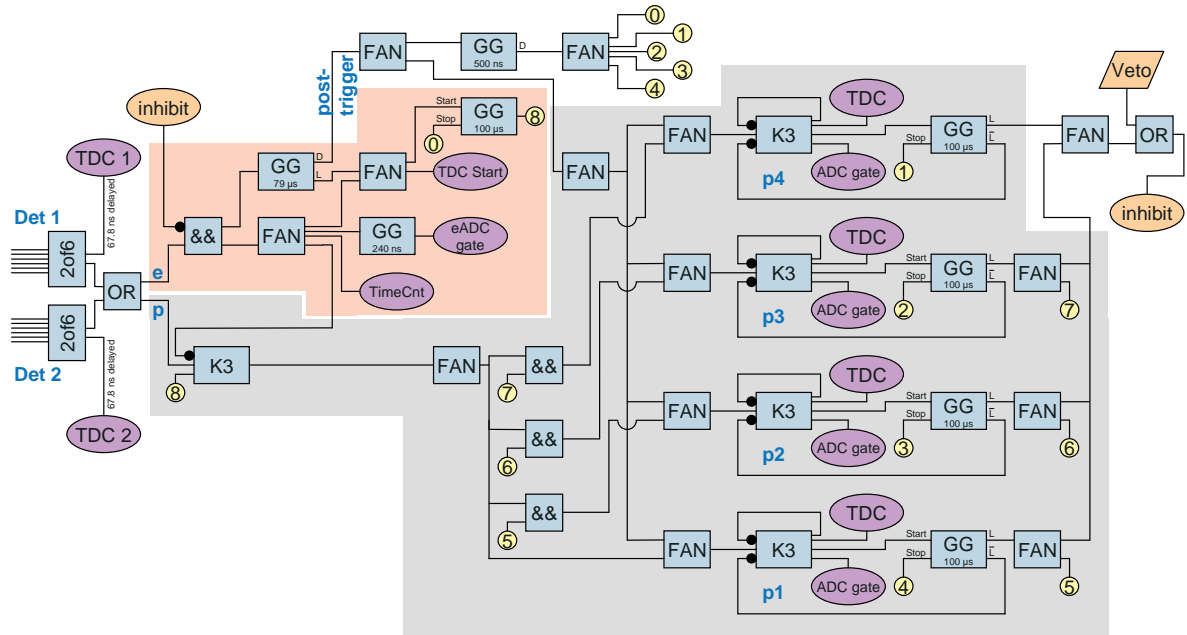
Figure 3.18: Logic part of the data acquisition electronics to measure the energy signal of the electron and up to four coincident stop signals: The 2×6 signals from the discriminator enter the logic from the left. Rectangles (turquoise) indicate standard NIM logic modules, ovals (violet) VME modules, circles (yellow) with equal numbers and *inhibit* symbolize connections, and *Veto* abbreviates the sum of all VME busy signals. The red shaded part is the electron logic, the grey part for the proton, and the "post-trigger" branch served to finish the event after 80 μs. The following abbreviations are used: &&: logic AND module, *FAN*: OR module with several inputs and outputs, *K3*: threefold coincidence unit, *GG*: gate generator that creates a gate of the indicated length t (L-output) if it is not stopped in advance via the stop-input, its D-output generates a short NIM-pulse after a delay-time t.

have detected a signal. This is the first stage of the digital logic part shown in figure 3.18: It is divided in an electron part that starts an event and ensures that all devices got a trigger at the end of the 80 μs coincidence window, even if nothing happened after the start. This "post-triggering" is necessary to ensure that all devices have registered the same number of events, otherwise event-reconstruction is impossible. The proton part of the logic triggered different ADCs (DL 642[8]) to measure the energy of the first four stop signals.

For timing measurements within an event we used a TDC with 0.8 ns resolution (CAEN V676A). This is good enough to measure backscattering effects since the minimal flight time for electrons from one detector to the other is about 3 ns. TDC-measurements were made relative to a global time window started by the electron part of the digital logic. Triggering of two separate TDC-channels for the detectors was done directly by the "2 out of 6" modules. So up to 32 stops for each detector could be measured. Another TDC (DL 643A) with a much lower time resolution (1 μs) allowed to determine the time of an event within a cycle, which is the shortest measurement unit (2 s) between two spin-flipper turns. A timing-module (ILL StartStop) for automatic dead time correction and several counters completed the data

---

[8]The "DL" modules were developed and manufactured by the electronics workshop of the Physics Institute (PI), University of Heidelberg.

acquisition system that was also used to control the experiment, i.e. to switch spin-flipper, move shutters (for background measurements) and calibration sources according to a fixed scheme. Details on the detector calibration follow in the next section.

3.4.5   Detector Calibration

Whereas the neutrino asymmetry B_{same} in the same hemisphere is almost not sensitive to detector calibration due to its flat distribution, detector calibration is crucial for the measurement with opposite detectors B_{opp}, and the proton asymmetry C. In this section we will just mention the efforts made to characterize the detectors precisely, the results of detector performance are presented in section 4.1.

We used five monoenergetic conversion electron sources covering the whole energy region of neutron decay with six peaks[9] since ^{207}Bi shows two:

	^{109}Cd	^{139}Ce	^{113}Sn	^{137}Cs	^{207}Bi	
Half Life $T_{1/2}$	462.6 d	137.2 d	115.1 d	30.2 a	32.2 a	
Peak Position [keV]	78.1	136.6	371.9	629.3	504.7	997.9

We applied the sources onto very thin carbon foils ($\approx 12\ \mu\mathrm{g/cm}^2$) to minimize energy loss in the foil transit. Unfortunately, the inner diameter of the support structure for the foils was chosen too small (15 mm) for the upper Bi-peak: Electrons with energy E_e (in units of the electron rest mass) in a magnetic field B (in T) gyrate around the field lines with a maximal radius

$$r_{\max} = \frac{1.70\sqrt{E_e(E_e+2)}}{B}\ \mathrm{mm\ T}, \tag{3.24}$$

when they are emitted perpendicular to the magnetic field. For bismuth in the field of PERKEO II ($B = 1.03$ T), this yields $r_{\max} = 4.6$ mm, but since an undisturbed gyration needs a free space of $2\,r_{\max}$ around the source center, a certain fraction of the electrons collide with the support. However, this concerns only the upper Bi-peak leading to an overall intensity loss but no spectral distortion, since all individual lines are effected the same amount. Hence the ratio of both Bi-peaks is changed without any impact on the calibration.

Additionally, one has to remember the γ-background generated by the daughter nuclei of the sources and photons from compton scattering. This cannot be removed from the spectra in the calibration and may yield a shift of the peak positions.

Calibration Plates: After installation of the electron detectors, we adjusted the photomultiplier tubes with calibration signals emitted from a plate equipped with six Bi-sources each positioned exactly in front of a photomultiplier tube. This facilitates an equal calibration of all tubes simultaneously, whereas the signal depends on the PMT-positions if only one single source is used.

---

[9]In reality the peaks consist of up to 20 individual lines of conversion electrons from different shells and additional Auger electrons with different energies (cf. e.g. [Met95]). But due to the low energy resolution of the plastic scintillators and PERKEO's magnetic field, that collects all electrons, one can sum up these lines to one peak. However, the fit functions incorporate all of the individual lines.

Calibration Carousel: Placed in between the detectors, this device consists of two turnable half plates with three particular calibration sources each. In "normal" position, the sources are shielded with lead and cannot be seen by the detectors. By turning one of the half plates by $90°$, $180°$, or $270°$, one source is placed right in the decay volume center, the others are still invisible.

We used the carousel regularly within a fixed measuring scheme to calibrate the detectors with all sources (rate $300-1000$ e^-/s) to avoid drift effects in the detector function. For the calibration of the proton ADCs, random coincidences, i.e. several electrons inside the coincidence window, were used. To get them in sufficient amount, a strong ^{207}Bi source ($\approx$ 7 kHz) was mounted in the sixth position. However, the energy-channel-relation determined with the calibration carousel has to be corrected since the sources were positioned in the center whereas the neutrons decay in the whole decay volume and the decay products cover the whole detector.

Scanner: The scanner was used to determine this correction: It allows to move a single calibration source two-dimensionally between the detectors, covering the whole decay volume projection. The motion in vacuum and in the high magnetic field of PERKEO II was realized by using piezo micro-motors from *Nanomotion* (cf. [Bre03, Sch04]).

We performed the scanner measurement three times ($2 \times$ ^{207}Bi, $1 \times$ ^{139}Ce) after reactor shutdown[10]. Analysis and results of the detector calibration are presented in section 4.1.

3.4.6 Vacuum Requirements

All PERKEO experiments used an evacuated beamline and spectrometer to prevent neutron scattering on air and to allow the decay products to reach the detectors. In this measurement we also wanted to detect the slow and heavy protons and had to use a detection setup on high voltage for this purpose. Hence vacuum requirements were slightly higher than in pure electron measurements.

One problem of PERKEO II is that we cannot put any pressure gauge in the neighborhood of the decay volume because of the strong magnetic field. This, however, was the region where pressure is crucial as the detection system with the foils on high voltage and the photomultipliers were installed here. Instead we measured the pressure in the beamline between orifices 2 and 3 (directly above a small turbopump, cf. figure 3.2) and at the beginning of the beam stop tube (located in between the decay volume and two big turbo pumps). Usually, the pressure measured in the beamline was slightly worse ($\approx$ 30 %) than in the beamstop.

The minimal pressure reached was $6.3 \cdot 10^{-7}$ mbar measured at the beamstop tube. We switched on the photomultipliers below $5 \cdot 10^{-5}$ mbar, and the high voltage at pressures around $8 \cdot 10^{-6}$ mbar. At these levels no problems associated with vaccum occurred.

---

[10]One reactor cycle at the ILL takes 50 days, afterwards there is a break of several days to change the fuel element. During this time, no neutrons are available.

3.5   Background and Shielding

Background is a severe problem in precision mesurements. We faced different background sources and therefore had to tackle them in different ways. A very detailed discussion of the backgrounds in a measurement like this can be found in [Kre04b].

External Background: This is generated by the environment in the experimental hall ILL 7 and consists of γ-radiation, fast, and thermal neutrons. We can fully subtract the external background, as it can be measured with closed neutron shutter, provided it is constant in time. The shutter was effectively shielded with lead so that the background produced there was not visible in the detectors [Mun06].

Beam related Background: Background generated by neutrons in our experimental setup is called "beam related". Main sources were the collimation system generating gammas and fast neutrons in the ^{6}LiF covering the orifices, scattered neutrons hitting the beam tubes that are protected by borated glass, and the ^{6}LiF-beamstop. Neutrons backscattered from the latter were catched by an installation called "aquarium", a cube made of borated aluminium (*Boral*) with an opening for the neutron beam at one side and the beamstop at the other. In short, we had beam related background produced in lithium or boron.

We made an effort to minimize this background by shielding the sources with a sandwich structure of polyethylene to moderate fast neutrons, boron to convert the neutrons to gammas, and lead to absorb the γ-radiation [Kre04, Mun06]. Furthermore, the big background-advantage of PERKEO IIB is the coincidence measurement: An event is only valid, if a second signal occurs within a given time interval after the first. All backgrounds described so far are effectively suppressed by this condition. They only act as accidental coincidences, an effect that can be well described mathematically, measured, and subtracted as described in section 4.3.3.

When the detector is operated without high voltage only electron measurements are possible and the setup is similar to an experiment to determine the electron asymmetry A. However, now no coincidence condition can be exploited to reduce the beam related background. Since we have changed the background optimized setup of the A-measurement by installing a fifth orifice closer to the decay volume, and by moving the beamstop towards the detectors, we face more beam related background that prohibits a determination of the electron asymmetry A with our setup.

Coincident Background: This background consists of events with a time structure similar to the one expected from neutron decay, i.e. a false start "electron" and a false stop "proton". Hence it is not possible to get rid of these signals using the coincidence condition, however, if it does not dependent on the presence of neutrons, it can be subtracted with a background measurement employing the neutron shutter.

Our coincident background, neglecting the purely statistical accidental coincidences, is mainly due to the high-voltage applied to the foils. We give some details on this topic in the next two sections.
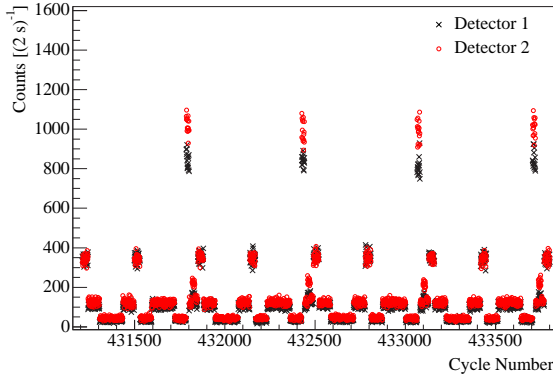
Figure 3.19: Count rate per cycle (2 seconds) for a measurement without high voltage applied onto the detector foils. The difference in the count rate of the detectors is due to different discriminator thresholds. By taking the difference between the low (*background*) and the *beam* count rate at ≈ 110 counts, we can get the individual electron count rates and with this the average neutron decay rate above the threshold: $r \approx 79$ Hz. The higher points correspond to the calibration sources.
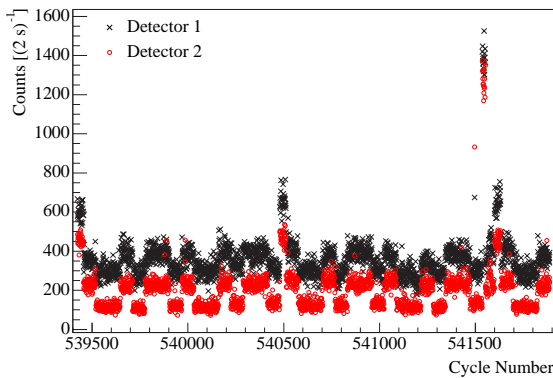

Figure 3.20: Example for a measurement ($U = -18$ kV) with stable high voltage background: Shown is the electron trigger rate per cycle (2 seconds). The different measuring modes *shutter*, *beam*, *calibration source* are clearly visible. However, detector 1 is worse than detector 2.
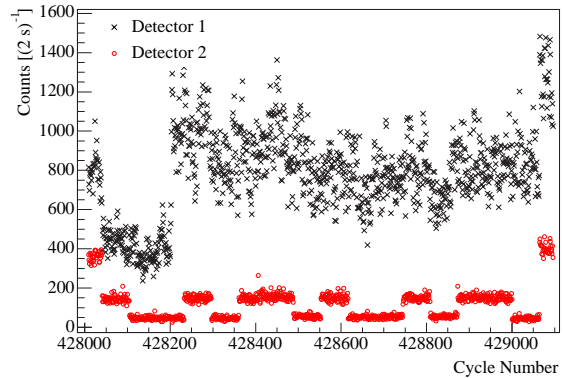

Figure 3.21: Example for a measurement with very instable high voltage background: Data was taken with $U = -15$ kV on both detector foils. Whereas detector 2 is stable over the whole measurement, detector 1 is background dominated and cannot be used for further analysis.

3.5.1 High-Voltage Background

As also seen in the test measurements on the detection system (section 3.4.2), the count rate gets larger with increasing high voltage applied to the detectors. By comparing figure 3.19, a measurement with no high voltage ($U = 0$ kV), with figure 3.20 at $U = -18$ kV, we can see that the average background count rate per cycle, corresponding to a measurement of 2 seconds, increases by 270 $(2s)^{-1}$ and 71 $(2s)^{-1}$ for detector 1 and 2 respectively. Regarding high voltage background, detector 1 is much worse than detector 2.

Figure 3.21 shows an extreme but unfortunately not rare example of a measurement with a very unstable high voltage background; the voltage applied was $U = -15$ kV: Whereas detector 2 shows a behaviour similar to figure 3.20 (the lowered rate is due to the smaller voltage), detector 1 is completely dominated by instable background and cannot be used for data analysis at all. Although we spent much time and effort to optimize the background situation on detector 1, we did not succeed and had to face a high background more than half of the measurement. Only the last three days – the vacuum vessel had been closed four days before and the high voltage had never been switched off again – detector 1 reached the

background level shown in figure 3.20. Together with its lower proton efficiency, this yields a strong imbalance in statistics of the two detectors, since detector 2 worked well during the whole beamtime.

Background in the measured Spectra: We measured energy dependent count rates $N^{\uparrow\uparrow}(E)$, $N^{\downarrow\downarrow}(E)$, $N^{\uparrow\downarrow}(E)$, and $N^{\downarrow\uparrow}(E)$, where the first arrow indicates the direction of the electron with respect to the neutron spin and the second the proton. For simplicity we omit the energy dependence in the following and focus on the B-measurement in the same hemisphere. An additional background X must be added to the count rates N^{ij}, hence we get the following expressions for difference D, sum S, and asymmetry B_{same}:

$$D \;=\; (N^{\downarrow\downarrow} + X) - (N^{\uparrow\uparrow} + X) = N^{\downarrow\downarrow} - N^{\uparrow\uparrow} \tag{3.25}$$

$$S \;=\; (N^{\downarrow\downarrow} + X) + (N^{\uparrow\uparrow} + X) = N^{\downarrow\downarrow} + N^{\uparrow\uparrow} + 2X \tag{3.26}$$

$$B_{\text{same}} \;=\; \frac{D}{S} = \frac{N^{\downarrow\downarrow} - N^{\uparrow\uparrow}}{N^{\downarrow\downarrow} + N^{\uparrow\uparrow} + 2X}. \tag{3.27}$$

These expressions assume a background that is independent of the spinflipper status, as it was the case for our measurement.

The difference spectrum D should be background-free by definition, hence it can be used to check the stability of the background level and its independence of the spinflipper status (since $N^{\uparrow\uparrow}$ and $N^{\downarrow\downarrow}$ are measured with the same detector but with the spinflipper switched on or off). An analysis of the sum spectrum S gives access to the background that is still present in the data. This decreases the asymmetry B_{same} as there is a background contribution $2X$ left in the denominator of equation (3.27). Figures 3.23 and 3.24 show the spectra D and S (corrected for all other effects) for detector 1 and 2 respectively. There is much background left for detector 1 and a bit for detector 2, but for energies above 240 keV, the spectra can be very well described by the fit functions that do not account for any background contributions. All fits have only one free parameter, a normalizing factor that does not change the spectral shape of the function. Therefore, background is no limitation for the final analysis as long as the region of interest is chosen correctly.

An important observation for the background interpretation is that most of the coincident background appears in the same hemisphere: Measurements that look for start and stop in different hemispheres have almost no background. This is shown for detector 2 detecting the first signal in figure 3.22: Although the measuring time for both background spectra is equal
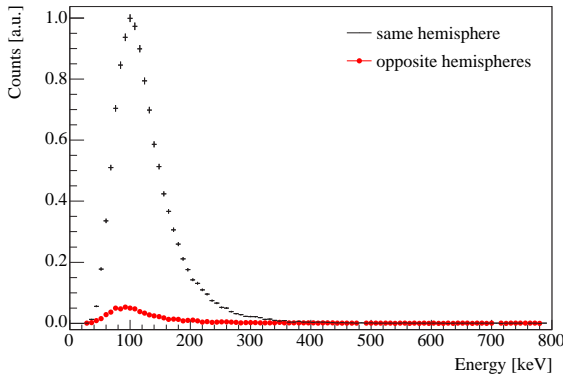

Figure 3.22: Energy distribution of coincident background, consisting of events that have a start and a stop signal, similar to the neutron decay signature. Shown is the energy of the start. The signal is more than 15 times larger when start and stop are detected in the same (here: detector 2) compared to opposite hemispheres. In the latter case, there is no background left above 250 keV, whereas the background for the same hemisphere situation goes up to 400 keV.
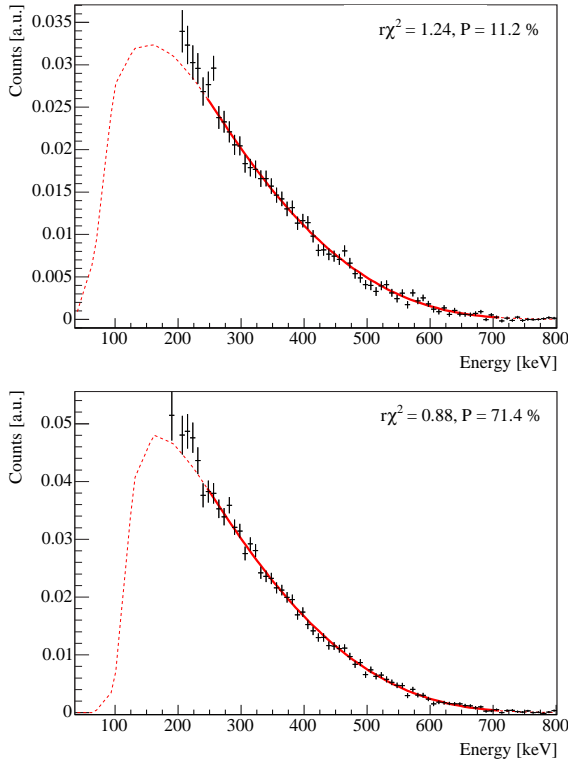
Figure 3.23: Detector 1: Difference spectrum D (top) and sum spectrum S of all data used for the analysis of the asymmetry B_{same} in the same hemisphere. There is much background left in the spectra at low energies, but the spectra can be well described above 240 keV. The solid part of the function indicates the fit region.
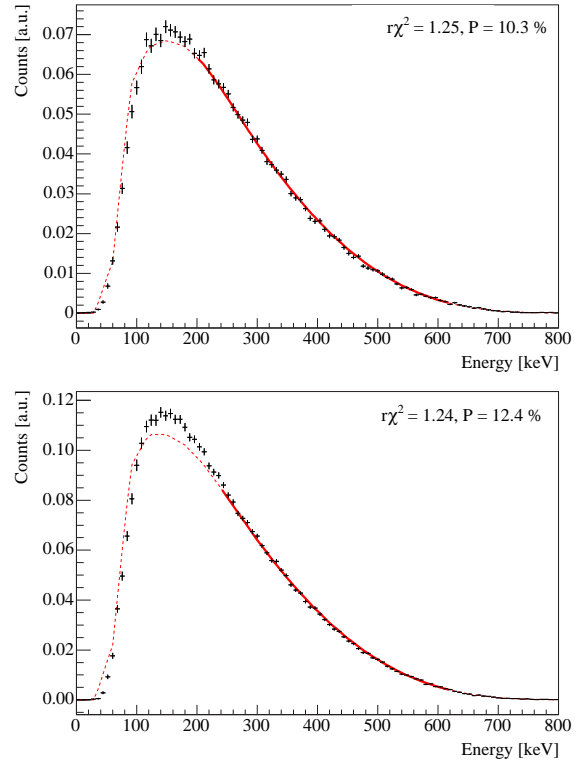
Figure 3.24: Detector 2: Difference spectrum D (top) and sum spectrum S of all data used for the analysis of B_{same}. D is almost background free in the whole energy range; N can be well described above 240 keV, i.e. there is no background left for these energies. Therefore background is no limitation for the analysis.

the signal in the same hemisphere is more than 15 times larger than the other. This effect has also been observed in the measurement of 2000 [Kre04b].

3.5.2 Simulation of High-Voltage Background

To summarize, we have to deal with a highvoltage related background generating events with coincident second triggers. Background is much higher when the second signal is detected in the same hemisphere than the first. The time-of-flight spectra of these signals, i.e. the time of the coincident stop, show the usual exponential decline superimposed by a characteristic peak. This occurs approximately 3.0 μs after the start for detector 1, detector 2 peaks a little later (figure 3.25 shows measured data for detector 1, 3.26 for detector 2).

There are several ideas to explain the nature of the coincident background [Kre04b, Dei05], e.g. one can assume that atoms of the residual gas are ionized in the high electric fields close to the thin wires shielding the decay volume creating a free electron and a much heavier ion.

We tried to reconstruct the characteristic peak structure in the TOF spectra using the Monte Carlo program *MoCaAsSiN* (Monte Carlo Asymmetry Simulation for Neutron decay) [Dei05]
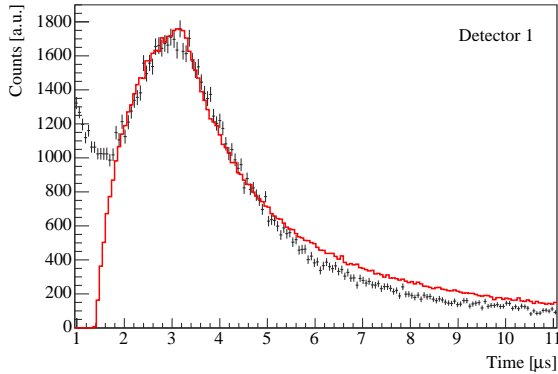
Figure 3.25: Simulation of the high voltage background: The peak in the measured background TOF-spectrum (black) can be well described by ^{4}He ions (red) generated at the last shielding grid.
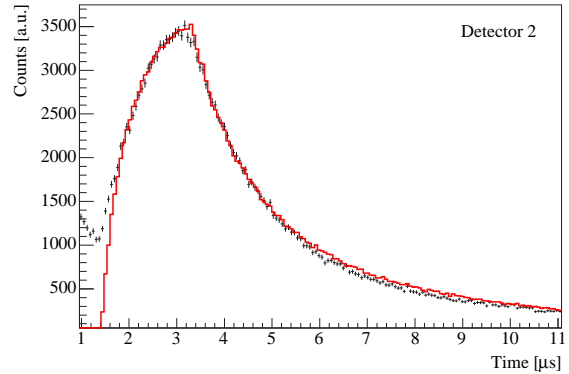
Figure 3.26: Simulation of the high voltage background: Ionized ^{14}N atoms generated at the last grid describe the structure in the TOF background spectrum even better. Both figures from [Dei05].

to simulate the above scenario. The examined ions were H$^+$, He$^+$, N$^+$, and Al$^+$: The first three are prominent constituents of the air, the last was chosen because almost all of the detector installation was made out of aluminium. We assumed a very low initial kinetic energy ($E_{\text{kin}} \approx 25\mu$eV), varied the ion generation position in the region of the grounding wires, and simulated the drift towards the foil on $U = -18$ kV.

The simulation results are shown in figures 3.25 and 3.26: Helium and nitrogen can at least qualitatively describe the measured peaks for both detectors, when the ions are generated in a region of $1-2$ mm width at the outermost grounding grid. The small difference in the peak position between the two detectors can be simply explained by a slightly asymmetric setup: Even small spatial differences (≈ 1 mm) in the ions "start"-position would yield the measured situation. Hydrogen and aluminium ions cannot describe the measured spectra.

Chapter 4

Data Analysis

Data acquisition for the PERKEO IIB measurement, presented in the last chapter, took 50 days of neutron-beamtime and approximately two more weeks for systematic checks that could be done without neutrons. To analyze this data, first of all, the detector functions, i.e. the response of the detectors with respect to different input signals, had to be obtained. Furthermore, we had to develop an approach to deal with events that exhibit more than one stop signal, and to cope with the sometimes very instable background situation. Not until this has been done successfully, we can finally generate the electron spectra and analyze the asymmetries. All these topics are described in the following sections.

4.1 Electron Detector

We introduced the mode of operation of the combined electron-proton detector in chapter 3.4.1. Now, we will present the calibration results of the electron detector, and some corrections that have to be made to account for geometrical effects.

4.1.1 Photomultiplier Calibration

One detector consists of six photomultiplier tubes (PMTs) attached to a large plastic scintillator, i.e. a measured detector signal S_{all} generated by an electron event of energy E_0 is made up of six single signals S_i:

$$S_{\mathrm{all}} = \sum_{i=1}^{6} S_i. \tag{4.1}$$

If the detector would be perfectly homogeneous, S_{all} would not depend on the impinge position (y, z) on the scintillator and the signal would always be of the same size[1]. Needless to say, that this is not the case for a detector size of 190×130 mm^2, read out in two lines with three PMTs each (cf. figure 4.1). The moderate energy resolution of the detector system is also responsible that an event of energy E_0 not always produces the same signal S_{all}.

---

[1]Please remember the coordinate system: The neutrons move in positive z-direction, x is the horizontal and y the vertical coordinate. The system is right handed.

To optimize electron detector response, we use a "PMT calibration" method developed by M. Kreuz [Kre99, Kre04b] whose notation we adopt: A calibration constant γ_i is assigned to each PMT such that the mean quadratic deviation δ from E_0 is minimized, i.e.

$$\delta = \frac{1}{N} \sum_{j=1}^{N} \left(E_0 - \sum_{i=1}^{6} \gamma_i S_i^j \right)^2 = \text{minimal}, \tag{4.2}$$

where we sum over all N events of energy E_0 measured at different positions on the detector.

The two-dimensional calibration scanner described in chapter 3.4.5, equipped with a monoenergetic electron source (^{207}Bi with two peaks), was used for the PMT calibration since it allows to place the calibration source at arbitrary (y, z) positions in front of the detector. It was installed in the decay volume center and covered only the detector area that could also be hit by electrons from neutron decay.

We solve the extremal problem (4.2) by calculating

$$\frac{\partial \delta}{\partial \gamma_k} = \frac{2}{N} \sum_{j=1}^{N} \left(\sum_{i=1}^{6} \gamma_i S_i^j - E_0 \right) S_k^j = 0, \tag{4.3}$$

an expression that can be transformed into

$$\sum_{i=1}^{6} \gamma_i \sum_{j=1}^{N} S_k^j S_i^j = E_0 \sum_{j=1}^{N} S_k^j \qquad \text{or} \qquad M\boldsymbol{\gamma} = \mathbf{s}. \tag{4.4}$$

The vectors

$$\boldsymbol{\gamma} = \begin{pmatrix} \gamma_0 \\ \vdots \\ \gamma_6 \end{pmatrix}, \quad \mathbf{s} = E_0 \begin{pmatrix} \sum_j S_0^j \\ \vdots \\ \sum_j S_6^j \end{pmatrix}, \tag{4.5}$$

and the 6×6 matrix

$$M = \begin{pmatrix} \sum_j S_0^j S_0^j & \cdots & \sum_j S_0^j S_6^j \\ \vdots & \ddots & \vdots \\ \sum_j S_6^j S_0^j & \cdots & \sum_j S_6^j S_6^j \end{pmatrix} \tag{4.6}$$

were introduced to express the problem in terms of vector equation (4.4), solved by

$$\boldsymbol{\gamma} = M^{-1}\mathbf{s}. \tag{4.7}$$

This is evaluated in an iterative way, where convergence is reached after only five iterations. We obtain the following calibration constants γ_i for the detectors:

PMT	1	2	3	4	5	6
Detector 1	1.100	0.668	0.972	1.093	0.759	1.406
Detector 2	1.368	0.777	1.118	0.893	0.717	1.127

In general, the recalibration method increases the weight of the outer tubes (1, 3, 4, 6, see figure 4.1) and decreases that of the two in the center (2, 5). However, the individual size of the constants γ varies due to the different PMT characteristics.
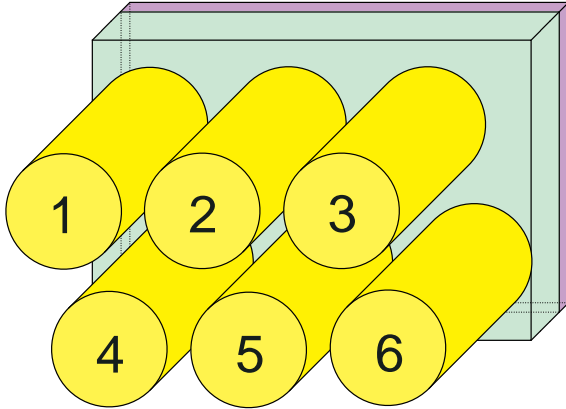
Figure 4.1: Sketch of the photomultiplier positions attached to the light guide. They are installed in two lines by three tubes each.
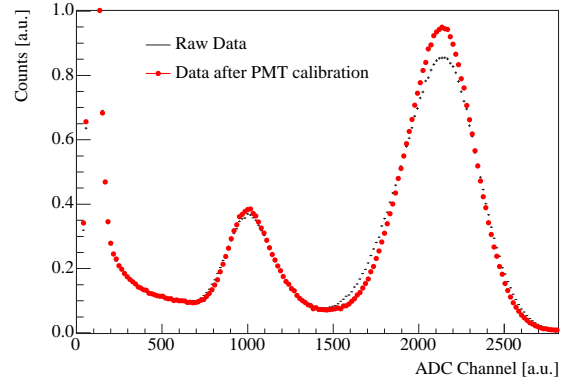
Figure 4.2: Effect of the PMT calibration procedure on the detector's energy resolution: The peak width is cleary smaller afterwards.

Besides improving the detector homogeneity, PMT calibration also enhances the energy resolution, an effect that can be seen in figure 4.2: The width of the upper Bi-peak, a measure of the energy resolution, has cleary decreased after PMT calibration. Quantitatively, we gain 18 % improvement for electron detector 1 and 15 % for detector 2. The mean deviation of the peak position for different positions of the calibration source from the average is decreased by 30 %.

To test the quality of the PMT calibration procedure, we performed it with the data of two ^{207}Bi-scans with approximately 100 (y, z)-positions each. The resulting constants γ_i agree within 8 %. Additionally, we checked the procedure by using more points or omitting some positions, however, the resulting shifts are even smaller. All these differences are much too small to yield observable effects, therefore, from now on, we will only use data calibrated with the constants γ_i given above.

4.1.2 Energy-Channel Relation

When an electron of energy E hits the scintillator, the number of photons produced is proportional to the energy. A certain fraction of the light is guided to the photomultiplier tubes and generates electrons in a photoeffect reaction in the cathode. These are multiplied and produce an analogue charge pulse that then is digitized in a charge integrating ADC. Since all parts in this sequence work linearly we also expect a linear relation between energy E of the incoming electron and the channel-sum C of all photomultipliers per detector:

$$E = g \cdot C + E_{\text{off}}. \tag{4.8}$$

The calibration carousel (introduced in chapter 3.4.5) was used to obtain *gain g* and *offset* E_{off}: It allows to place calibration sources with altogether six monoenergetic electron lines in front of the detector centers. Since we need the detector response function for the whole area covered by decay electrons, this necessitates the so-called "area correction" relating the detector function in the center to the area-average. Details on this topic can be found in section 4.1.5, the values presented here are already corrected.
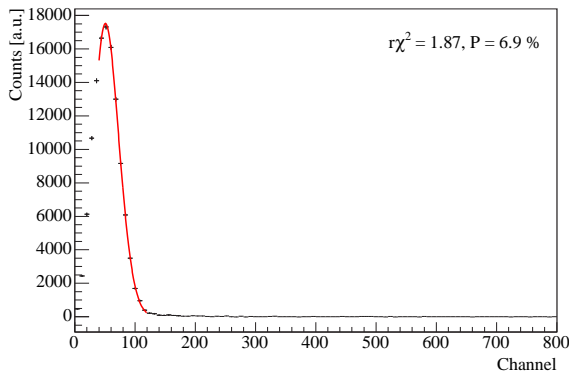
Figure 4.3: Example for a fit of the monoenergetic conversion electron source ^{109}Cd. The peak is very low energetic, 78.1 keV, and the trigger function has to be considered in the fit.
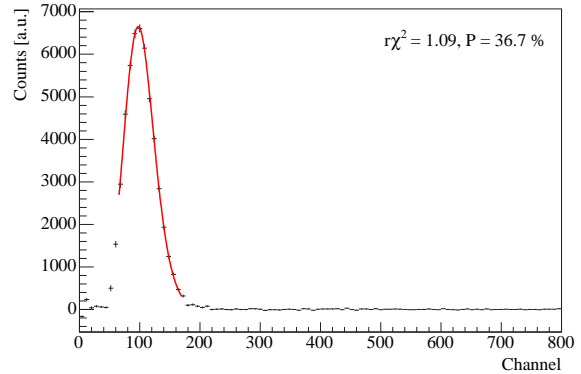

Figure 4.4: Fit of ^{139}Ce. The peak is located 136.6 keV, hence the trigger function has to be also included to account for the low energetic part of the line.
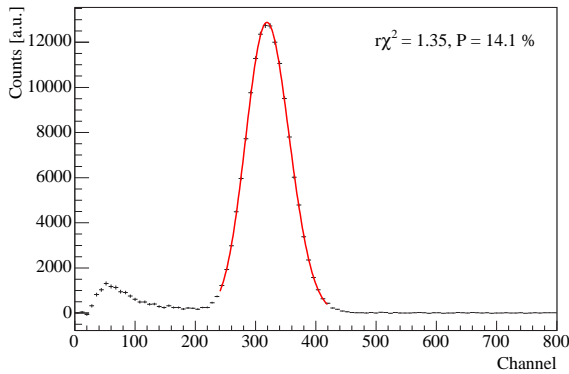

Figure 4.5: ^{113}Sn with a peak at 371.9 keV. All shown spectra were measured with detector 2.
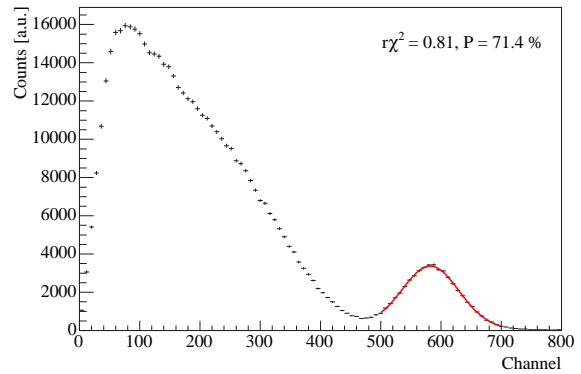

Figure 4.6: ^{137}Cs with a peak at 629.3 keV. It superimposes two continuous β-spectra.
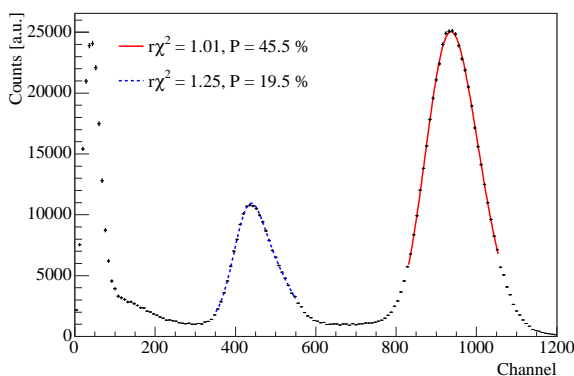

Figure 4.7: Fit example of ^{207}Bi. It shows two peak at 504.7 keV and 997.9 keV that are fitted separately. All fits to the calibration spectra are statistically significant, i.e. they have fit probabilities $P \geq 5$ %. They are used to determine energy calibration and energy resolution.
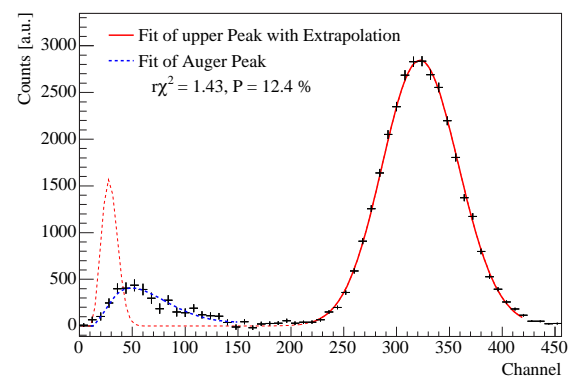

Figure 4.8: In detector 2, the Auger peak of ^{113}Sn at 25.4 keV is visible. Due to the very poor energy resolution at low energies, is is very broad, but its area agrees with the expection from a linear extrapolation of a fit to the "normal" Sn-peak. The trigger function has been considered.

Fit of the Calibration Sources: The six peaks of the conversion electron sources are fitted with a function containing the complete description of the electron lines that make up the peak [Met95]. These lines are broadened using a Gaussian to account for the detector's energy resolution and summed up to obtain the shape of the single peak at a discrete energy E. From the fit, we obtain peak position x with error and a measure of the energy resolution denoted with σ_{MeV}. All fits were statistically significant with χ^2 probabilities $P \geq 5$ %. Examples are shown in figures 4.4−4.7.

In reality, the broadening of the individual lines is governed by Poisson statistics, however, using this gives no difference to the Gaussian case that is much easier to handle. We also checked the electron's energy loss in the carbon foil to convert the protons: It is about 0.05 keV for 25 keV electrons and even smaller for higher energies. Hence it is completely negligible for the calibration.

Energy-Channel Relation: Knowing the channel positions x_i and the energies E_i of the six calibration peaks, we can perform a straight line fit to get gain and offset. However, the uncertainty acquired from the fits does not account for any systematic error, such as a slightly displaced sources or detector drifts between the measurements with the different sources. This gives rise to very poor reduced chi-squared $r\chi^2 = \chi^2/\mathrm{ndf}$ of the straight line fit, where ndf denotes the number of degrees of freedom.

Only a fit describing the data points well will yield realistic values for the uncertainty of the energy-channel relation, thus we scale the individual uncertainties in the peak position Δx_i with a factor

$$S = \sqrt{r\chi^2} \tag{4.9}$$

to obtain a straight line fit with $r\chi^2 = 1$ [PDG06]. Examples for both detectors are shown in figures 4.9 and 4.10, the scaling factors are $S = 3.3$ and $S = 12.5$ for detector 1 and 2 respectively.
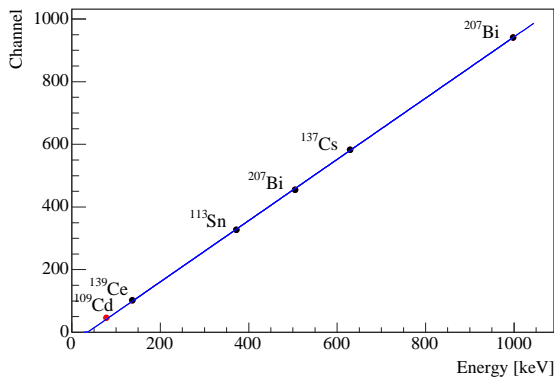

Figure 4.9: Energy-channel relation of detector 1: The used calibration points are (with increasing energy) ^{109}Cd, ^{139}Ce, ^{113}Sn, ^{207}Bi lower peak, ^{137}Cs, and ^{207}Bi higher peak.
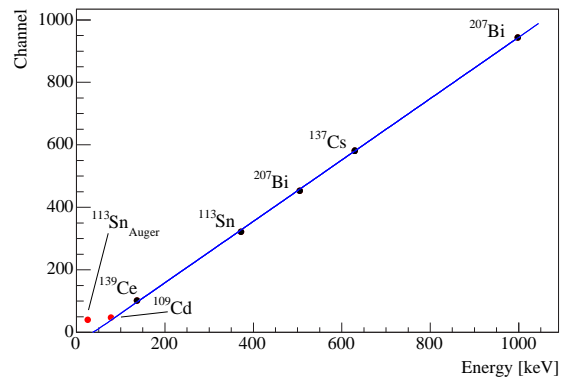
Figure 4.10: Energy-channel relation of detector 2: Obviously, the additional peak at low energy (the Auger-peak of ^{113}Sn at 25.4 keV) lies above the expected linear relation.

Non-linear behaviour at low Energies: As is well known, the peak positions at low energies are higher than expected, the energy-channel-relation flattens and is no longer linear. This behaviour starts around 100 keV: The cerium peak at 136.6 keV still fits perfectly to a linear description, whereas cadmium (78.1 keV) lies systematically too high. The peak at 25.4 keV due to Auger-electrons of tin (cf. figures 4.8 and 4.10) is even higher. Hence we omit this and cadmium in the fits to obtain gain and offset. Above 100 keV, the detectors perform well, with a non-linearity[2] L below 0.8 %.

The non-linear detector function at low energies could also be the reason that the straight line fits do not cross the origin (with the pedestal signal of $E = 0$ keV at channel 0) but show an offset ("energy loss") of $35-40$ keV. If the detector would respond perfectly linearly all electrons with lower energies would be lost. Obviously, this is not the case: We can identify the peak at 25.4 keV, and we also detect secondary electrons generated by protons hitting the carbon foil: They have energies of $12-18$ keV. However, the energy resolution of the detector gets very poor at low energies. An ansatz to describe the effect could be that the trigger function cuts away the lowest part of an extremly broadened electron peak, leading to a higher peak barycenter.

We account for backscattered events by summing up the energy content of both detectors. If one of the signals is very low, the non-linearity leads thus to a wrong detector sum. However, this effect is not crucial, since the backscattered events are considered in the calibration, and therefore only yield a slightly decreased energy resolution.

Results: Calibration measurements were performed regularly during the expriment. Therefore each "measurement", a period of 20 min to 15 hours data acquisition, can be calibrated on its own to account for drifts. However, to study the general influence of calibration, we are also interested in the average values for both detectors:

	Gain g	$\Delta g/g$	Offset E_{off}	$\Delta E_{\text{off}}/E_{\text{off}}$
Detector 1	1.0415	0.3 %	37.7 keV	5.8 %
Detector 2	1.0370	0.6 %	40.4 keV	10.7 %

We obtain the mean uncertainty of gain g and offset E_{off} by averaging the errors of the individual calibration measurements. They are used to determine the effect of the imperfect energy calibration on the asymmetries.

The table shows that the gain is known much more precisely than the offset, and that calibration of detector 1 is superior. The reason for this is not known, however, it is not important for the determination of the neutrino asymmetry in the same hemisphere, since the asymmetry is almost flat. For the opposite hemispheres and the proton asymmetry, detector calibration yields large uncertainties.

---

[2]The non-linearity L is defined via

$$L = \left| \frac{\Delta C}{C_{\text{max}}} \right|,$$

where C_{max} is the maximal measured channel and ΔC is the maximum deviation from the linear fit [Leo94].

4.1.3 Energy Resolution

The energy resolution σ_E is governed by the number of photo-electrons N generated in the photomultiplier tubes. This process obeys Poisson statistics, thus $\Delta N = \sqrt{N}$, and since N is proportional to the energy E of the electron we obtain

$$\frac{\sigma_E}{E} = \frac{\sqrt{N}}{N} = \frac{1}{\sqrt{N}} \tag{4.10}$$

or

$$\sigma_E = \sigma_{E_0} \sqrt{\frac{E}{E_0}}, \tag{4.11}$$

where E_0 is a reference energy: The energy resolution is proportional to the square-root of the energy.

We use $E_0 = 1$ MeV and rewrite equation (4.11) introducing σ_{MeV}, the energy resolution at 1 MeV:

$$\sigma_E = \sigma_{\mathrm{MeV}} \sqrt{\frac{E[\mathrm{MeV}]}{1\ \mathrm{MeV}}}. \tag{4.12}$$

This expression is used as standard deviation of a Gauss-curve to broaden the lines in the calibration fits[3], where σ_{MeV} is a free parameter to be determined. The averaged values and uncertainties are:

	σ_{MeV}	$\Delta\sigma_{\mathrm{MeV}}/\sigma_{\mathrm{MeV}}$	PE/MeV
Detector 1	64.2 keV	1.0 %	243(5)
Detector 2	62.9 keV	0.7 %	253(4)

In the last column, we have used σ_{MeV} and equation (4.10) to calculate the number of photo-electrons (PE) per MeV. If we define the energy resolution δ_E via

$$\delta_E = \frac{\Delta E}{E} = \frac{\mathrm{FWHM}}{E} = \frac{2.35\ \sigma}{E} \tag{4.13}$$

[Leo94], we obtain $\delta_E = 15.1$ % and $\delta_E = 14.8$ % at 1 MeV for detector 1 and 2 respectively.

4.1.4 Detector Drifts

Detector calibration was done regularly during the asymmetry measurements, thus we are able to identify drifts of the data acquisition system. Figure 4.11 shows the position of the upper Bi-peak in all calibration measurements during three weeks of data taking: At the beginning, the peak positions – which is a measure of the gain drift – show a large spread. But the installation of an additional external cooling device[4] for data acquisition electronics (vertical line) stabilized the drift on small time scales immediately.

---

[3]All fits describing measured data use σ_{MeV} to broaden the electron spectrum to account for energy resolution.

[4]The experiment was performed from June to August 2004, with temperatures of up to $30°$ C in the experimental hall ILL7.
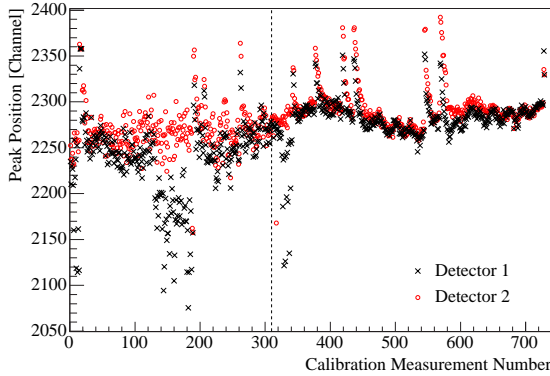
Figure 4.11: Evolution of the upper Bi-peak position in time: Shown are all calibration measurements that have been performed; the x-scale ranges over more than three weeks, but the scale is not linear during the first measurements. The vertical line represents the installation of an additional external cooling system for data aquisition electronics, and the sharp peaks indicate when the vacuum system was closed right before. No measurements were performed directly after vacuum closing. The wiggles on the right are due to a day-night gain drift of about 0.5 %.

The high peaks in the figure occur when the vacuum system was closed right before the measurements. They show an increase of $4-5$ %, and drop off to the usual level in about five hours. This is irrelevant for the asymmetry measurements since these need high voltage on the detector foils which was applied not earlier than several hours after closing the vacuum vessel.

The remaining drift at the percent level over several days is negligible since calibration measurements were performed every $20-30$ minutes. On this time scale the drift is irrelevant. This also holds for the small day-night effect of 0.5 % causing the wiggles superimposed on the overall drift in the right part of figure 4.11: The maximum arises at about 12:00 hours and the minimum around midnight.

Although the detector drift was quite high before installation of the cooling device, data is not lost completely. Analysis shows that it can be used to obtain the asymmetry B_{same} in the same hemisphere, which is almost independent of detector calibration (cf. chapter 4.6).

4.1.5 Detector Homogeneity and Area Correction

In this chapter, we want to give details on the "area correction", that was shortly mentioned in section 4.1.2. It accounts for the fact that the energy calibration measurements were performed in front of the detector center, whereas the gain can be different at other positions.

Detector Homogeneity: If the detector would be perfectly homogenious, i.e. its gain would be constant over the whole area (corresponding to an unchanged peak position), the area correction would be unity. However, this is not the case, what can be analyzed using calibration data obtained with the two-dimensional scanner (figure 4.12).

If we define the inhomogeneity Δm to be the quadratic deviation of a peak p_i obtained at a scanner position i from the detector average $\overline{p}$,

$$\Delta m = \sqrt{\frac{\sum w_i (p_i - \overline{p})^2}{\sum w_i}}, \tag{4.14}$$

where the weights w_i are determined by the neutron density at the vertical y_i-position (cf. figure 3.13, page 41), we obtain $\Delta m(\mathrm{Det}\ 1) = 3.7$ % and $\Delta m(\mathrm{Det}\ 2) = 4.6$ %. Weighting
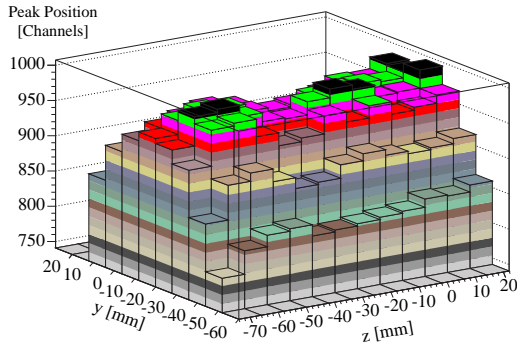
Figure 4.12: Peak position of the higher Bi-peak measured with detector 1. The source was placed at different positions (y, z) in front of the detectors. The corresponding plot for detector 2 is comparable.
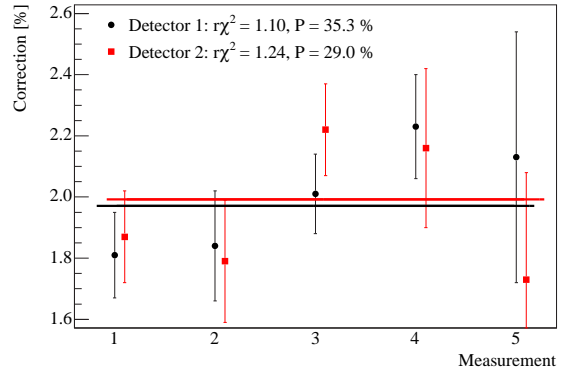
Figure 4.13: Area correction to be applied to the gain of the energy-channel relations: The values are obtained from five individual peaks (1: $Bi_{low,Scan1}$, 2: $Bi_{high,Scan1}$, 3: $Bi_{low,Scan2}$, 4: $Bi_{high,Scan2}$, 5: Ce) and show nice agreement.

with the neutron beam is important since we have to know the detector performance for a measurement of charged products from neutron decay.

Area correction: Now, we compare the peak position p_c of a calibration source placed in front of the detector center with the average over the whole detector area p_{mean} which is again weighted with the vertical neutron density. The quantity

$$f_{area} = \frac{p_c - p_{mean}}{p_c} \tag{4.15}$$

is the relative area correction factor: The gain g obtained from a calibration fit has to be divided by $(1 - f_{area})$, the offset E_{off} stays unchanged.

Altogether three detector scans have been performed: Two using a ^{207}Bi-source with two peaks and one with ^{139}Ce. Thus we can altogether use five peaks to obtain f_{area} that should not depend on the scan and the used calibration source. The decay volume was scanned at 96 positions, however, some measurements had to be omitted because of a too large positioning uncertainty. We reconstructed the missing positions with linear extrapolation from the neighboring points.

The results are presented in figure 4.13: The factors determined from different peaks/scans agree very well, therefore we can calculate the average and yield $f_{area} = 1.97(8)$ % and $f_{area} = 1.99(10)$ % for detector 1 and 2 respectively. It is not surprising that two factors coincide, since the detectors are constructed exactly the same way using the same materials.

4.1.6   Trigger Function

The trigger function $T(E)$ gives the probability that an electron of energy E generates a trigger in the data acquisition system. Here, we face the problem that the energy-channel relation is not linear at low energies where the trigger probability is smaller than unity. Therefore a conversion of channels C into energy E is not possible here.
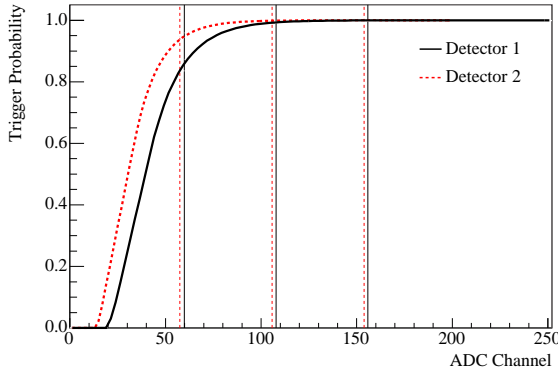
Figure 4.14: Trigger functions for both detectors: Due to the non-linear behaviour of the energy-channel relations at low energies, a conversion of ADC-channels to energy is not possible below 100 keV. However, to get an impression of the trigger probability, we plotted vertical lines at 100 keV and 150 keV for both detectors: It is certainly unity above 200 keV (third line).

Anyhow, we can gain some information from the trigger function: It can be obtained by analyzing backscattering events, i.e. events that depose energy in both detectors, and is defined (here for detector 1) by

$$T_{\mathrm{Det1}}(C) = \frac{h_1(C)}{h_1(C) + h_2(C)},\tag{4.16}$$

where $h_1(C)$ and $h_2(C)$ are energy-histograms of detector 1: h_1 contains all events where both detectors have triggered (i.e. at least two out of six PMT signals per detector have passed the disciminator threshold), and h_2 contains all events where detector 2 has triggered and detector 1 not. Figure 4.14 shows the resulting histogram $T(C)$ for both detectors. The trigger probabilities are given here:

	90 %	100 %
Detector 1	104 keV	170 keV
Detector 2	94 keV	160 keV

Above 200 keV, the trigger function is certainly unity, but it has to be taken into account at lower energies, e.g. for the fits of the cadmium and cerium calibration peaks; it cancels in the asymmetry spectra.

Due to the instable low energetic background in detector 1 we did not decrease the discriminator threshold as low as possible, resulting in a slightly worse trigger function. This is the reason that the Auger-peak of tin (cf. fig. 4.10) is only visible in detector 2. Both trigger functions are independent of the high voltage applied, and – within the poor statistics of the scanner measurements – independent of the impinging point on the detector.

4.1.7 Electron Backscattering and Time Resolution

Compared to solid state detectors[5], plastic scintillators have the lowest backscattering (BS) probabilities in electron spectroscopy due to their low average atomic number Z. But with $p_{\mathrm{BS}} \approx 8\%$ [Leo94] this probability is still quite high ($p_{\mathrm{BS}} \approx 4\%$ for normal incident). In our setup, the magnetic field of PERKEO II lowers this value considerably due to the magnetic mirror effect (cf. section 3.3.3), where an electron moving in an increasing magnetic field can

---

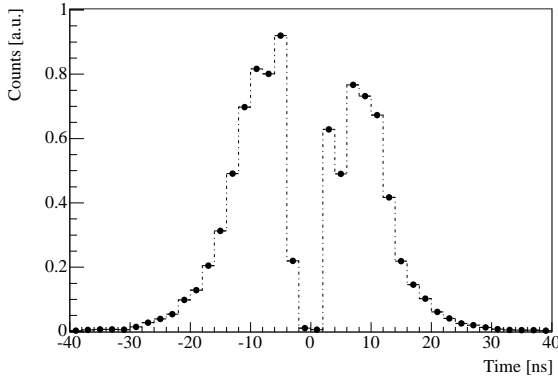[5]NaI-Scintillators have backscattering probabilities up to 80 % [Leo94].

Figure 4.15: Timing measurement of 2-trigger backscattering. The plot shows the TDC difference between detectors 1 and 2, hence events where detector 1 triggered first are in the left peak. The peaks are well separated.
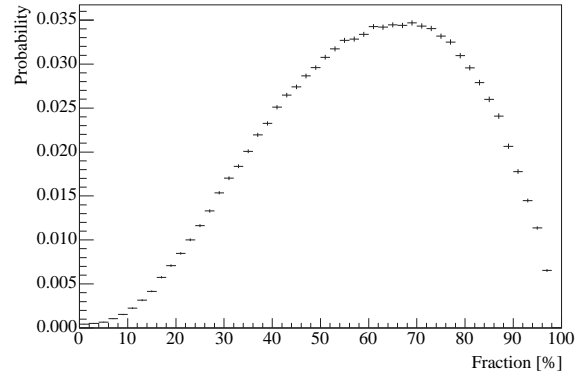
Figure 4.16: Measurement of the probability that a backscattering event deposits a particular fraction of its energy in the primary detector. It shows a strong preference to depose more energy in the primary detector.

be reflected. This happens to many electrons scattered out of the detector, and returns them to the scintillator where they depose their remaining energy.

We study backscattering in an integral way and do not distinguish between different angles of incidence θ on the detector. The maximal angle θ_{max} is around 45° (measured to the detector normal) as the decreasing magnetic field transfers the electron momentum into the component parallel to the field lines. Most electrons hit the detector at these angles (cf. also figure 4.56 on page 99). The influence of the magnetic field reduces the overall backscattering probability to below 5 %.

2-Trigger Backscattering: Whenever a trigger signal occurs, the ADCs of both detectors are read out simultaneously. With 180 ns, the integration is time much higher than the average time the backscattered electrons need to cover the distance beween the detectors (800 mm), and we always obtain the full energy information of the event. 2-trigger backscattering occurs when an event generates a trigger in the primary and the second detector. This allows to determine the chronological order of the two triggers by using the timing information of the TDC. If its resolution is smaller than the minimal flight time between the detectors, this assignment can be done without any uncertainty.

Figure 4.15 shows the timing measurements of 2-trigger backscattering: The well separated peaks correspond to events where detector 1 (left) or detector 2 (right) was hit first, the separation is a measure of the system's time resolution: It is given by the TDC-channel width of 0.8 ns. In between the peaks, where no first detector can be assigned properly, there are less than 0.2 % of the events. Combined with the backscatter probability of below 5 %, this fraction – omitted in the analysis – is negligible. The energy of the backscattered electrons is not distributed uniformly into primary and secondary detector (figure 4.16): Independent of the overall signal size, it shows a strong preference to depose more energy in the first.

Unrecognized Backscattering: To analyze the effects of unrecognized backscattering, i.e. backscattering where we do not have two triggers and therefore cannot proceed as de-
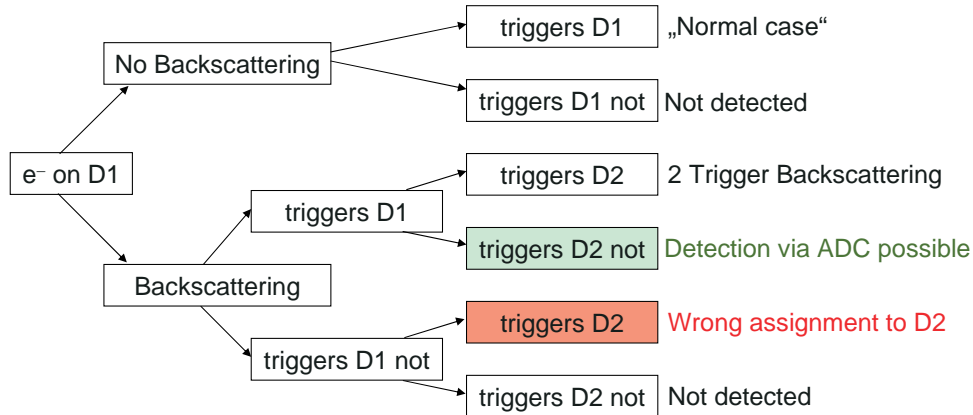
Figure 4.17: Backscattering decision tree: The 4th and the 5th case from top are important for unrecognized backscattering, but only the 5th case influences the asymmetry measurements.

scribed above, we have to take a look at the decision tree shown in figure 4.17, considering an electron hitting detector 1: If no backscattering occurs it is not important whether detector 1 triggers or not. In the first case, we have the usual electron detection and in the second nothing happens at all – but this case is limited to very small energies and is described by the trigger function.

Now consider the case with backscattering. When detector 1 and detector 2 record a trigger we have 2-trigger backscattering as described above. For small energies it is possible that both detectors do not trigger and the event gets lost. When detector 1 triggers and detector 2 does not, we have unrecognized backscattering, but the event is assigned to the correct detector. Crucial is only the case where the primary detector does not trigger but the secondary does. Here the event is assigned to the wrong detector – imposing a systematic error to the asymmetry measurement that depends on the correct determination of the initial momentum direction.

As the energy information is always available for both detectors, we can analyze the ADC content of the second: If the primary detector has triggered and the ADC of the secondary contains a signal above the pedestal threshold[6], we have identified an unrecognized backscatter event. This is shown in figure 4.18: Histogram H_1 shows the energy content of detector 2, when detector 1 has created the primary and detector 2 the secondary trigger. H_2 includes events where detector 1 has triggered first and the ADC content of the second is above the pedestal threshold. For energies high enough to generate a second trigger, the curves coincide. For low energies, the second spectrum shows additional unrecognized backscattering, where detector 2 has not triggered.

It is important to notice that the experimental signature of

$$\text{Detector 1 (trigger)} \quad \rightarrow \quad \text{Detector 2 (no trigger)}$$
$$\text{Detector 2 (no trigger)} \quad \rightarrow \quad \text{Detector 1 (trigger)}$$

is the same (the arrow indicates the chronological order) whereas the signals belong to different "primary" detectors. Hence we have to discriminate between these cases (cf. also figure 4.17).

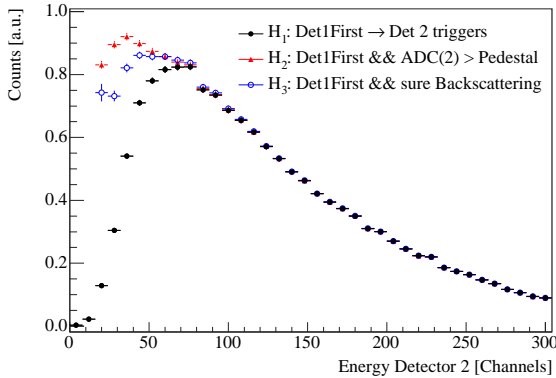[6]The ADC signal without any energy deposition, corresponding to 0 keV.

Figure 4.18: Low energy part of the energy spectrum of the second detector under the condition that detector 1 has triggered first (Det1First). H_1 includes all events with two triggers. The difference between H_2 and H_3 are the events wrongly assigned to detector 1. (cf. text).
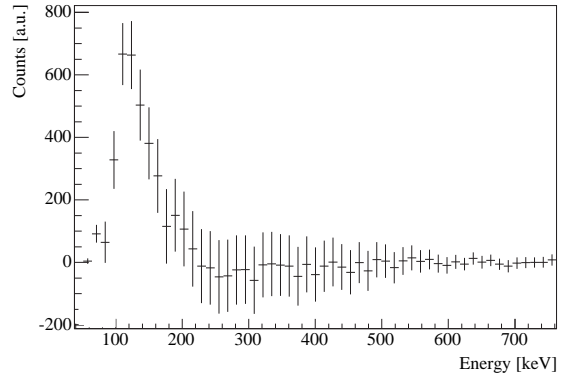
Figure 4.19: Total energy of the wrongly assigned events that are detected as "detector 1 first" but really detector 2 was hit before without generating a trigger. The plot shows that unrecognized backscattering is a low energy effect. Note that the energy scale is invalid below 100 keV.

We recall, that the trigger function gives the probability $T_d(E)$ that an electron of energy E generates a trigger signal in detector d. If this probability would be unity for the whole energy range, we would not have any unrecognized backscattering. Thus we correct the 2-trigger spectrum H_1 in figure 4.18 to obtain a trigger probability

$$T_2(E) = 1 \quad \text{for all } E \tag{4.17}$$

by dividing it by the trigger function of detector 2. The resulting spectrum H_3 contains all events where detector 1 has triggered first and the backscattered electron has reached detector 2.

The difference between the spectra H_2 and H_3 is the fraction of wrongly assigned events. Here, the experimental signature suggests that the events belong to detector 1, wheras in reality the electron hit detector 2 first – without depositing enough energy to create a trigger.[7]

Fraction and Spectrum of wrongly assigned Events: In this paragraph, we will show that the influence of wrongly assigned events is negligible in our measurement. In order to analyze unrecognized backscattering quantitatively, it is necessary to extrapolate to lower ADC channels, as it is not possible to evaluate the spectra below a certain channel due to the pedestal threshold[8]. We have chosen two extreme extrapolation cases for the histograms H_2 and H_3 in figure 4.18: In the first, we assume that no entries are in the lowest bins, in the second we set them to the value of the last correctly determined channel.

---

[7]It is also possible to obtain the number of wrongly assigned events by looking at the energy spectrum of detector 1, where detector 1 triggered first and detector 2 generated a second trigger [Bae96]. This spectrum can be divided by the trigger function of detector 1. The difference of the spectra gives again the number of events assigned to the wrong detector. However it is not possible to determine all branches in the decision tree (fig. 4.17) with this method.

[8]Below a certain energy, the pedestal prevents a correct identification of backscattering events, and the histogram H_2 diverges.

	2-trigger	"true" backscattering	wrong assignment
Detector 1 First	4.23(1) %	4.9(2) %	0.12(1) %
Detector 2 First	3.57(1) %	4.4(2) %	0.20(2) %

Table 4.1: Results of the general amount of backscattering and of the fraction assigned to the wrong detector. Since detector 1 had a slightly worse trigger function and an higher pedestal threshold, its number of wrong assigned events is higher.

We average over both extrapolation cases to obtain a value for the wrongly assigned backscattering, and choose the difference between average and extrapolation to be the $2\,\sigma$ error. This is a reasonable decision to account for the statistical errors, the extrapolation, and the non-linearity of the detector in this energy region. Table 4.1 shows the results: Integration of H_1 yields the 2-trigger backscattering, the integral of H_3 (extrapolated as described above) gives the number of "true" backscattering events, where the correct detector has triggered first, and the difference $H_2 - H_3$ gives the fraction of wrongly assiged events. These are less than 5 % of all backscattering events.

For the analysis of a low-energy experiment it is important to know the energy of the events assigned to the wrong detector to check their influence. Figure 4.19 shows their spectrum: Within the errors, there are no events above 240 keV, whereas, in general this result depends on the trigger thresholds of the detectors.

The energy spectrum can also be modeled: We start with the normalized distribution $P_{E_*}(E)$ (figure 4.16) giving the probability that a backscattered electron of total energy E_* deposes a certain energy E in the primary detector. A low energy threshold (a step-function at x_0 = 39, 47, and 55 keV) is introduced to account for the trigger function of the first detector. The distribution is integrated for different electron energies E_* from 0 to x_0 to determine the fraction of events not triggering the first detector. This is then multiplied with the phase space factor $F'(E_*)$ of the Fermi-spectrum (cf. equation (2.30)) to obtain an energy distribution
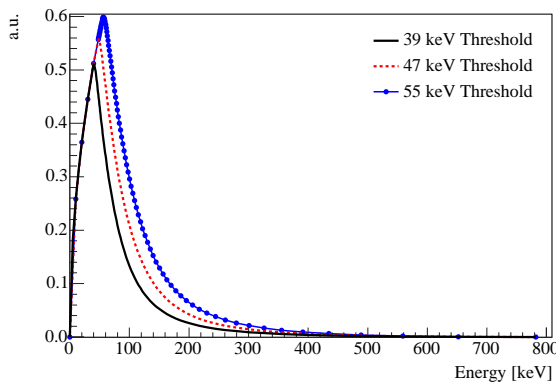

Figure 4.20: Modeled energy spectrum of the events wrongly assigned to the first detector for different trigger thresholds. The shape is similar to the experimental data, figure 4.19.
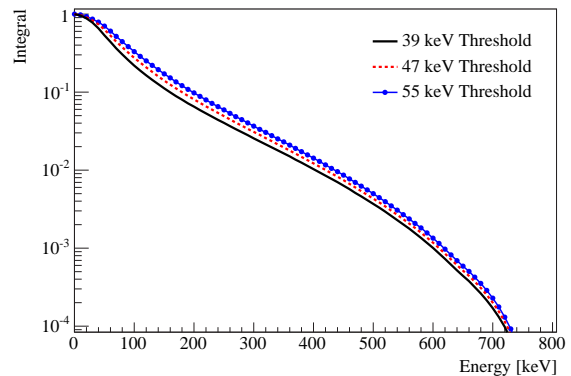
Figure 4.21: Integral of the three modeled spectra of figure 4.20: Above 200 keV, the fraction of wrongly assigned backscatter events is below 10 %.

similar to the experimental situation. The model yields the spectrum $s(E_*)$:

$$s(E_*) = F'(E_*) \int_0^{x_0} P_{E_*}(E) \, \mathrm{d}E. \qquad (4.18)$$

The trigger function of the secondary detector is neglected.

The model, figure 4.20, agrees well with the measurement, figure 4.19, and integration allows to estimate the fraction of wrongly assigned events in the spectra: If the region of interest starts above 240 keV, the model predicts less than 6 % ($x_0 = 55$ keV) of wrongly assigned events to have higher energies. With overall 0.2 % wrongly assigned events (table 4.1), this yields a maximal correction in the order of 0.01 % which is completely negligible. This result is consistent with the measurement shown in figure 4.19 with no wrongly assigned events above 240 keV within the errors[9]. However, when the low energetic part of the spectrum shall be used as well, the effect of wrongly assigned events may be critically.

4.1.8 Summary

Here, we give a brief summary on the properties of the electron detector:

- Above 100 keV, the electron detector shows a linear energy-channel relation with a non-linearity well below 1 %. At smaller energies, the linear relation is no longer valid.

- Whereas the gain g of the energy-channel relation is known with a rather small uncertainty, the offset E_{off} can only be determined with an relative error of ≈ 10 %.

- The energy resolution (FWHM) at 1 MeV is about 15 %. Detector homogeneity and energy resolution were optimized in a PMT calibration procedure.

- Detector drifts on the percent level are irrelevant since calibration measurements were performed on a much smaller time scale.

- Since the calibration sources were positioned in front of the detector center, an area correction of $\approx 2\%$ accounting for the full detector area has to be performed.

- Electron backscattering is reduced by PERKEO's strong magnetic field and detected with a fast TDC. Unrecognized backscattering can be deduced from measured data: Its influence is negligible above a threshold of 240 keV.

4.2 Proton Detector

The proton spectra are also measured with the electron detector, however, when we say "proton detector", we consider the signals of the secondary electrons generated in the carbon foil, detected in the proton part of the data acquisition system. That means that one "start" signal (due to an electron) must have been occurred in advance.

---

[9]For our experiment, we even expect a fraction lower than 6 %, since the low energy electron spectrum is greater than the Fermi spectrum used in the model due to additional background. This yields an increase of events assigned to the wrong detector below 200 keV, whereas the overall size of the effect, determined as described above, is not changed.
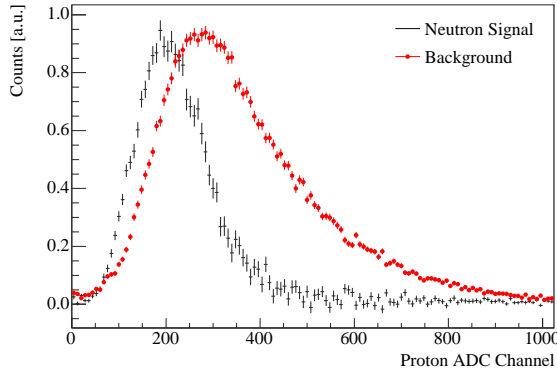
Figure 4.22: Energy-spectrum of the first stop ("proton") of detector 2: Neutron decay related signal and background look very similar and are low energetic. In this range a conversion to energy is not reasonable due to the non-linear detector behaviour below 100 keV. This corresponds to channel 250, 250 keV to channel 940.
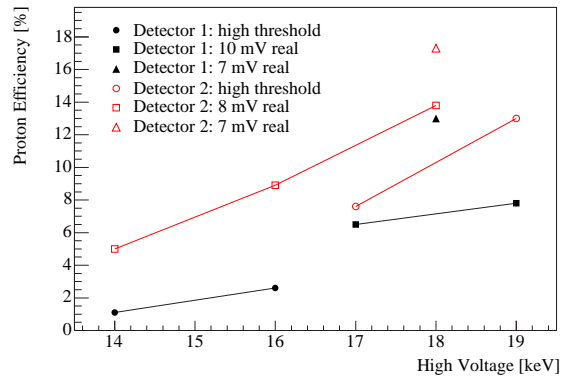
Figure 4.23: Proton efficiencies for both detectors, given for different high voltages applied to the foil and various discriminator thresholds. Equal threshold settings are connected with lines. Detector 2 always shows a higher efficiency. The best values were obtained at 18 keV with thresholds of 7 mV.

Calibration: The energy-channel relation of the secondary electron (proton) detector is also determined with the six electron sources. However, since two events with a time difference smaller than 80 μs are needed for the first stop, three within this window for the second etc., calibration statistics decreases rapidly from stop 1 to 4, and only a crude calibration can be obtained for the proton energy spectra. Furthermore, the largest part of the spectra lies below 100 keV where the relation is no longer linear. Therefore no precise energy information is available for the secondary electron spectra, they can be only analyzed qualitatively.

Secondary Electron Spectrum of first Proton-Stop: Figure 4.22 shows the secondary electron energy spectrum of the first proton of detector 2 (detector 1 looks similar with the peak slightly shifted to lower energies): The neutron related spectrum is not well separated from the background that even extends to higher energies. Thus, we cannot use the energy spectrum for discrimination between neutron related and background events, but can only compare the overall spectral shape.

The similarity of the spectra also gives a hint on the background nature: The signal is most likely also generated in the carbon foil on high voltage, but the average secondary electron yield is somewhat higher than for protons. This is what we would expect for ions produced at the grounding grids and accelerated onto the foil, since they are heavier than protons.

Proton Efficiency: The fraction of protons detected per neutron decay is refered to as proton efficiency. It increases with larger foil-voltage and with decreasing discriminator threshold. During data acquisition, we varied both to improve background conditions, and to increase the proton efficiency. The overall neutron decay rate r (with electron energies above the discriminator threshold) can be derived from a measurement without high voltage, e.g. figure 3.19 (page 51): It is $r = 79$ Hz. The proton efficiencies for different detectors, high voltages, and discriminator thresholds, normalized to this decay rate are given in figure 4.23:

We were able to identify the first proton signals at -12 kV, and achieved a maximal proton efficiency of 17.3 % for the last five measurements with detector 2, where the threshold was as low as possible. Compared to detector 2, the efficiency of detector 1 was always lower with a maximum of 13.0 %.

4.3 Coincidence Measurement

As we cannot detect the neutrino itself, we have to reconstruct it from a coincident measurement of electron and proton. Due to the rather low count rates, in principle, we would expect a clean event signature with an electron as "start" and a proton ("stop") following some microseconds later. However, high voltage background and accidental coincidences alter the measurement and have to be accounted for.

Time-of-Flight Spectra: In order to analyze the coincidence measurement we study the time-of-flight (TOF) of the stop, i.e. the time difference between the starting electron and the proton (or background). The TOF spectra for the case where electron and proton are detected in the same hemisphere are given in figure 4.24, for the opposite hemisphere in figure 4.25. The protons need a certain time to drift from the decay vertex towards the detectors, before they are accelerated by the high voltage. This drift time is slightly higher for events in the same hemisphere due to the initial momentum distribution of the protons.

We use the time-of-flight spectrum to discriminate between events. For example, if a stop would occur at 0.4 μs, this is too fast for a proton, and the event is due to background. When several stops arise, the TOF information is also used to decide how to proceed. This will be described in the following sections.
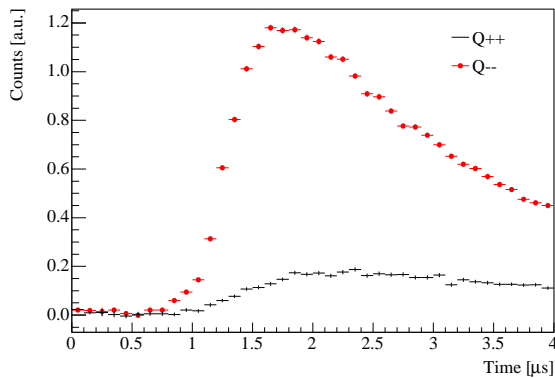

Figure 4.24: Time-of-flight measurement of the spectra Q^{++} and Q^{--}, where electron and proton are detected in the same hemisphere. The minimal drift time is ≈ 0.8 μs. Background is subtracted.
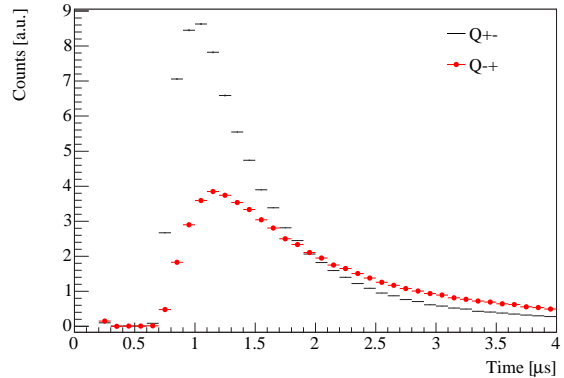
Figure 4.25: Time-of-flight measurement of the Q-spectra in opposite hemispheres. The spectra start a little earlier at about 0.65 μs. Both figures are scaled equally.
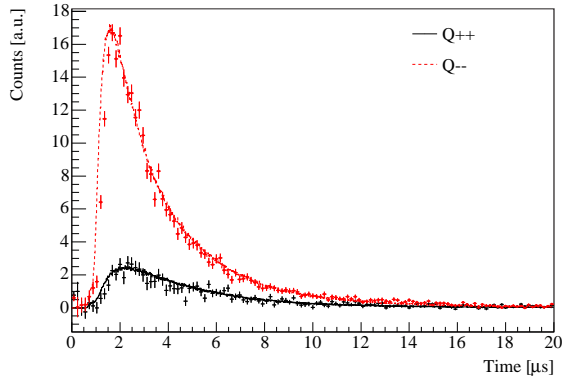
Figure 4.26: Monte Carlo simulation of the time-of-flight spectra for the B measurement in the same hemisphere. The histograms show measured data, the solid lines the simulations.
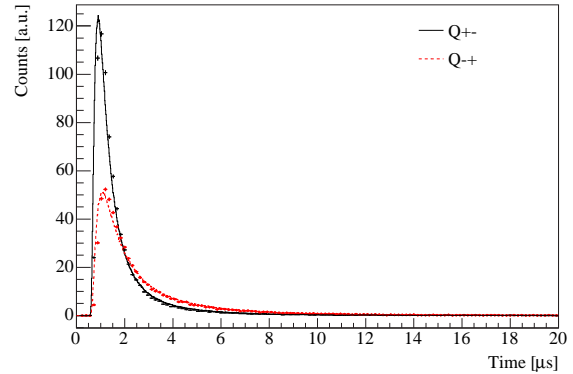
Figure 4.27: TOF-Simulation of the spectra in opposite hemispheres. The spectra are normalized equally to figure 4.26, the count rate difference is a real property of neutron decay.

4.3.1   Monte Carlo Simulations

In chapter 3.5.2 we have already introduced the Monte Carlo simulation program *MoCAsSiN* [Dei05] that has been developed to simulate neutron decay in the experimental setup of PERKEO II. It accounts for the real neutron beam shape and the realized detector geometry, and allows to obtain the following spectra:

- All relevant electron (and proton) energy spectra such as Q^{ij}, difference D, sum S, and the asymmetry itself. From these, simulated including systematic effects, the correction spectra can be obtained (cf. chapter 4.5).

- Time-of-flight spectra of protons.

- Time-of-flight spectra of ions for background studies.

Simulation of proton time-of-flight is performed in a phenomenological way instead of solving the exact equation of motion in a combined electric and magnetic field. This means, that the proton motion consisting of an initial drift, followed by acceleration in an increasing electric field (due to the grounding grids) and in the full high voltage potential at last, is separated in only two parts: A drift region where the motion is governed by the proton momentum p and the magnetic field turning p in forward direction. In the second region, the simulated proton is accelerated by the full electric field. The borderline between the two is adjusted using real data from the measurement; the simulation results describe the stop spectra of the functions Q^{++}, Q^{--} (figure 4.26) and Q^{+-}, Q^{-+} (figure 4.27) quite well.

We used the simulation for a quantitative analysis: Figure 4.28 shows the fraction of protons arising in a certain time interval after the electron, the last bin includes a linear extrapolation to larger times. Integration of this spectrum from a lower border t_0 to 40 μs yields the proton fraction that is still missing at time t_0. This is shown in figure 4.29: The fraction of "missed" protons is smaller than 0.02 % for all four Q-spectra. However, the following small corrections Δ_t have to be applied to the asymmetries as a consequence of the finite coincidence window length of 40 μs:
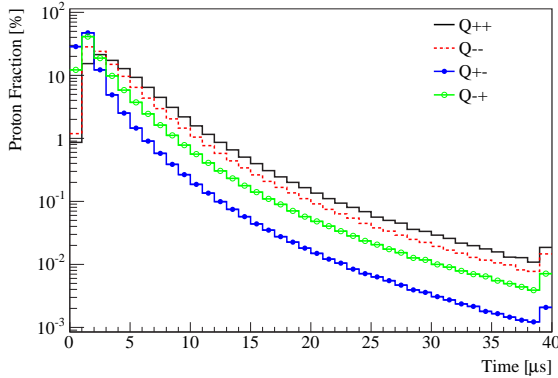
Figure 4.28: Simulation of the fraction of protons in the TOF-spectrum for different time intervals. The last bin is a linear extrapolation to larger times.
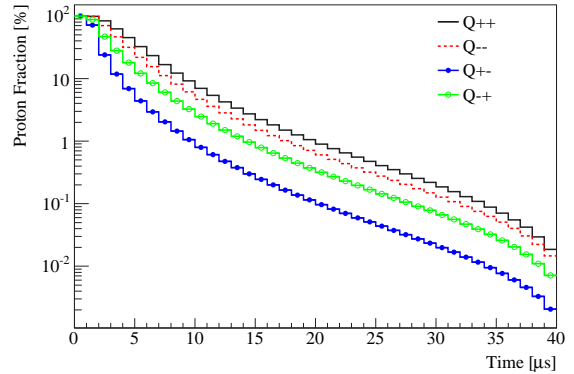
Figure 4.29: Integral of figure 4.28: The fraction of "missing" protons for times $t > 40\mu s$ is smaller than 0.02 % for all four spectra, and the influence on the asymmetries is very small.

	ν-Asymmetry B_{same}	ν-Asymmetry B_{opp}	p-Asymmetry C
Correction Δ_t	$-5(3) \cdot 10^{-4}$	$-1.6(8) \cdot 10^{-3}$	$+3(2) \cdot 10^{-4}$

The asymmetry fit regions were chosen according to the final analysis. Compared to the other corrections and uncertainties, this effect is almost negligible, even if we assume a (certainly overestimated) error of 50 %.

4.3.2 Multi-Stop Measurements

Ideally, a valid event consists of a start-signal (electron) and one single stop (proton). However, sometimes much more stops are detected due to background and accidental coincidences; we measured up to 32 stops per event to account for this. The usual number of stops is much lower as can be seen in this table, where background and accidental coincidences (cf. chapter 4.3.3) already have been subtracted (the numbers are given for start and stop arising in the same detector):

	Detector 1	Detector 2
1 Stop	100.0(2.3) %	100.00(25) %
2 Stops	1.1(1.5) %	3.22(12) %
3 Stops	$-0.6(1.0)$ %	0.00(8) %

No information on neutron decay is left in the 2- and 3-stop events of detector 1, and in the 3-stop events of detector 2 since the stop fraction is compatible with zero. Only in detector 2, there are also neutron related signals in the 2-stop case, however, most of the second stops arise correlated to the first (cf. section 4.3.4). The size of the statistical errors is greater for detector 1 due to its lower proton efficiency and since fewer measurements could be used because of the instable background. For measurements in opposite hemispheres, the same conclusion holds when the stop is detected in the detector given in the table above: Protons are still present in the 2 stop spectrum when detector 1 recognizes the start and detector 2 the stops.

Several stops (besides electron backscattering) occurring in different detectors were not found in the data in a significant amount.

Restriction to 1-Stop Events: In the following analysis of the asymmetries, we restrict ourselves to events with a single stop in the coincidence window. A look at the table given above shows that this case is a restriction only for detector 2 since there are no 2-stop events with proton information in detector 1.

We expect only one proton and hence only one single stop signal (the number of accidental coincidences is quite low due to the small count rate), therefore the additional stops are most likely due to additional background. Thus the restricion to one stop event is a quite appealing possibility to further discriminate between signal and background, especially as the number of 2-stop events is small and does not contribute to the available statistics.

The influence of 2-stop events on the overall result would by tiny anyway: If one analyzes only same hemisphere events with exactly two stops, one finds that the resulting asymmetry B is significantly lower than expected from previous measurements: $B_{2 \text{ Stops}} = 0.895(33)$. All spectra, however, can be well described by the fit functions. We conclude that most of the events are due to neutrons accompanied by a second stop, but a certain fraction is due to background only. Unfortunately, this part cannot be separated from the rest of the data, and it is the systematically cleaner way to omit the two stop events completely. However, if we average the asymmetries from 1- and 2-stop events, it is only shifted by less than 0.25 σ to lower values[10] compared to the 1-stop case. The same holds for the asymmetry B_{opp} in opposite hemispheres, where the effect is approximately twice as high, however, the uncertainties are also much larger.

4.3.3   Accidental Coincidences

Accidental coincidences are due to particles from another decay or background occurring within the coincidence window. As they are not related to the start signal, they do not show the usual time-of-flight distribution, but have an equal probability at any time t. Of course, the last statement is only valid, if they are not suppressed by preceding events, as in the measurement of 2000, where only the first stop signal was registered. In the new experiment, suppression did not longer exist since data acquisition was able to deal with many stops.

We measured the accidental coincidences with the delayed coincidence method: 40 μs after the start signal, less than 0.02 % of all protons have not been arrived at the detector (cf. fig. 4.29), a fraction that can be totally neglected. Hence, all stops arising in the delayed window from 42 to 82 μs are due to background (that can be fully subtracted by a measurement without neutrons) and accidental coincidences. The spectrum of accidental coincidences obtained in the delayed window is now used to correct the asymmetry spectrum measured with a stop in the coincidence window from $0.8 - 40.8$ μs.

It is important to ensure that the condition for the events in the delayed window is exactly the same as in the "normal" coincidence window: An arbitrary number of stops before the window is allowed, besides in the 0.8 μs directly preceding the delayed window: Here no stop

---

[10]The asymmetry B_{same} is lowered due to the remaining background in the 2-stop events that cannot be removed from the data set.
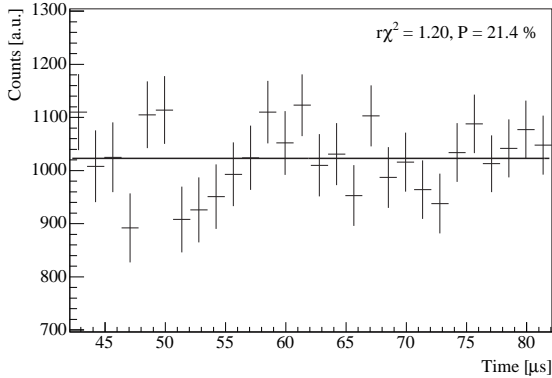
Figure 4.30: Time-of-flight spectrum of the accidental coincidences in the delayed coincidence window of detector 2. The spectrum is flat as expected from a purely random process.
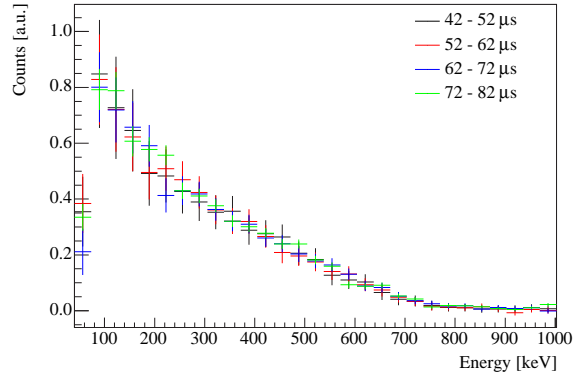
Figure 4.31: Energy spectrum of the accidental coincidences: The delayed window was separated into four intervals whose spectra coincide within the errors.

must occur, analogous to the minimal TOF required for a valid proton. Within the delayed window exactly the number of stops that we are looking for (usually one) has to arise, the number afterwards is again arbitrary.

Systematic Checks: Several checks have been performed to ensure that the accidental coincidences are determined correctly.

- If we denote the probability that one stop occurs in the delayed window with $p(A_1)$, the probability for two accidental is approximately $p(A_1)^2$ and for three $p(A_1)^3$. The measurement (same hemisphere) of exactly one accidental coincidence yields $M_1 = p(A_1) = 0.06093$, where the number of events with one single stop in the coincidence windows was normalized to unity. The measurements M_i and the expected probabilities are shown in the following table:

Stops i	Measurement	Probability
1	$M_1 = 0.06093(64)$	$p(A_1) = 0.06093(64)$
2	$M_2 = 0.00354(22)$	$p(A_1)^2 = 0.00371(8)$
3	$M_3 = 0.00046(13)$	$p(A_1)^3 = 0.00023(1)$

The 2-stop case shows excellent agreement, and the numbers agree within 1.6 σ for three stops.

- The probability that an accidental coincidence signal occurs at a certain time is constant, hence we expect the TOF spectrum of the accidentals to be flat. The measurement, figure 4.30, confirms this. Fitting a straight line to the data yields a slope compatible with zero.

- We splitted the 40 μs delayed window into four equally sized intervals and determined the energy spectrum of the accidentals. All four show the same shape (figure 4.31), the differences agree with zero, and we conclude that the effect of accidental coincidences

on the asymmetries is independent of length (if correctly scaled) and temporal position of the delayed window.

For the final asymmetry analysis, we used a coincidence window from $0.8-40.8$ μs and a delayed window from $42-82$ μs for the same hemisphere measurements, and a coincidence window starting 140 ns earlier to account for the shorter proton drift times in the opposite case. The delayed window was not changed.

Accidentals and the "1-Stop" Condition: When we restrict the analysis to one-stop events only, we have to consider the following systematic effect: In the coincidence window, we find "real" stop events and accidental coincidences; in the delayed window, we have only the latter. If the combination stop-signal plus accidental coincidence arises in the coincidence window, it is not included in the analysis since it is a 2-stop event. However, it actually should be considered to subtract the accidental coincidences correctly, as otherwise too much accidentals are removed from the data, and their influence gets overrated.

Therefore we have to scale down the spectrum of accidental coincidences according to the number of 2-stop events that are due to the combination mentioned above. The scaling factors can be obtained from the measurement itself since we have recorded the overall number of stops of each event. To reduce the influence of the low energy background, we only consider events with electron energies in the interval used for the asymmetry fit.

We denote the probability to obtain one "real" stop in the coincidence window with p_S, and the probability to obtain one accidental stop signal with p_A. The latter is equal for the coincidence and the delayed window, whereas $p_S = 0$ in the delayed window. Measured signals are one (S_1) or two (S_2) stops in the coincidence window and in the delayed window (A_1 and A_2). The corresponding probabilities p, extracted from the data, can be expressed in terms of p_S and p_A, where we neglect terms to the third power due to their smallness:

$$p(S_1) = p_S + p_A - p_S p_A - p_A^2 \tag{4.19}$$
$$p(A_1) = p_A - p_A^2 \tag{4.20}$$
$$p(S_2) = p_S p_A + p_A^2 \tag{4.21}$$
$$p(A_2) = p_A^2. \tag{4.22}$$

Using these relations we can determine the probabilities p_S and p_A. One can clearly see that the 1-stop accidental coincidences $p(A_1)$ do not include a term corresponding to $-p_S p_A$ in equation (4.19). Therefore too much accidentals are subtracted. The size of the effect is given by $p_S p_A$ corresponding to a certain percentage ϵ of accidental coincidences. Accordingly, the spectrum has to be scaled with $\kappa = 1 - \epsilon$, derived independently for beam and background measurements, to eliminate the effect. In the following table, we list the corrections to the neutrino asymmetry B for the different measuring schemes and detectors:

	Detector 1		Detector 2	
	Same	Opposite	Same	Opposite
Correction [%]	$-0.24(6)$	$-0.67(3)$	$-0.13(3)$	$-0.62(9)$

The uncertainties are governed by statistical count rate errors imposing errors on the probabilities p_i. Since the number of accidentals is different for the hemispheres and since they depend on electron trigger rate and proton efficiency, the four factors are not equal.

After having obtained the probalilities p_S, p_A from equations (4.19) and (4.20), one can use equations (4.21) and (4.22) for cross checks of the results.

4.3.4 Events with correlated second Stop

Although we do not consider events with more than one stop, we want to give some comments on events with two stops in this section. Especially, we will focus on two stop events in detector 2, where the second stop comes coincident with the first – after a particular time difference Δt – in almost all cases.

Correlations between Events: Whenever an event occurred, we measured the time within the measuring cycle with the low resolution TDC, introduced in section 3.4.4. From this we can obtain the time difference between two events. All checked subsets (all events, only 1-stop events, only 2-stop events, etc.) show the expected exponential behaviour for the time difference disctribution and we have not found any correlations between events.

Correlation within Events: Since we recorded many stops within an event, we can also check for correlations here, and find that the second stop in detector 2 appears correlated to the first in almost all 2-stop cases. The time difference Δt between the stops is shown in figure 4.32, it has a sharp peak at 170 ns with a FWHM of 9 ns. The coincident second signal arises only in detector 2 (D2), but in all possible stop combinations, e.g:

> Start D2 - Coincident Stop D2
> Start D2 - Stop D2 - Coincident 2nd Stop D2
> Start D1 - Stop D2 - Coincident 2nd Stop D2
> Start D2 - Stop D2 - Coincident 2nd Stop D2 - arbitrary 3rd Stop D2.

Many systematic tests to obtain the characteristics of this signal were performed yielding the following results:

- The coincident second stop is correlated with the presence of protons: It occurs only in measurements with opened neutron beam and is not present in background and calibration measurements, as well as in measurements without high voltage.

- Approximately 85 % of all two-stop events show the correlated second stop.

- The signal is independent of the spinflipper status.

- It is independent of the electron trigger-rate.

- One cannot use the energy spectrum of the stops to distinguish between the two signals since the energy distribution is equal.
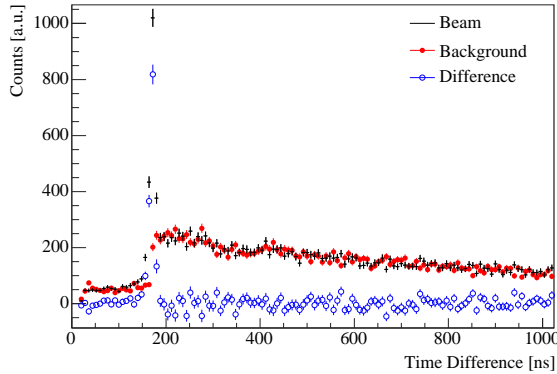
Figure 4.32: Example for the correlated second stop in detector 2. Shown is a same hemisphere measurement, i.e. start and two stop signals in detector 2. The time difference between first and second stop peaks sharply at 170 ns. Almost all signals appear in the peak.
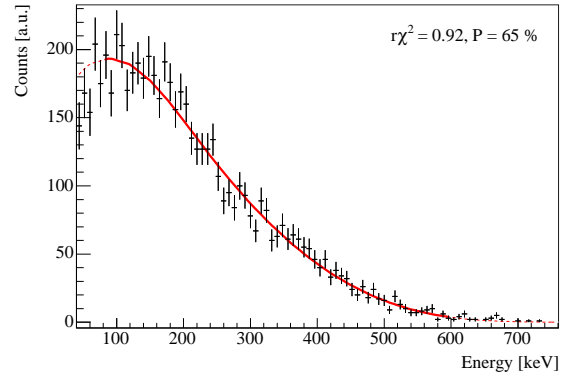
Figure 4.33: Electron (start) spectrum of the two stop signals from figure 4.32. Since it is the sum of both spinflipper states, we try to describe the spectrum with the sum spectrum S for same hemisphere data, what fits very well. Hence, there is no energy cut in the two-stop events.

- The electron energy spectrum of events with a coincident second stop can be perfectly described with a fit of the sum-spectrum S (that has to be chosen according to the hemispheres in which start and stops are detected: same or opposite). An example is shown in figure 4.33.

- The time-of-flight spectrum of the 2-stop events, which is a measure of the angular distribution of the particles generating the stop, has the same shape as the 1-stop case. Only for opposite hemispheres, a small difference appears at the steep rising slope of the spectrum.

- The second stop cannot be explained by a proton crossing the carbon foil a second time ("swing-through") generating additional secondary electrons. The time scale of such an event would be around 10 ns only [Bra00].

Unfortunately, we cannot explain the origin of this signal. Its occurrence at only one detector and the rather sharp peak would indicate an electronics problem, however, it only appears in one particular kind of measurement and seems to be related to protons. Therefore we decided to omit this data in the final analysis what can be justified by the following arguments:

- The occurence of events with several stops is most probably related to additional background since a single decay only generates a single proton. The combination signal plus accidental coincidence only accounts for 25 % of the cases.

- The electron spectrum can be well described by a fit of the corresponding sum-function, and the time-of-flight spectrum – a measure for the angular distribution of the decay products – agrees with the one-stop case[11]. This indicates that we have neither energy nor angular cuts associated with the coincident second stops.

---

[11]For opposite hemispheres, one can see a declining ratio at the rising edge of the TOF spectrum

- The 2-stop events cause a shift of the asymmetry B_{same} that is smaller than 0.25 σ. This is completely irrelevant (cf. chapter 4.3.2).

4.4 Background and Data Reduction

The background difficulties associated with high voltage effects have already been mentioned at different places, and conclusions have been made on its origin. In this chapter, we describe how we dealt with the background and present a data reduction scheme allowing to obtain a data set with reduced background. In the final analysis of this data, background is even further reduced by requiring a coincident stop for valid events.

4.4.1 Formalism of Data Reduction

We recall, that a measurement is a longer period $(0.3-15$ h$)$, where data acquisition was not interrupted and no external settings (high voltage, thresholds) were changed. With a length of 2 seconds, a cycle is the shortest subset in a measurement, corresponding to a particular shutter, spinflipper, calibration source combination. In figure 4.34, one data point corresponds to one cycle. To extract the correlation coefficients in neutron decay, we only use measurements performed at high voltages of at least -14 keV in order to have reasonable proton efficiencies. Additionally, they must have been stable in terms of high voltage background. In many cases, however, it is sufficient to remove only the cycles with sparkovers etc. from the data set, instead of rejecting the whole measurement.

To determine whether a cycle should be used or removed, the following data reduction procedure was developed. It assigns a number to each cycle indicating its deviation from the mean count number. This number is not constant in time but drifts slightly up and down, what has to be taken into account. The procedure includes five steps:

1. All cycles of similar type (e.g. neutron beam on and spinflipper off) are merged into up to 80 consecutive packages.

2. In each package, we determine the median[12] to avoid that single count number mavericks get too much weight.

3. To account for drifts, a polynomial of 4th order is used to describe the evolution of the median in time. All cycles with count numbers N differing more than $3\,\sigma = 3\sqrt{N}$ from this function are ignored for the moment.

4. From the remaining cycles, the mean value is calculated in each package. Again a polynomial of 4th order is used to describe the evolution of the mean.

5. In a final step, we determine the deviation from the mean for every cycle in the data set. This number (again given in σ, the square root of the count number) is assigned to each cycle and can be used to reject cycles in a reasoned manner.

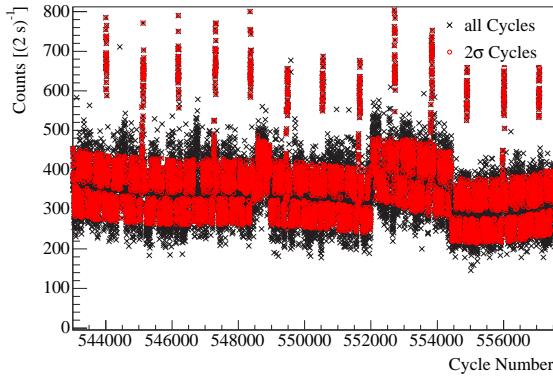[12]The median of n numbers x_i is the value x_m where half of the numbers x_i is smaller than x_m, and half is larger.

Figure 4.34: Data reduction of detector 1: Shown is the count rate for all cycles (2 s) and for the cycles with a deviation smaller than 2 σ from the mean. The sudden count rate jumps had to be considered separately.
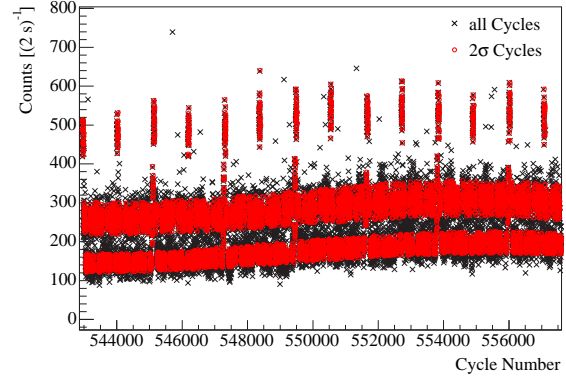
Figure 4.35: Data reduction of detector 2: It is more stable than detector 1, there are no sudden count rate jumps. Data reduction is done separately for beam and background measurements and flipper status.

The polynomials used are just phenomenological descriptions of the long time drift and not based on an underlying theory. Linear drifts on smaller time scales are automatically compensated by the spinflipper scheme applied in the measurement,

$$\text{On Off Off On Off On On Off,}$$

where On or Off indicate the flipper state of one cycle. This scheme was also used to switch between beam and background measurements.

Examples for this procedure are given in figures 4.34 and 4.35 for detector 1 and 2 respectively: The black points indicate the whole data set, whereas the red ones are the cycles remaining if all cycles with deviations larger than 2 σ are rejected. Please note that σ is not one fixed number but changes with the number of counts per cycle. For detector 2, this procedure works very well since the drift is continuous. In detector 1, we sometimes face sudden steps in the count rate that cannot be described by a polynomial. These cases had to be removed by hand to ensure that the automatic procedure works.

Determination of the Rejection Threshold: We determined the asymmetries B_{same} and B_{opp} with different rejection thresholds to check their influence on the result. Due to the smaller proton efficiency and very instable high voltage background, most of the measurements where detector 1 serves as proton detector cannot be used for analysis. The remaining combinations are B_{same} where detector 2 measured electron and proton, and B_{opp} with the electron identified in detector 1 and the proton in detector 2. Anyhow, we use the thresholds given below also for the other two cases.

For the asymmetry B_{opp}, no effect of the rejection threshold σ can be seen if the fit region is chosen to start at energies high enough. The asymmetries for the data sets $0 - 2 \ \sigma$ and $2 - 10 \ \sigma$ coincide within the statistical errors ($r\chi^2 = 1.15$, $P = 58 \ \%$). Therefore we use the 10 σ threshold in this case; this includes almost all data besides a few cycles with extreme sparkovers.
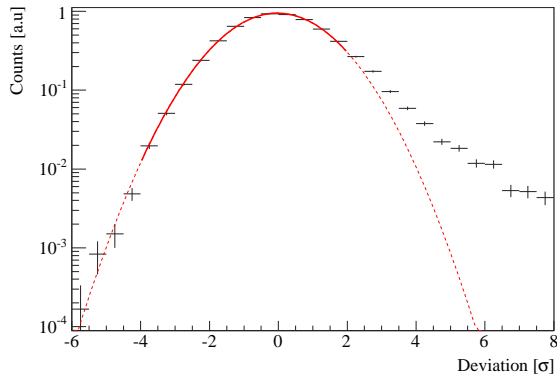
Figure 4.36: Deviation from the mean beam count rate obtained with the data reduction method described in the text. On the low count rate side, it can be described by a Gauss fuction, but for higher rates more deviations exist due to high voltage effects that can only increase the rate.
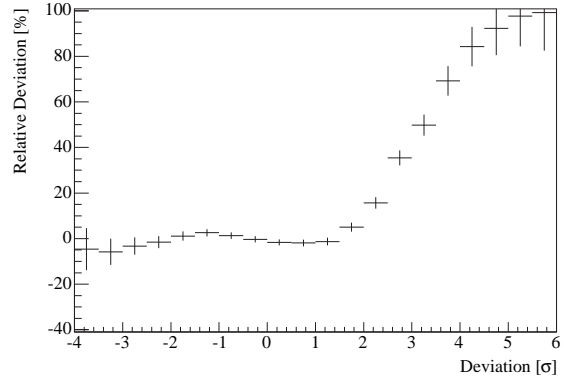
Figure 4.37: Relative deviation between data and Gauss curve of fig. 4.36: There is no significant difference up to 2σ, then the deviation begins to grow due to increased background. This is the reason for the reduction (≈ 0.5 stat. standard deviations) of the asymmetry B_{same} starting at 2σ.

However, when we perform this analysis for the same hemisphere, we find that B_{same} for the disjunct data sets $0-2\ \sigma$ and $2-10\ \sigma$ differs by more than three sigma (statistical error). Further analysis shows that the asymmetry stays constant from $0-2\ \sigma$, but a sudden step to a lower asymmetry occurs at $2\ \sigma$, which then stays again constant with increasing σ.

Most likely this step is due to background entering the data set only for $\sigma > 2$. This can be explained by figure 4.36: The histogram shows the number of cycles with a given deviation from the mean value. If the measurement process would be purely statistical, we would expect a Gaussian distribution around zero. However, we operated a system with high voltage inducing additional background. This can only increase the count rate and never lower it. Therefore, we fit a Gauss function from low to medium count rates to the data and yield a statistically satisfactory fit-result. Higher deviation values cannot be described by the Gaussian, there is a small but significant fraction of additional background above $2\ \sigma$ (figure 4.37) lowering B_{same} by about 0.5 statistical standard deviations. Because of this, we set the rejection threshold for the same hemisphere to $2\ \sigma$. Please remember that background is much smaller in opposite hemispheres (cf. chapter 3.5) allowing us to use the much larger threshold of $10\ \sigma$ as mentioned above.

If the description of the mean count rate's temporal evolution with the polynomial works satisfactory, we expect the center of the Gauss function to be at $0\ \sigma$. The fit from figure 4.36 gives exactly this result.

4.4.2 Systematic Background Checks

Systematic checks on the background have been performed to ensure that it behaves as expected, and that no systematic errors due to background alter the measurement:

- The spectra of background and calibration sources are independent of the spinflipper status in the whole energy range, when the cycles are chosen according to the scheme described above. This also holds if one only analyzes the fit region.

- The energy content of difference $D = Q^{--} - Q^{++}$ and sum $S = Q^{--} + Q^{++}$ spectra should be zero above the endpoint energy of the β-spectrum. To account for the rather low energy resolution of the plastic scintillator we checked a region from $970-1110$ keV: The fit of a constant agrees with zero, no background is left.

- The difference of two Q^{++} spectra, for example, measured at two different times is zero. This is expected when background drifts are handled correctly.

- When the "background free" difference D, and the sum spectrum S are fitted, we have only one free parameter, a normalizing factor N. This factor should be the same for both spectra if no additional background is present in S. This was proven in the analysis, N_D and N_S agree within the errors, where the fit was performed in the region of the B_{same} analysis. However, the conclusion from this analysis – no background in the sum spectrum – is only valid within the precision of the fit results. These are statistically limited to 0.25 %.

4.5   Corrections and Systematic Effects

PERKEO II provides a setup where systematic corrections to be applied to the measured value are very small; they are in the order of 1.0 %. Compared to previous precise measurements of the neutrino asymmetry B, where the quoted corrections were quite large (≈ 33 % in [Kuz95], ≈ 5 % in [Ser98]), this is one of the big advantages of this experiment.

In this chapter, we will briefly introduce the corrections and make some remarks on how they can be determined. If necessary, the electron energy-dependent correction functions were directly included into the fit routines.

4.5.1   Theoretical Corrections

These corrections are the same for all neutron decay experiments, since they have to be applied to the Fermi spectrum, the basic expression to describe the measurements analytically. It is the phase-space factor in the decay probability (2.30),

$$F'(E) = (E_0 - (E + m_e))^2 \sqrt{(E + m_e)^2 - m_e^2} \ (E + m_e) \tag{4.23}$$

and gives the electron energy distribution of unpolarized neutron decay. E is the electron's kinetic energy, E_0 the endpoint energy, and m_e its mass. However, effects inherent to the decay process change the spectral shape and the spectrum has to be corrected. It now reads

$$F(E) = F'(E) \ (1 + \delta_R(E)) \ (1 + R(E)) \ F_C(E), \tag{4.24}$$

with the Coulomb correction $F_C(E)$, recoil correction $R(E)$, and outer radiative corrections $\delta_R(E)$. All contributions are very small and have almost no effect on the asymmetries.

Coulomb Correction: To account for the attractive electromagnetic force between proton and electron, Fermi introduced the correction function

$$F_C(E) = \frac{2\pi\alpha\beta^{-1}}{1 - \exp(-2\pi\alpha\beta^{-1})}, \qquad \text{with } \alpha = \frac{e^2}{\hbar c}, \text{ and } \beta = \frac{v}{c}. \tag{4.25}$$

It is a classical approximation better than $5 \cdot 10^{-4}$ for $E > 5$ keV [Bae96] which is sufficient for our purpose.

Recoil Correction: The equations given in the introductory chapter are derived assuming an infinitely heavy proton. Although the proton is 2000 times heavier than the electron, it has a finite mass, and proton recoil effects have to be taken into account. The correction was calculated by [Wil82], here we present only a shortened expression where constants have already been inserted. Mass and energy are given in keV:

$$R(E) = 0.001 \left(-3.57 - \frac{722}{E + m_e} + 0.00766 \, (E + m_e) \right). \tag{4.26}$$

Outer Radiative Corrections: In the most simple picture, neutron decay is just mediated by a single W-boson exchange. However, there are processes of higher order that have to be considered, e.g. the emission of a bremsstrahlung photon from the electron or corrections to the vertex. These radiative corrections can be separated in an outer part, that is model independent and mainly due to QED effects, and an inner part that strongly depends on the structure of the weak and strong interaction. Only the outer radiative corrections, given by [Sir67], change the shape of the Fermi spectrum:

$$\delta_R(E) = \frac{\alpha}{2\pi} \cdot (t_1 + t_2 + t_3 + t_4) \tag{4.27}$$

with

$$\begin{aligned}
t_1 &= 3 \, \log(\frac{m_p}{m_e}) - \frac{3}{4} \tag{4.28} \\
t_2 &= 4 \, (\frac{\text{atanh}(\beta)}{\beta} - 1) \cdot \left(\frac{E_0 - (E + m_e)}{3(E + m_e)} - \frac{3}{2} + \log(\frac{2(E_0 - (E + m_e))}{m_e}) \right) \\
t_3 &= \frac{4}{\beta} \cdot L(\frac{2 \, \beta}{1 + \beta}) \\
t_4 &= \frac{\text{atanh}(\beta)}{\beta} \cdot \left(2 \, (1 + \beta^2) + \frac{(E_0 - (E + m_e))^2}{6(E + m_e)^2} - 4 \, \text{atanh}(\beta) \right)
\end{aligned}$$

and the Spence-Function

$$L(z) = \int_0^z \frac{\log(1 - x)}{x} \, \mathrm{d}x. \tag{4.29}$$

The model dependent inner radiative corrections Δ_R are of the order of 2 % (see e.g. [Glu03]), do not change the spectrum, and can be absorbed into the coupling constants. They do not have to be considered here.

In agreement with the calculations of Sirlin [Sir67], Glück [Glu98, Glu03] concludes that the effect of the model-independent outer radiative corrections δ_R can be completely neglected in the asymmetry measurements. New calculations using effective field theories confirm these results [And04]. However, we also want to mention that there is a suggestion that δ_R should be much larger [Bun06].
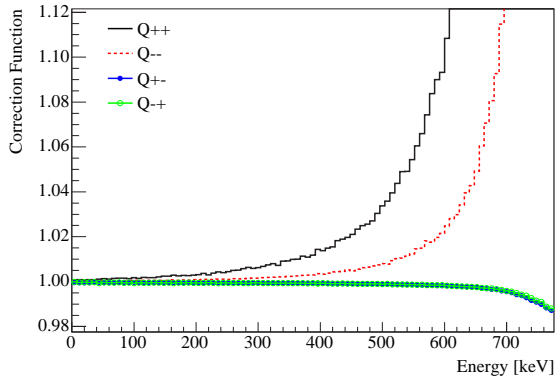
Figure 4.38: Correction functions for the Q-spectra to account for the magnetic mirror effect. The correction is applied by multiplying the fit function with the functions given here. Whereas the spectra measured in opposite hemispheres (Q^{+-}, Q^{-+}) are hardly affected, the corrections for Q^{++} and Q^{--} get very large for higher energies, imposing an upper limit for a reasonable fit region.

4.5.2 Magnetic Mirror Effect

The magnetic mirror effect [Jac02], i.e. the possibility of a momentum turn in an increasing magnetic field, was already described in chapter 3.3.3. It is the only systematic effect arising due to the magnetic field, since Stern-Gerlach-effects are much too small to be relevant here [Kre04b].

We obtained the correction functions for the general magnetic mirror effect[13], and for various displacements Δ between neutron beam and magnetic field maximum from a Monte Carlo simulation [Dei05]. It features

- the real PERKEO magnetic field,

- the neutron beam profile,

- and the electron's momentum turn of the magnetic field.

Another simulation of the setup was performed by F. Glück [Glu05]. The results agree within 0.2 %, what is a sufficient agreement if one takes into account that the overall magnetic mirror correction to the spectra has a size in the percent range.

The correction functions for the four different Q-spectra are shown in figure 4.38: Whereas the opposite hemisphere spectra are hardly affected, the magnetic mirror effect gets quite large for Q^{++} and Q^{--}.

4.5.3 Displacement between Neutron Beam and Magnetic Field

In general, the displacement Δ between neutron beam and magnetic field maximum constitutes no problem, since it cancels when one averages the asymmetries B_{same} of both detectors (cf. chapter 3.3.3). However, we have to deal with the situation that only detector 2 worked quite stable and provides much more data than the other. Therefore, the two asymmetries B_{same} are statistically not comparable and we would spoil the statistical precision reached with detector 2 by simple averaging. For B_{opp} and the proton asymmetry C this is not crucial since the mirror effect is almost negligible.

---

[13]This means the effect with a displacement $\Delta = 0$ mm.

In this section, we will show that it is possible to determine the displacement Δ very precisely, which decreases its influence on B_{same} quite remarkable. We have developed procedures to obtain Δ from the data itself. The basic idea for both methods presented below is that the experiment was performed with a particular displacement, and we can identify it by analyzing its effects on the spectra. To do so, we used the magnetic mirror correction spectra, computed for different displacements.

χ^2-Minimization: The displacement Δ changes the electron energy distribution in the different spectra. We found that the difference spectrum $D_{\text{same}} = Q^{++} - Q^{--}$ has the highest sensitivity on Δ. If we now describe measured data with the function D, a function without free parameters besides a normalizing factor, we expect to obtain the best fit result when we have applied the correction function for the real displacement. An example is shown in figure 4.39: The fit region starts well above the low energetic background and extends to quite high energies to increase sensitivity on magnetic mirror effect and displacement.

The χ^2 of the fits performed with different Δ were recorded, see figure 4.40. A quadratic equation is used to describe the curve, and we obtain the best value for the displacement from the minimum χ^2_{min}; the one standard deviation error corresponds to the positions with $\chi^2_{\text{min}} + 1$.

The same procedure can also be employed to analyze detector 1, however, its sensitivity on Δ is much smaller due to low statistics. We get the following results:

$$\Delta_1 = (0.35 \pm 0.55)\,\text{mm} \qquad \text{for detector 2, and} \qquad (4.30)$$
$$\Delta_2 = (0.11 \pm 1.69)\,\text{mm} \qquad \text{for detector 1.} \qquad (4.31)$$

The method requires the spectra not to be affected by imprecise implementations of the other corrections, namely edge and grid effect (cf. chapters 4.5.5, 4.5.6). Their influence has been checked quantitatively: A linear distortion of 5 %, corresponding to the addition of a straight line to the edge and grid effect correction functions, yields a maximal displacement shift of 0.05 mm, what is much smaller than the quoted error.
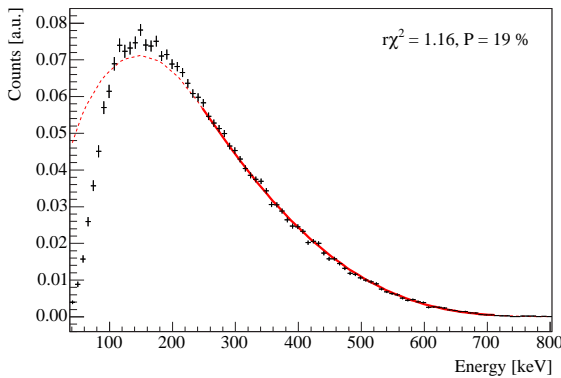

Figure 4.39: Example for a fit of the difference spectrum D_{same} of detector 2 to obtain information on the displacement Δ between neutron beam and magnetic field.
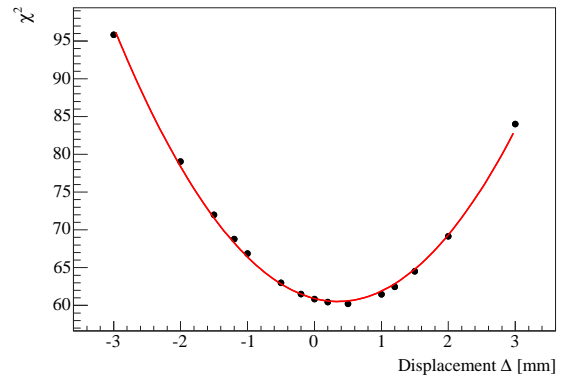
Figure 4.40: The displacement Δ was varied in the sum fits of detector 2, the resulting χ^2 is plotted here. The minimum of the χ^2 parabula is located at $\Delta = 0.35(55)$ mm.
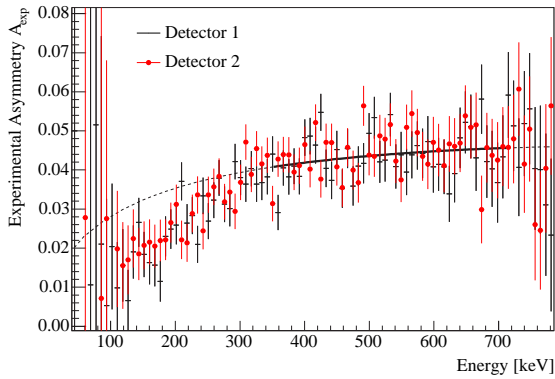
Figure 4.41: Electron asymmetry A for both detectors with a fit to detector 1. The difference in the asymmetries can be used to extract the displacement Δ from measured data.
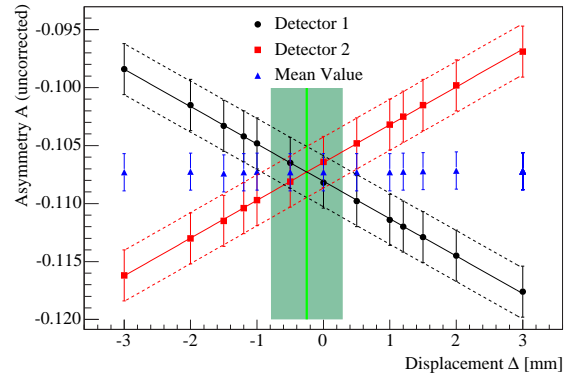
Figure 4.42: Averaging the electron asymmetry fit results with different displacements Δ yields a constant. The results of the detectors coincide at the "real" displacement: $\Delta = (-0.25 \pm 0.54)$ mm.

Δ_1 and Δ_2 from the χ^2-minimization show nice agreement with the result of the direct measurement,

$$\Delta_3 = (1.0 \pm 1.4) \text{ mm}, \tag{4.32}$$

however, the uncertainty of Δ_1 is much smaller.

Electron Asymmetry A: The spectra associated with the asymmetry B_{opp} from opposite hemispheres cannot be used to obtain further information on the displacement since they are almost independent of the magnetic mirror effect. Alternatively, we can use measurements performed without proton detection: Whenever the vacuum was not good enough to apply high voltage onto the detector foils, or extreme background conditions forced us to turn off the voltage, we acquired pure electron spectra anyway. In principle, these could be analyzed to extract the electron asymmetry A, however, now the coincidence condition cannot be applied, and the large beam related background does not allow to obtain precise absolute A-values[14].

On the other hand, without high voltage we have two electron detectors of the same quality, providing results with the same statistical error. The relative difference between the A values of both detectors (figure 4.41) is only caused by Δ, the asymmetric positioning of the neutron beam relative to the magnetic field, assuming an equal beam-related background on both detectors. This is a realistic assumption, since the PERKEO IIB-setup was highly symmetric (with the "background source" beamline as symmetry axis), and we chose a fit region starting at very high energies ($E > 350$ keV). Here beam-related background is strongly suppressed since it arizes mainly below 200 keV [Mun06].

The asymmetry spectra were fitted employing different displacement correction functions, cf. figure 4.42. Averaging the values with equal Δ yields a constant, and the results of both detectors coincide at the "real" displacement Δ. The uncertainty is determined by the projection of the error ellipse (i.e. the contour with $\chi^2 = \chi^2_{\mathrm{min}} + 1$) onto the Δ-axis, leading to the result:

$$\Delta_4 = (-0.25 \pm 0.54) \text{ mm}. \tag{4.33}$$

---

[14]Statistics would also be much too low to get a result for the asymmetry A competitive to the current best measurements [Abe02, Mun06].
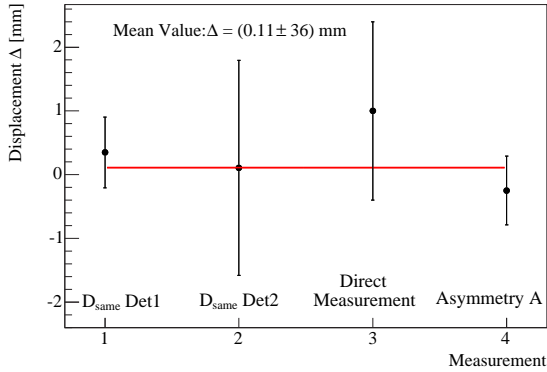
Figure 4.43: The figure shows the results for the four individual determinations of the displacement Δ between neutron beam and magnetic field maximum: The first two values were obtained from the difference D_{same}. Details on the direct measurement can be found in chapter 3.3.3. The last point stems from a comparison of the electron asymmetries of both detectors. The values show excellent agreement, the average is $\Delta = (0.11 \pm 0.36)$ mm, where the positive sign indicates a displacement towards detector 2.

Final Displacement Result: The four independent values $\Delta_1 - \Delta_4$ from independent data sets are presented in figure 4.43. They show excellent agreement. Averaging yields a mean value

$$\Delta = (0.11 \pm 0.36) \text{ mm}, \tag{4.34}$$

where the positive sign indicates a shift towards detector 2.

Compared to the direct measurement, the methods introduced above allow to reduce the uncertainty of the displacement considerably, however, it is still the largest systematic error in the determination of the neutrino asymmetry B from same hemispheres.

4.5.4 Electric Mirror Effect

Since the proton-to-electron converter foil is on negative potential U we have to consider its repulsive effect on the decay electrons. Detailed studies can be found in [Dei05], here, we only give a short summary: The electrons pass the electrostatic barrier if their kinetic energy parallel to the electric field lines is larger than $E_\parallel = eU$. However, the parallel component increases in a decreasing magnetic field due to the momentum turning in flight direction. To cover the worst case, we have to calculate the minimal kinetic energy $E_{\min}$ of an electron emitted perpendicular to the electric (and magnetic) field lines, i.e. with an initial energy $E_\parallel(0) = 0$, neccessary to overcome the potential barrier. For the realized PERKEO II setup, this energy is $E_{\min} = 84$ keV.

Electrons with higher energies are not affected by the electric field at all, since decay volume and scintillator are both on ground potential. Electrons with lower energies may be repelled by the foil, however, this is not crucial since we use fit regions starting at much higher energies to obtain the asymmetries. We can therefore totally neglect the electric mirror effect.

4.5.5 Edge Effect

Since we measure with a continous neutron beam we have to confine the decay volume length along the beam direction to establish well defined border conditions[15]. Now, some of the

---

[15]An alternative would be a measurement with a chopped neutron beam and a data acquisition system that is only active when the neutron cloud is located within the decay volume. This, however, is not realizable with PERKEO II since the effective count rate would be much too low [Bre03].
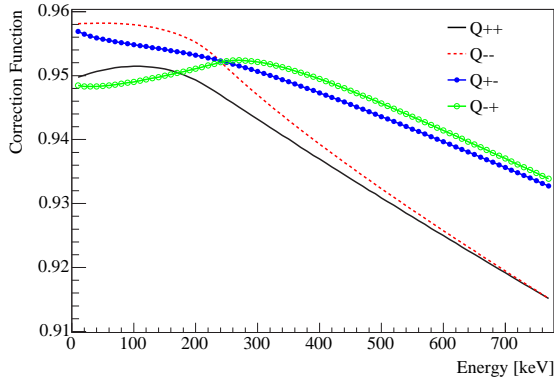
Figure 4.44: Edge effect correction spectra: This effect is due to the finite lenght l=90 mm of the decay volume that is limited by thick aluminium baffles.
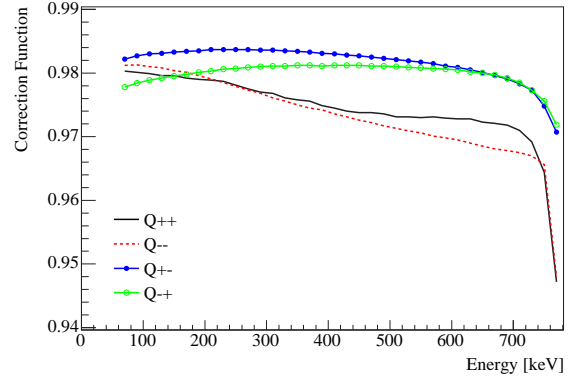
Figure 4.45: Correction functions to account for the grid effect. It arises because of the thin wires between decay volume and high voltage foil to prevent electrical reach-through.

charged particles hit the aluminium baffles installed for this purpose and get absorbed; this gives rise to the edge effect.

Electrons and protons gyrate around the magnetic field lines. If they are created in a region close to the ends of the decay volume, they may hit the baffles depending on their gyration radius r_g. Please note, that the radii of electron and proton are coupled in a coincidence measurement, what has to be taken into account in the simulation of the effect. We use "thick" baffles, i.e. they have a length of 30 mm along the particles flight direction, assuring that the baffles get hit at least two times. This way, particles that were only scattered first may get absorbed the second time, increasing the overall absorption probability close to unity.

The correction spectra (figure 4.44) were also obtained in two independent Monte Carlo simulations [Dei05, Glu05] for cross check reasons. Again, there was no significant difference in the result.

4.5.6   Grid Effect

Four grids made out of thin aluminium wires were placed between high voltage foil and decay volume to avoid changes in the initial flight direction of the charged particles due to the electric field. However, the wires disturb the trajectories of some electrons and protons respectivley and cause a slightly energy dependent grid effect.

Whereas protons are absorbed in the wires, electrons may be scattered or absorbed. The effect on the spectra was studied by F. Glück [Glu05] using the Monte Carlo program *PENELOPE* [Bar95] that allows to simulate the motion of particles in different materials. The resulting correction spectra are shown in figure 4.45: Although corrections are of the order of $2-3$ %, the functions are very similar for the two same hemisphere spectra and the two other as well. This yields small overall corrections to the asymmetries since the effects cancel.

The exact size of all corrections mentioned here depends on the fit regions chosen for the analysis, the final numbers for the asymmetries B_{same}, B_{opp}, and the proton asymmetry C can be found in the tables 4.2, 4.3, and 4.4 respectively.

4.6   Neutrino Asymmetry B – Same Hemispheres

Now, we have prepared everything to finally extract the asymmetries B and C. We will start with the analysis of the neutrino asymmetry B_{same} consisting of same hemisphere events. The very first section, however, will introduce the general expressions und uncertainties used for all correlation coefficients.

4.6.1   Spectra and Errors

To extract correlation coefficients from data, we have to generate several spectra with different spinflipper states. The two spinflipper states (on/off) are used to obtain the asymmetries from one detector; this avoids effects due to different detector functions. Starting point for all cases, i.e. same and opposite hemisphere measurements, are the following spectra

- N_{on}, N_{off}: measurements with neutron beam, spinflipper on/off

- N_{bg}: background measurement, both flipper states

- N_{on}^{a}, N_{off}^{a}: accidental coincidences when beam is off, spinflipper on/off

- $N_{\mathrm{bg}}^{\mathrm{a}}$: accidental coincidence, background,

with the uncertainties $\mathrm{d}N_{\mathrm{on}}$, $\mathrm{d}N_{\mathrm{off}}$, $\mathrm{d}N_{\mathrm{bg}}$, etc. given by the square-root of counts. The spectra are obtained from the data applying conditions (e.g. start and stop in detector 2) and cuts (e.g. only 2 σ data). We have to scale all spectra to count rate $[\mathrm{s}^{-1}]$ since the particular number of usable cycles for one spectrum certainly differs from the others. The accidental coincidence spectra have to be multiplied with the scaling factor κ, determined in chapter 4.3.3, to account for the suppression of regular stops due to the "1-stop" condition.

First of all, we have to generate the background subtracted spectra Q_{on} and Q_{off} corresponding to one of the Q^{ij} functions (depending on neutron spin orientation, and where electron and proton are detected):

$$\begin{align}
Q_{\mathrm{on}} &= N_{\mathrm{on}} - N_{\mathrm{bg}} - N_{\mathrm{on}}^{\mathrm{a}} + N_{\mathrm{bg}}^{\mathrm{a}} \tag{4.35}\\
Q_{\mathrm{off}} &= N_{\mathrm{off}} - N_{\mathrm{bg}} - N_{\mathrm{off}}^{\mathrm{a}} + N_{\mathrm{bg}}^{\mathrm{a}}. \tag{4.36}
\end{align}$$

From this, difference D and sum S can be constructed and the errors $\mathrm{d}D$, $\mathrm{d}S$ can be calculated:

$$\begin{align}
D &= Q_{\mathrm{off}} - Q_{\mathrm{on}} = N_{\mathrm{off}} - N_{\mathrm{on}} - N_{\mathrm{off}}^{\mathrm{a}} + N_{\mathrm{on}}^{\mathrm{a}} \tag{4.37}\\
\mathrm{d}D &= \sqrt{\mathrm{d}N_{\mathrm{off}}^{2} + \mathrm{d}N_{\mathrm{on}}^{2} + \mathrm{d}N_{\mathrm{off}}^{\mathrm{a}\,2} + \mathrm{d}N_{\mathrm{on}}^{\mathrm{a}\,2}} \tag{4.38}\\
S &= Q_{\mathrm{off}} + Q_{\mathrm{on}} = N_{\mathrm{off}} + N_{\mathrm{on}} - 2N_{\mathrm{bg}} - N_{\mathrm{off}}^{\mathrm{a}} - N_{\mathrm{on}}^{\mathrm{a}} + 2N_{\mathrm{bg}}^{\mathrm{a}} \tag{4.39}\\
\mathrm{d}S &= \sqrt{4\mathrm{d}N_{\mathrm{bg}}^{2} + \mathrm{d}N_{\mathrm{off}}^{2} + \mathrm{d}N_{\mathrm{on}}^{2} + 4\mathrm{d}N_{\mathrm{bg}}^{\mathrm{a}\,2} + \mathrm{d}N_{\mathrm{off}}^{\mathrm{a}\,2} + \mathrm{d}N_{\mathrm{on}}^{\mathrm{a}\,2}}. \tag{4.40}
\end{align}$$

The asymmetry B reads:

$$B = \frac{D}{S} \tag{4.41}$$

$$
\begin{aligned}
\mathrm{d}B \quad = \quad & 2\Big[\Big\{\mathrm{d}N_{\mathrm{on}}^2\left(N_{\mathrm{bg}}-N_{\mathrm{off}}-N_{\mathrm{bg}}^{\mathrm{a}}+N_{\mathrm{off}}^{\mathrm{a}}\right)^2 + \mathrm{d}N_{\mathrm{on}}^{\mathrm{a}\,2}\left(N_{\mathrm{bg}}-N_{\mathrm{off}}-N_{\mathrm{bg}}^{\mathrm{a}}+N_{\mathrm{off}}^{\mathrm{a}}\right)^2 \\
& +\mathrm{d}N_{\mathrm{off}}^2\left(N_{\mathrm{bg}}-N_{\mathrm{on}}-N_{\mathrm{bg}}^{\mathrm{a}}+N_{\mathrm{on}}^{\mathrm{a}}\right)^2 + \mathrm{d}N_{\mathrm{off}}^{\mathrm{a}\,2}\left(N_{\mathrm{bg}}-N_{\mathrm{on}}-N_{\mathrm{bg}}^{\mathrm{a}}+N_{\mathrm{on}}^{\mathrm{a}}\right)^2 \\
& +\mathrm{d}N_{\mathrm{bg}}^2\left(N_{\mathrm{off}}-N_{\mathrm{on}}-N_{\mathrm{off}}^{\mathrm{a}}+N_{\mathrm{on}}^{\mathrm{a}}\right)^2 + \mathrm{d}N_{\mathrm{bg}}^{\mathrm{a}\,2}\left(N_{\mathrm{off}}-N_{\mathrm{on}}-N_{\mathrm{off}}^{\mathrm{a}}+N_{\mathrm{on}}^{\mathrm{a}}\right)^2\Big\} \\
& \times\Big\{2\,N_{\mathrm{bg}}-N_{\mathrm{off}}-N_{\mathrm{on}}-2\,N_{\mathrm{bg}}^{\mathrm{a}}+N_{\mathrm{off}}^{\mathrm{a}}+N_{\mathrm{on}}^{\mathrm{a}}\Big\}^{-4}\Big]^{1/2}
\end{aligned}
\tag{4.42}
$$

Now we have five spectra for each set of hemisphere combination and detector: Two Q-spectra, difference D, sum S, and asymmetry B. Although the correlation coefficient is only obtained from the asymmetry, the others are important to check systematics. We want to emphasize that there is only one free parameter in all fits, either the correlation coefficient itself, or a normalizing factor. All other neccessary parameters like gain, energy offset, energy resolution, polarization, etc. were determined in other measurements.

4.6.2   Analysis

We use all data with high voltages above $U = -14$ kV for the analysis of B_{same} measured with detector 2. Due to the sometimes very instable high voltage and higher discriminator thresholds, much less measurements can be used for detector 1. Additionally, its proton efficiency is smaller, hence we have two detectors that are not comparable in terms of statistics. As explained in the previous sections of this chapter, we use $2\,\sigma$ data and consider only events that have exactly one stop in the coincidence or the delayed window.

Fit Region: The fit region is chosen on order to get the smallest combined statistical and systematical error. Additionally, it has to fulfill several conditions: First of all, the obtained asymmetry must be independent of small changes in the fit region. Secondly, the region must not be extended to too low energies, since there is still some background left that would influence the result. At the high energy side, the fit interval should be limited to decrease the influence of the magnetic mirror effect, but one has to balance this with the increasing statistical error. For detector 2, this is shown in figure 4.49. At last, we require that all relevant spectra used to generate the asymmetry, i.e. Q^{++}, Q^{--}, difference D, and sum S, can be described with fit probabilities $P > 5$ % in the fit interval or in a larger region including it (cf. figure 4.46). This is the common limit to define if the disagreement beween observed and expected distribution is significant [Tay97], a larger probability thus indicates that the measurement can be statistically described by the fit.

The fit intervals that were finally chosen (cf. figures 4.47 and 4.48) for the analysis are:

	Detector 1	Detector 2
Fit Region [keV]	245−455	250−455

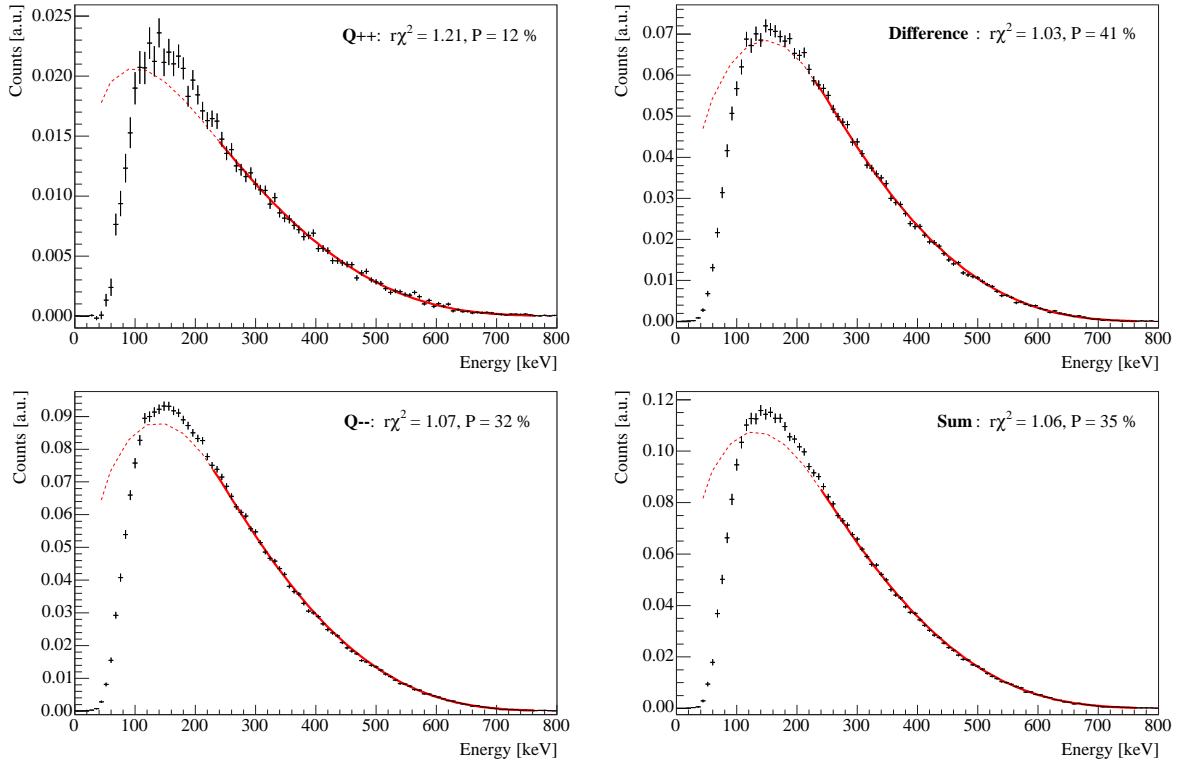Differences in the conversion from channels to energies exhibit the slight difference in the detector calibration.

Figure 4.46: The spectra Q^{++} (top left) and Q^{--} (bottom left) of detector 2 for the asymmetry B_{same}. Difference (top) and sum (below) are shown on the right side; all spectra can be well described in large fit regions from $230-760$ keV; a displacement $\Delta = 0.11$ mm was used for the fits. Please note that the only free parameter in all these fits is a normalizing factor. No trigger function is considered, thus the fits cannot describe the low energetic part of the spectra.
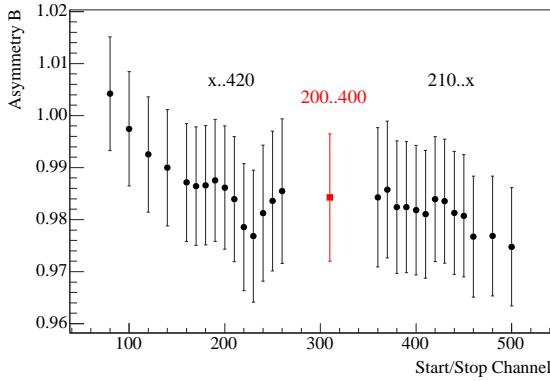

Figure 4.47: Check of the fit region to extract B_{same} from detector 1: On the left, the region starts according to the value on the axis and stops at channel 420; on the right the start channel is fixed to 210. A fit region from channel $200-400$ corresponding to $245-455$ keV is used.
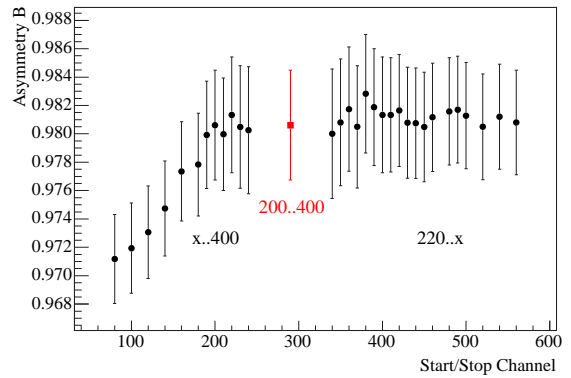
Figure 4.48: Fit region as a function of channels to extract B_{same} from detector 2: We use a fit region of channels $200-400$ corresponding to $250-455$ keV. The error bars indicate the statistical uncertainty of the fit which is much smaller for the second detector.
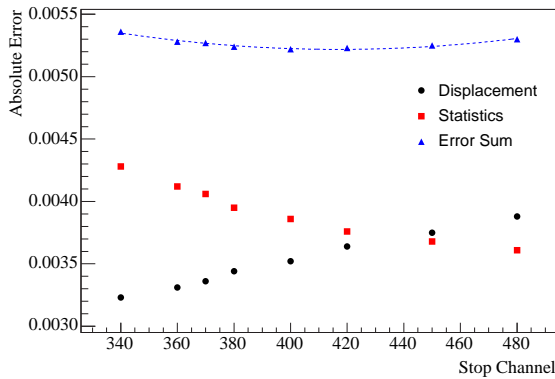
Figure 4.49: With increasing upper border of the asymmetry fit region, the statistical uncertainty gets smaller. At the same time the influence of the imprecisely known displacement between neutron beam and magnetic field grows, since the magnetic mirror correction increases with energy. The plot shows both errors and the error sum for detector 2; fit region starts at channel 200. The minimum of the combined error is at channel 400.
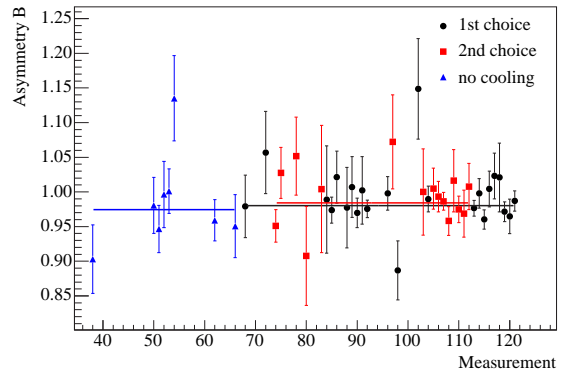
Figure 4.50: Results from B_{same}-fits of the individual measurements of detector 2. They are divided into three groups according to the status of the experimental environment (high voltage stability etc.) during the time the measurement was performed. There is no difference in the mean value of the three groups, and no trend is visible. The errors are only statistical, whereas all corrections already have been applied.

Effects of Drifts and Calibration: B_{same} is almost independent from energy calibration and thus not influenced by gain drifts. This is shown in figure 4.50 where all B-values of detector 2 are presented. The size of the statistical errors varies since measuring time differed from 30 minutes to 15 hours. We have divided them in three groups according to the experimental circumstances they were measured in (e.g. high voltage background, trigger thresholds, etc.): "First choice" indicates measurements with very stable conditions, "second choice" measurements were performed with a less perfect setup, and "no cooling" denotes the early measurements without external cooling where the gain was quite unstable. The three groups coincide perfectly, and no trend is visible. Data can be described better with a constant than a straight line; the gradient of the latter is equal to zero within the errors.

Correction and Errors: We obtain the size of corrections and errors directly from a fit of the B_{same} spectrum that contains all data, by including the respective correction or not, or by varying the constants within their errors. The largest systematic uncertainty is due to the imperfect knowledge of the displacement Δ between neutron beam and magnetic field.

The errors of the systematical corrections (0.05 %) are conservative estimations based on the Monte Carlo results, taking into account the uncertainty of the magnetic field parametrisation [Rav95]. In a cross-check, the correction functions were varied by 5 %, resulting in asymmetry shifts smaller than 0.05 % for all corrections. We expect the description of the effects to be much better, since some of them have been determined independently with two simulations, and the results agree better than 0.5 %. However, since these errors do not limit the measurement, they can be overestimated without consequences to be on the safe side. The influence of the theoretical corrections, i.e. Coulomb, recoil, and outer radiative correction, can be completely neglected here.
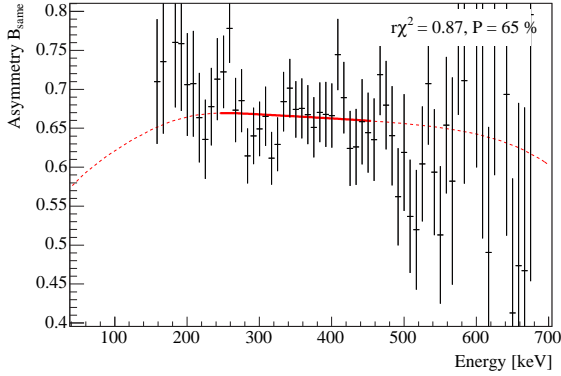
Figure 4.51: Fit of the asymmetry B_{same} to the combined data of detector 1. Low energies cannot be described by the fit due to the high voltage background.
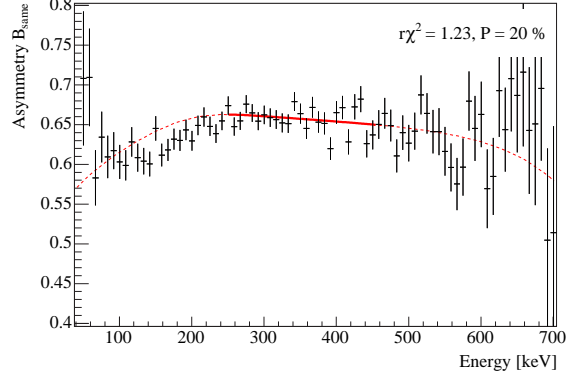
Figure 4.52: Fit of B_{same} to all detector 2 data. The statistical uncertainties are much smaller for this detector; the figures are drawn with the same scale. The solid curve indicates the fit region.

	Detector 1		Detector 2	
Fit Region [keV]	245-455		250-455	
Effect	Corr. [%]	Err. [%]	Corr. [%]	Err. [%]
Polarization				
Polarization	+0.3	0.1	+0.3	0.1
Flip Efficiency		0.1		0.1
Data Set				
Statistics		1.22		0.36
Proton Window	−0.05	0.03	−0.05	0.03
1 Stop Condition	−0.24	0.06	−0.13	0.03
Detector Function				
Gain		0.01		0.01
Offset		0.02		0.02
Resolution		0.00		0.00
Systematic Effects				
Edge Effect	−0.16	0.05	−0.16	0.05
Mirror Effect				
Correction	+0.44	0.05	+0.44	0.05
Displacement	−0.10	0.32	+0.10	0.32
Grid Effect	+0.03	0.05	+0.03	0.05
Correlation Coefficients				
A		0.03		0.03
a		0.06		0.06
Sum	+0.22	1.28	+0.53	0.52

Table 4.2: Correction and errors of the neutrino asymmetry B obtained from events where electron and proton were emitted in the same hemisphere.

4.6.3   Result

Figures 4.51 and 4.52 show the asymmetry B_{same} for the two detectors, generated from all usable measurements. One can clearly see that the statistical significance of detector 2 is superior. A detailed summary of all corrections and uncertainties can be found in table 4.2. It emphazises the smallness of the neccessary corrections allowing systematically very clean measurements. The influence of the accidental coincidences on the error is not stated separately; it is included in the statistical error, where it contributes to approximately 10 %.

The neutrino asymmetry results are

$$B_{\text{Det1}} \;=\; 0.9845(126) = 0.9845(120)_{\text{stat}}(36)_{\text{syst}} \tag{4.43}$$
$$B_{\text{Det2}} \;=\; 0.9798(51)\; = 0.9798(36)_{\text{stat}}(36)_{\text{syst}} \tag{4.44}$$

for detector 1 and detector 2 respectively. Both values agree very well. Since most systematic errors are correlated, only the statistical uncertainties can be averaged to obtain the final result for the same hemisphere measurement:

$$B_{\text{same}} = 0.9802(50) = 0.9802(34)_{\text{stat}}(36)_{\text{syst}}. \tag{4.45}$$

4.7   Neutrino Asymmetry B – Opposite Hemispheres

We will now focus on the analysis of the neutrino asymmetry B_{opp} generated from events with electron and proton emitted in opposite hemispheres. The majority of all events belongs to this group (78 %), however, the statistical sensitivity is quite low. Additionally, it strongly depends on detector calibration.

4.7.1   Analysis and Result

Once again, we have big differences between both detectors regarding the number of measurements that can be used for analysis: Much more data is available when the electron is detected in detector 1 and the proton in detector 2 (we call this B_{opp} measured in detector 1) than in the other case, again due to high voltage instabilities and the different proton efficiencies. We use a rejection threshold of 10 σ corresponding to nearly all cycles, only extreme mavericks are not considered.

Fit Region: Both asymmetries have rather large statistical errors, and the individual points of the measured spectra are widely spread. Because of this, the B values are shifted considerably when the fit region is only changed a bit, however, the shifts are maximally in the order of 0.5 statistical standard deviations – the overall error including systematics is much larger. We therefore use the same approach as for the same hemispheres, and require that all four spectra used to generate the asymmetry must be well described in the asymmetry fit region. For detector 1, this is shown in figure 4.53, the resulting regions are:

	Detector 1	Detector 2
Fit Region [keV]	260−610	200−550

Due to the last requirement, the fit regions differ by 60 keV, however, both of them are chosen high enough to be not affected by background and unrecognized backscattering effects.

Detector Drifts: We divide the 30 measurements used for detector 1 into three subgroups according to their measurement conditions: (Please note that these do not coincide with the groups introduced for B_{same}.)

1. Partly different detector settings, e.g. some photomultipliers have higher discriminator thresholds etc.

2. Different high voltages applied to the foils (maximal difference $\Delta U = 2$ kV).

3. "Good" measurements with stable conditions on detector 1.

The groups have almost the same statistical weight and the asymmetries obtained from each subset can be averaged: For detector 1, they show excellent agreement, whereas there is an obvious drift to lower values in the case of detector 2: Despite of the large errors the three asymmetries are not consistent. Therefore, we have to restrict analysis to the "good" measurements of group 3, with the best background conditions on the proton detector. Of course, this limits statistics dramatically.
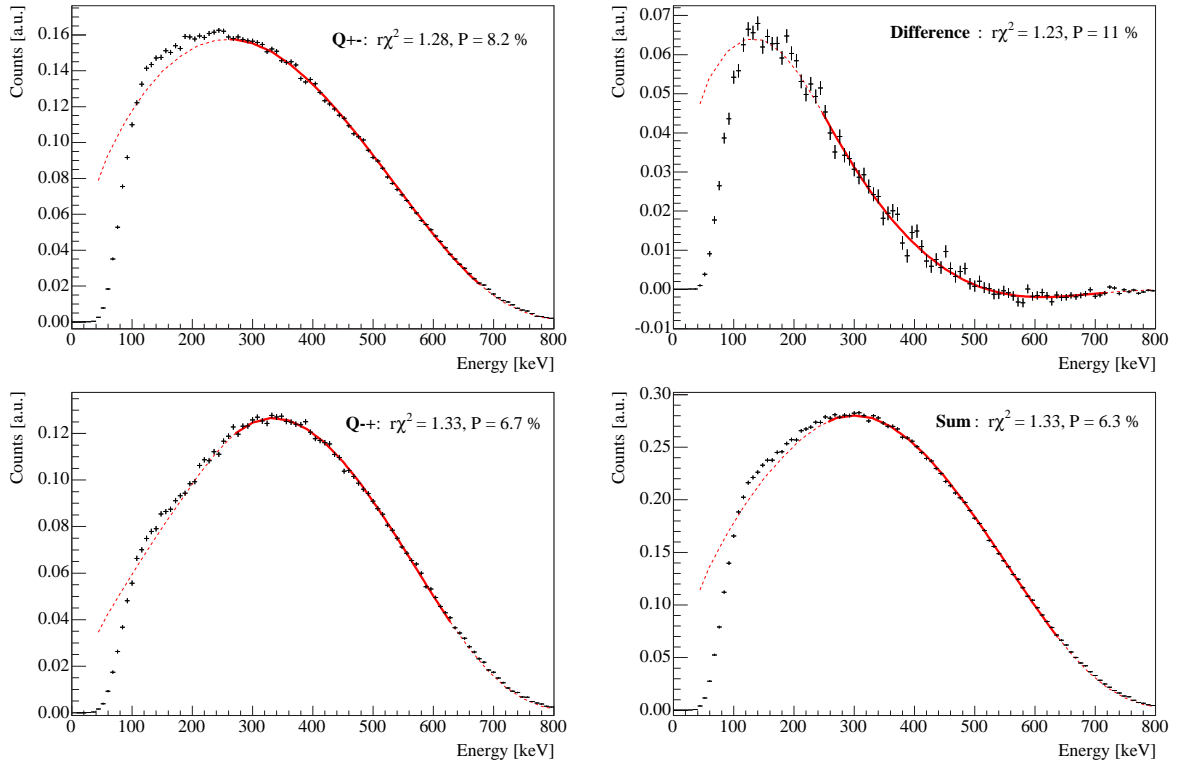

Figure 4.53: The spectra Q^{+-} (top left) and Q^{-+} (bottom left) for the asymmetry B_{opp} in opposite hemispheres; the electron was observed in detector 1. Difference (top) and sum (bottom) are shown on the right hand side; all spectra can be well described within the fit region of $260-610$ keV and larger. Please note that the only free parameter in all these fits is a normalizing factor. No trigger function is considered, thus the fits cannot describe the low energetic part of the spectra.
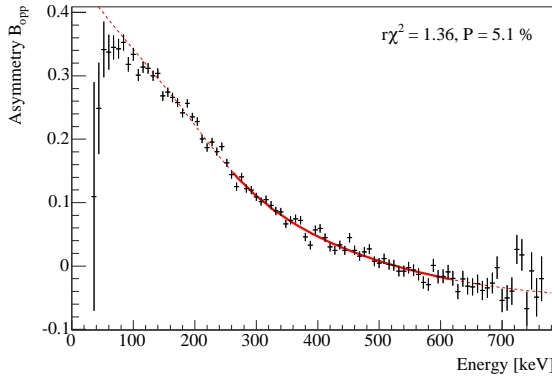
Figure 4.54: Fit of the neutrino asymmetry B_{opp} to all data of detector 1, i.e. the electron was observed in detector 1 the proton in the "good" proton detector 2.
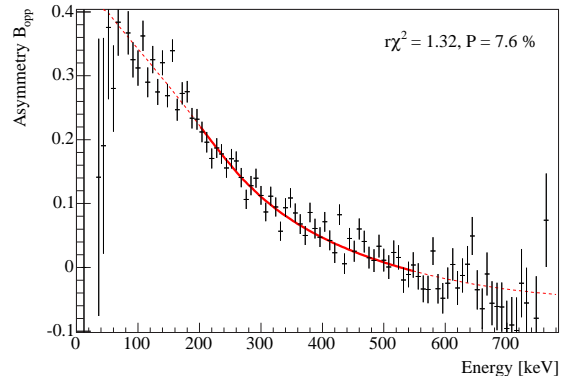
Figure 4.55: Fit of the B_{opp} to all data used for the detector 2 analysis. The error bars are larger compared to detector 1 since less measurement could be considered.

Effects of Detector Calibration: Energy calibration is the most important error contribution for B_{opp}. Especially the energy offset E_{off} of the energy-channel relation is only known very poorly, and therefore constitutes the largest uncertainty of the measurement. The exact determination of the gain is also essential, only the effects of the energy resolution are small.

Now, we generate the asymmetry specta and obtain the asymmetries B from the fits (cf. figures 4.54, 4.55). After application of all relevant corrections we get:

$$B_{\mathrm{Det1}} = 1.017(17) \tag{4.46}$$
$$B_{\mathrm{Det2}} = 1.029(31). \tag{4.47}$$

The detailed error analysis is presented in table 4.3. At a first glance, the high values are quite astonishing, since asymmetries greater than unity would imply that more than 100 % of particles are emitted into one hemisphere, what is obviously not possible. However, if we consider the full uncertainty, statistical and systematical, we find that the asymmetries for detector 1 and detector 2 differ from the Particle Data Group value only by 1.9 σ and 1.4 σ respectively. Deviations of this size are too small to be taken seriously.

However, since both asymmetries are shifted in the same direction, we may have a systematic effect in the detector calibration that changes the energy offset to higher values. An offset E_{off} lowered by just $2-3$ σ would allow to describe the B_{opp} spectrum with the Standard Model B value. A possible explanation for this could be the additional γ-radiation emitted from the calibration sources. In measurements of the electron asymmetry A performed with PERKEO II, the γ-contribution was determined in a procedure including calibration C and background X measurements with ($_B$) and without ($_0$) magnetic field. Combining these spectra in the following way ("4-difference") [Mue96],

$$S_4 = C_B - X_B - C_0 + X_0, \tag{4.48}$$

yields the pure electron spectrum if the detector gain is independent of the magnetic field (cf. e.g. [Bae96]). Unfortunately, this condition cannot be fulfilled when the photomultiplier tubes are installed as for the B-measurement, since the detector gain differs significantly

Effect	Detector 1		Detector 2	
Fit Region [keV]	260-610		200-550	
	Corr. [%]	Err. [%]	Corr. [%]	Err. [%]
Polarization				
Polarization	+0.16	0.06	+0.20	0.07
Flip Efficiency		0.07		0.06
Data Set				
Statistics		0.93		1.63
Proton Window	−0.16	0.08	−0.16	0.08
1 Stop Condition	−0.67	0.03	−0.62	0.09
Detector Function				
Gain		0.50		0.91
Offset		1.13		2.29
Resolution		0.05		0.01
Systematic Effects				
Edge Effect	+0.72	0.05	+0.32	0.05
Mirror Effect				
Correction	−0.02	0.05	−0.01	0.05
Displacement	−0.02	0.02	−0.01	0.01
Grid Effect	−0.85	0.05	−0.74	0.05
Correlation Coefficients				
Theory Corrections	−0.02		−0.02	
A		0.47		0.35
a		0.01		0.01
Sum	−0.86	1.62	−1.04	2.98

Table 4.3: Correction and errors of the neutrino asymmetry B obtained from events with electron and proton measured in opposite hemispheres.

for measurements with and without magnetic field. This prevents to exploit the 4-difference method which relys on constant signal amplification, and we have to get by with the additional γ-radiation in the calibration spectra.

Analysis of calibration data obtained in an electron asymmetry setup [Sch04, Mun06] indicates indeed that the energy offset is shifted to lower values when the spectra S_4 are used for calibration, resulting in a smaller B_{opp}. For the other asymmetries, B_{same} and C, the exact knowledge of the energy channel relation is much less important, therefore a "simple" calibration using only measurements with magnetic field is completely sufficient.

Final Result: When one looks at the detailed summary of all corrections and errors, table 4.3, it is obvious that a determination of B in opposite hemispheres cannot be regarded as a precision measurement. Therefore we do not average these values with the same hemisphere results, but rather consider them as cross checks.

For detector 1, the final result for the asymmetry in opposite hemispheres is

$$B_{\text{Det1}} = 1.017(17) = 1.017(10)_{\text{stat}}(14)_{\text{syst}}, \tag{4.49}$$

and for detector 2 we obtain

$$B_{\text{Det2}} = 1.029(31) = 1.029(17)_{\text{stat}}(26)_{\text{syst}}. \tag{4.50}$$

Both values show statistical agreement with the world average, the χ^2 probabilities are P=5 % and P=14 % for detector 1 and 2 respectively.

4.7.2 Systematic Checks

Although the results are statistically compatible with the expecations, we performed tests with measured data and with Monte Carlo simulations to check if something went wrong or if the result could be caused by unknown systematical effects, since both B_{opp} values are shifted to rather high values.

All checks and simulations that will be presented below indicate that the high asymmetry values are neither caused by wrong considerations in the generation of the spectra nor by cuts into angular or time-of-flight distribution of the particles. The results (4.49) and (4.49) are correct. Nevertheless, we will present the checks in some detail, since they give interesting insights into the analysis of the opposite hemisphere asymmetry.

4.7.2.1 Checks with Data

These systematic test were performed with real data, we changed conditions, cuts, and corrections to study their influence on the result. An error in the implementation of the fit functions can be excluded since they were verified with Monte Carlo data. Besides other basic tests, we investigated the following:

- If we generate the asymmetry from 10 σ data with background subtraction, but ignore the contribution from accidental coincidences, we get a reasonable B_{opp} value below unity. The sum spectrum, however, cannot be described by a fit. Only the restriction of the stop to the coincidence window (40 μs) and the correct subtraction of accidental coincidences leads to a realistic sum spectrum; but then the asymmetry is increased to values above unity again.

- Regarding more than one stop in the time windows has almost no effect, besides that now the spectra Q^{+-}, Q^{-+}, D, and S cannot be described with statistically acceptable fit probabilities due to increased background.

- The asymmetry cannot be shifted to lower values by changing timing conditions: Neither reducing the backscattering window[16], nor the limitation of the coincidence window has a considerable effect. The same holds when the start of the coincidence window is shifted to smaller times.

---

[16]When a stop occurs in the backscattering window $(0-200$ ns$)$ it is regarded as backscattered electron and not as a decay proton. However, we do not expect a proton in the backscattering window due its much larger drift times.

- We did not find anything unusual in the energy spectrum of the stop signals. However, as already mentioned in chapter 4.2, the spectrum of the background signals is very similar to the proton stops.

- When we exclude backscattering events from the data, we obtain an asymmetry $B_{\mathrm{opp}} \approx 1$. Analysis of the spectra generated from backscattering data only yields a very high asymmetry $B_{\mathrm{BS}} \approx 1.4$, the sum spectrum S can be well described, what is not the case for the difference D.

  However, the high value for the backscattering data is due to a cut in the angular distribution of the particles, what will be explained in the following section.

To summarize, we can state that no systematic errors have been made in the generation of the spectra.

4.7.2.2 Monte Carlo Simulations

Additionally, we studied the neutrino asymmetry B_{opp} with Monte Carlo (MC) simulations. All fits to simulated spectra were performed using the same fit region as for the real data (detector 1).

Cuts in the angular Distribution: When electrons of particular incident angles on the detector have smaller trigger probabilities than others, i.e. if there are cuts in the angular distribution, we expect changes in the asymmetries. Figure 4.56 shows the distribution of the angle between neutron spin and electron momentum. This corresponds to the incident angle on the detector, since the spin is aligned perpendicular to the detectors: Initially, all angles from 0 to π appear, however, the decreasing magnetic field turns the momenta in forward direction to steeper angles.

We tried different cut conditions on the angular distribution to reproduce the observed situation for the asymmetries: B_{same} according to the Standard Model prediction and B_{opp} larger than unity. This is only fulfilled by a cut at steep angles ($\theta \approx 0, \pi$), where the electron spectrum can still be described by a Fermi function.
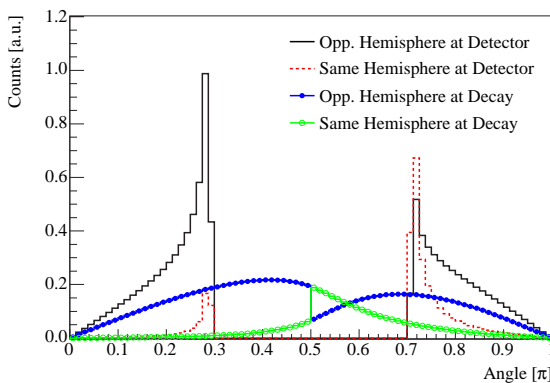

Figure 4.56: Distribution of the angle between neutron spin $\mathbf{s}$ and electron momentum $\mathbf{p}_e$ obtained from a Monte Carlo Simulation. An angle of 0 indicates $\mathbf{p}_e$ parallel to $\mathbf{s}$, π is the anti-parallel case. The smooth distributions generated in the decay get shifted to steeper angles of incidence at the detectors due to the momentum turn in the decreasing magnetic field. The flattest angles at the detectors are 0.29 π and 0.71 π, where the distributions almost show their maximum. Obviously, the opposite hemisphere events hit the detectors much more often at steep incident angles.

However, this scenario cannot be motivated physically: The detection efficiency is maximal at incident angles close to the normal since backscattering effect are vanishing [Mar03], therefore we have to reject this cut as explanation for the high asymmetries. Instead it is most likely the reason for the extremely high asymmetry value of the backscattered events alone, since the steep angles are missing in this data set.

Another argument against angular cuts is the spectral shape of the observed asymmetry B_{opp}. It shows no distortion within the statistical errors, whereas we expect that changes in the angular distribution would alter the energy dependence.

Stops generated by Background events: A second simulation was used to examine the influence of background events: With probability P, the electron energy of a simulated event was replaced by a background signal, that was randomly obtained from a spectrum measured without coincidence condition. Again, this leaves B_{same} unaffected and leads to high values for B_{opp}. At the same time, however, the resulting spectra get strongly distorted at low energies what is not the observed case, and we would need rather high probabilities $P = 15\%$ to reconstruct $B_{\mathrm{opp}} \approx 1.015$. This is much too high for the almost background free events in opposite hemispheres.

Events where a background stop occurs before the proton arrives represent cuts in the time-of-flight spectrum and lead to increased B_{opp} values. This was the situation in the previous experiment [Kre04b], where only one stop per event could be detected. We now have a completely different situation, since we were able to identify many stops: No event with more than one signal in the coincidence window is considered, regardless if the "false" stop occurred before or after the proton signal. Hence we do not cut into the TOF-spectrum.

Summary: We performed Monte Carlo simulations to reproduce the observations, and actually found some scenarios that yield an increased asymmetry in opposite hemispheres. However, these are not sufficient to describe the results since all bring up physical objections.

4.7.2.3   Analysis via Proton Asymmetry

The last systematical test performed involves the proton asymmetry introduced in chapter 2.3.3. From the spectra

$$\rho^{\uparrow} = Q^{++} + Q^{-+} \qquad \text{and} \qquad \rho^{\downarrow} = Q^{--} + Q^{+-}, \tag{4.51}$$

using detector 2 (Q^{++} and Q^{--}, same hemisphere) and detector 1 data (Q^{+-} and Q^{-+}, opposite hemispheres), the experimental proton asymmetry spectrum

$$C_{\mathrm{exp}} = \frac{\rho^{\uparrow} - \rho^{\downarrow}}{\rho^{\uparrow} + \rho^{\downarrow}} \tag{4.52}$$

can be constructed. Since the Q-spectra depend on B, a fit to C_{exp} can be also used to obtain the neutrino asymmetry, that we will denote B_p in this case (cf. figure 4.57).

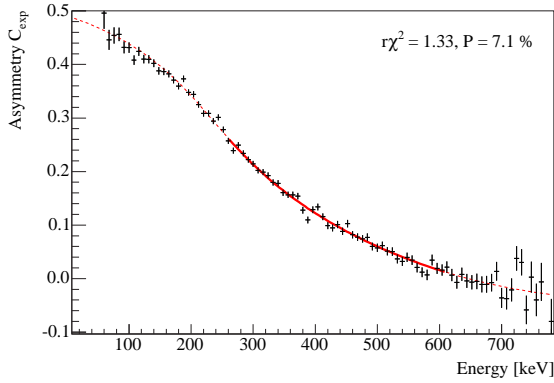When we use the usual fit region of $260-610$ keV, we get

$$B_p = 0.981(15), \tag{4.53}$$

Figure 4.57: Fit of the neutrino asymmetry B_p to the experimental proton asymmetry spectrum C_{exp}. Although it is mainly generated from the Q^{+-} and Q^{-+} spectra, one yields a reasonable asymmetry that is below unity. However, it is not possible to give a detailed error analysis for this case, since C_{exp} consists of data of both detectors and the detector functions get mixed.

where the error is estimated using only the dominating factors statistics, gain, and energy offset. A detailed error analysis would be quite difficult, since contributions of both detectors get mixed in C_{exp}. The B_p-value is lower than unity, although C_{exp} was constructed mainly from the opposite hemisphere spectra since these are kinematically favoured by 78 %. Possible influences of additional γ-background in the calibration spectra are reduced here, since the spectrum C_{exp} is less steep in the fit region, i.e. less energy dependent, than B_{opp}.

4.8 Proton Asymmetry C

The proton asymmetry C cannot be obtained from a fit to a measured spectrum (not even from a fit to C_{exp}, equation (4.52)), as it is the case for the asymmetries A, B_{same}, and B_{opp}, since there is no theoretical description of neutron decay based on C. However, the four Q^{ij}-spectra contain the information in which hemisphere the proton was emitted, and we can determine C by integrating these spectra:

$$C = \frac{\int \rho^\uparrow(E)\mathrm{d}E - \int \rho^\downarrow(E)\mathrm{d}E}{\int \rho^\uparrow(E)\mathrm{d}E + \int \rho^\downarrow(E)\mathrm{d}E}, \tag{4.54}$$

where $\rho^\uparrow$ and $\rho^\downarrow$ are defined as

$$\rho^\uparrow(E) = Q^{++}(E) + Q^{-+}(E) \tag{4.55}$$
$$\rho^\downarrow(E) = Q^{--}(E) + Q^{+-}(E). \tag{4.56}$$

Since low and high energy range of the spectra cannot be measured with a reasonable precision we have to get the area below the Q-functions from a fit at medium energies, and extrapolate to the whole spectrum before integration. When we want to evaluate C in a particular detector (what is important to be independent of the proton efficiency), we have to consider (electron) Q-spectra from different detectors. In case of the "good" proton detector 2, Q^{++} and Q^{--} are measured in detector 2, Q^{+-} and Q^{-+} in detector 1. Only this combination allows to determine a precise C-value.

4.8.1 Analysis

We use the same data as in the analysis of the neutrino asymmetries: 2 σ is the rejection threshold for the same hemisphere spectra, 10 σ for the opposite case. Background and
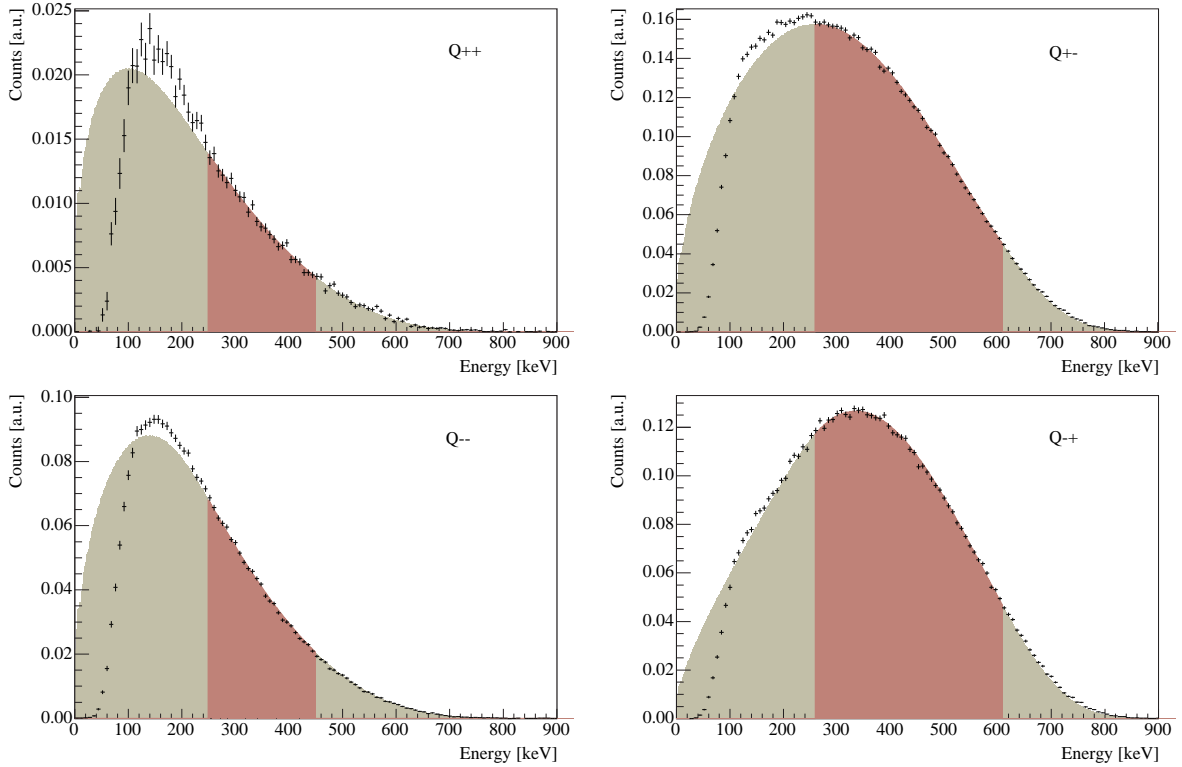
Figure 4.58: Determination of the proton asymmetry C for proton detector 2: The same hemisphere electron spectra Q^{++} (top left) and Q^{--} (bottom left) of detector 2 are fitted in the usual fit region indicated in the plots. Then the functions are extrapolated to cover the whole energy range and finally integrated. The figures on the right show Q^{+-} (top) and Q^{-+} of detector 1. Using the integrals, one can calculate the asymmetry C.

accidental coincidences are subtracted as usual, and only 1-stop events are considered. Additionally, we reuse the fit regions $250-455$ keV and $260-610$ keV for same and opposite data respectively. This is reasonable, since the effects limiting the result also stay the same: At low energies, the spectra are affected by unrecognized backscattering and high-voltage background, at high energies, the influence of mirror- and edge-effect becomes large.

Extrapolation: After summing up all data and scaling the Q-spectra to equal measuring times, we perform fits with the corresponding theoretical Q-function in the regions given above. Please note that we have again only one free fit parameter, a normalizing factor N. All other input values are taken from calibration measurements. Now, the fit-functions are extrapolated to higher and lower energies and integrated. Since we have to consider the energy resolution of the detectors, we integrate from $0-850$ keV, i.e. beyond the theoretical maximum electron energy of $E_0 = 781.6$ keV. A further extension to 900 keV yields changes in the order of 0.01 % and is completely negligible. The fits and extrapolations for proton detector 2 are shown in figure 4.58.

Corrections and Uncertainties: The size of errors and corrections is obtained by variation of the respective parameters in fits of all four spectra, followed by extrapolation and

integration. The statistical error is determined by changing the normalizing factor N to $N + \Delta N$, where ΔN is its statistical uncertainty from a "normal" fit. Now this function is evaluated; the deviation from the fit above is the uncertainty due to statistics.

It is the characteristic feature of this analysis method that we have to extrapolate considerably to energies, where no precise information on the asymmetry is accessible experimentally. However, we do not give an individual error on the extrapolation since it is already included in the uncertainties of statistics, gain, and energy offset: These change the spectral shape in the fit region resulting in different fits, extrapolations, and integrals.

Alternative Analysis: Instead of fitting and extrapolating the four Q-functions as demonstrated above, one could also think of using the spectra $\rho^\uparrow$ and $\rho^\downarrow$ directly (cf. figure 2.15, page 23). We do not follow this approach, since each of the two consists of data from both detectors, what makes error analysis very difficult because detector calibrations get mixed. Q- and ρ-spectra consist of exactly the same data, therefore the asymmetry itself should be the same.

4.8.2 Result

The final result for the proton asymmetry C,

$$C_{\text{Det2}} = -0.2377(36), \qquad (4.57)$$

is limited by the calibration of the electron detectors, its influence is comparable to the B_{opp} analysis. Especially the value of the energy offset E_{off} should be known much more precisely. This shows that we cannot get to much more precise C-values using this setup without significant improvements on detector calibration. A detailed summary of all errors and uncertainties can be found in table 4.4.

When we determine C from the inferior proton detector 1 we obtain

$$C_{\text{Det1}} = -0.245(12). \qquad (4.58)$$

The error of 4.8 % is only estimated, using the dominating factors statistics, gain, and energy loss. Both values, C_{Det2} and C_{Det1}, agree very well, however, due to the large systematic uncertainties of the latter we will only use it as cross check and do not average the results.

Effect	Corr [%]	Err [%]
Polarization		
Polarization	+0.30	0.10
Fip Efficiency		0.10
Data Set		
Statistics		0.44
Extrapolation	−47.37	
Proton Window	0.03	0.01
1 Stop Condition	−0.84	0.15
Detector Function		
Gain		0.38
Offset		1.36
Resolution		0.12
Systematic Effects		
Edge Effect	−0.26	0.05
Mirror Effect		
Correction	−0.02	0.05
Displacement	0.02	0.03
Grid Effect	−0.08	0.05
Correlation Coefficients		
Theory Corrections	−0.46	
A		0.01
B		0.07
a		0.02
Sum	−48.68	1.50

Table 4.4: Correction and errors of the proton asymmetry C. The extrapolation uncertainty contributes to the statistical and detector calibration errors.

Chapter 5

Results and Standard Model Tests

Having obtained values, corrections, and uncertainties of the neutrino asymmetry B and the proton asymmetry C in the preceding chapter, we will now compare the results to previous measurements and expectations, and will calculate new world mean values. At last, we want to examine the implications of the newly measured correlation coefficients on searches for "Physics beyond the Standard Model".

5.1 Final Results

The final neutrino asymmetry result of the PERKEO IIB measurements is

$$\text{Neutrino Asymmetry} \quad B = 0.9802(50). \tag{5.1}$$

Corrections to this value are below 1 %, details on the uncertainty of altogether 0.51 % can be found in table 4.2. Additionally, we performed the first precise measurement of the proton asymmetry at all:

$$\text{Proton Asymmetry} \quad C = -0.2377(36). \tag{5.2}$$

The neccessary extrapolation corrections are quite large, however, a total error of 1.5 %, dominated by the uncertainty of detector calibration, is a very good result.

5.2 Neutrino Asymmetry and right-handed Currents

Figure 5.1 shows all measurements of the neutrino asymmetry that have been done so far and includes our new result. Although we almost had to fully abandon the second detector, resulting in a 50 % loss in statistics and a large systematical uncertainty (displacement Δ), it has almost the same precision as the last measurement by Serebrov et al. [Ser98], $B_{1998} = 0.9801(46)$. We were even able to perform an experiment with considerably smaller systematical corrections, as our result had to be corrected by 0.53 % only (1.21 % if the absolute values of all contributions are added up), compared to at least[1] 3.5 % correction for the measurement of 1998.

---

[1] This is only the correction due to polarization and spinflipper efficiency, the size of all other contributions (solid angle determination with Monte Carlo simultions, etc.) is not given in the publication.
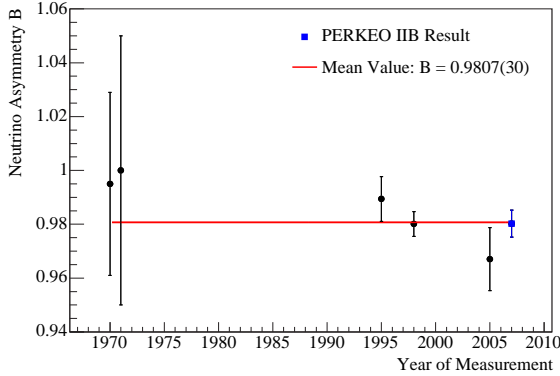
Figure 5.1: The figure compares the new neutrino asymmetry B (2007) with the results from earlier experiments [PDG06]. All values agree very well ($r\chi^2$=0.56, P=73%), and our result confirms the old world average. The uncertainty of the new average $B_{\mathrm{mean}} = 0.9807(30)$ is reduced by 25 %.

All other previous measurements are confirmed as well. In particular, we also agree with the preceding PERKEO II measurement (2005, [Kre04b]), however, we managed to reduce the overall uncertainty by a factor of 2.4.

The calculation of a new world average, including all six results given in figure 5.1, yields

$$B_{\mathrm{mean}} = 0.9807(30). \tag{5.3}$$

Compared to the last mean value, $B_{2006} = 0.981(4)$, published by the Particle Data Group (PDG) [PDG06], the uncertainty is reduced by 25 %.

Right-handed Currents: The main motivation for measuring the neutrino asymmetry is its sensitivity to the neutrino helicity and therefore to possible right-handed contributions to the weak interaction. In the exclusion plots presented below, we exploit equations (2.73)$-$(2.76) to get limits on the mixing angle ζ and $\delta = \frac{m_1^2}{m_2^2}$, the mass ratio of the bosons W_1, W_2 (cf. section 2.3.5). However, since the $e\nu$-correlation a is only known with a precision of 4 %, we will only include the correlation coefficients A and B, and the lifetime τ_n in the analysis. In the year 2004, when we started this thesis, the status regarding right-handed admixtures was as shown in figure 2.4 (page 15).

In the last years, neutron lifetime measurements have achieved higher and higher precision: The current world mean value given by the PDG [PDG06], $\tau_{\mathrm{PDG}} = 885.7(8)$ s, is dominated by the measurement of Arzumanov et al. [Arz00], that has an absolute uncertainty of 1.0 seconds. However, in 2005, Serebrov et al. [Ser05] published the lifetime $\tau_{\mathrm{Ser}} = 878.5(8)$ s, which differs by 6.5 standard deviations σ from τ_{PDG} and by 5.6 σ from Arzumanov's result. Obviously, averaging these values is not reasonable, and we face the situation that we have to deal with two different neutron lifetimes at the moment. Therefore, we calculate constraints on left-right symmetry for both values.

Besides the two lifetimes given above, we use the following input values: The new neutrino asymmetry average $B_{\mathrm{mean}} = 0.9807(30)$, the Particle Data Group value for the electron asymmetry $A_{\mathrm{PDG}} = -0.1173(13)$, and the average of all A-values measured with PERKEO II $A_{\mathrm{PII}} = -0.1193(4)$. Here, the latest experiment [Mun06] is not published yet. The precision of the combined PERKEO II measurements is significantly higher than the PDG value, since the error of the latter is scaled with a factor 2.3 to include older measurements. However, these had to be corrected by 15$-$29 %, where the corrections of the three PERKEO II values only range from 3.9$-$0.4 %.
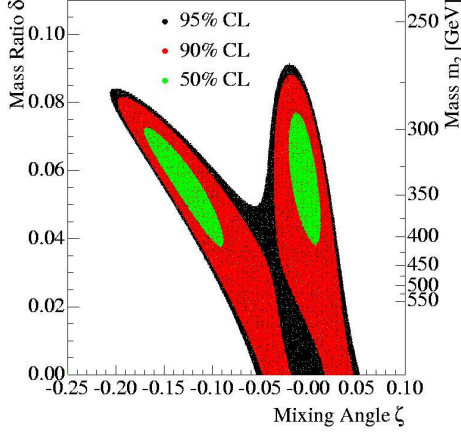
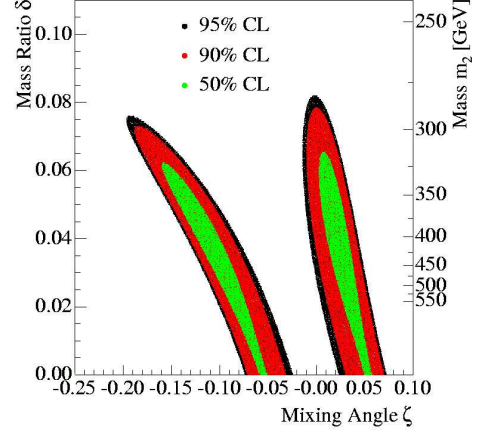Figure 5.2: Exclusion plot on admixtures of right-handed currents generated with the input values A_{PDG}, B_{mean}, and τ_{PDG}.

Figure 5.3: This exclusion plot employs the parameters A_{PDG}, B_{mean}, and the neutron lifetime from the Serebrov measurement (2005): τ_{Ser}.
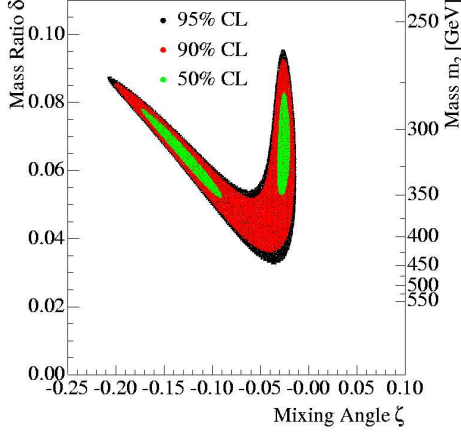

Figure 5.4: Input: A_{PII}, B_{mean}, τ_{PDG}.
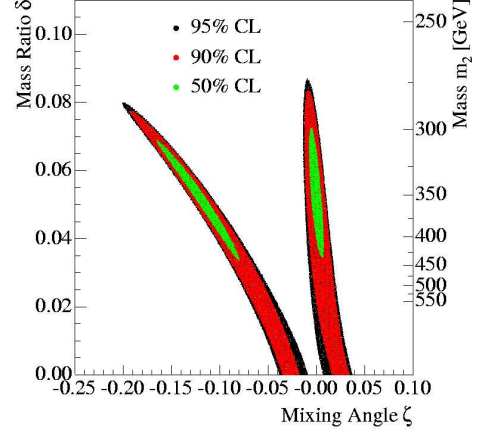
Figure 5.5: Input: A_{PII}, B_{mean}, τ_{Ser}.

The exclusion plots 5.2−5.5 were generated by calculating

$$\chi^2 = \left(\frac{A(\lambda', \zeta, \delta) - A_{\mathrm{exp}}}{\mathrm{d}A_{\mathrm{exp}}} \right)^2 + \left(\frac{B(\lambda', \zeta, \delta) - B_{\mathrm{exp}}}{\mathrm{d}B_{\mathrm{exp}}} \right)^2 + \left(\frac{\tau(\lambda', \zeta, \delta) - \tau_{\mathrm{exp}}}{\mathrm{d}\tau_{\mathrm{exp}}} \right)^2 \qquad (5.4)$$

for every point λ', ζ, and δ. It is the quadratic deviation of the coefficient $X(\lambda', \zeta, \delta)$ computed in the left-right symmetric model from the experimental input X_{exp}. $\mathrm{d}X_{\mathrm{exp}}$ is the experimental uncertainty. $\chi^2 < 1.39$ defines the 50 %, $\chi^2 < 4.61$ the 90 %, and $\chi^2 < 5.99$ the 95 % confidence level (CL). The resulting three-dimensional contours are mapped along the λ'-axis onto the $\zeta\delta$-plane to generate the two-dimensional exlusion plots.

In the following, we present the global χ^2 minimum $(\lambda'_{\mathrm{min}}, \zeta_{\mathrm{min}}, \delta_{\mathrm{min}})$, and limits on λ', ζ, and δ – corresponding to a constraint on the mass m_2 – for the different parameter sets considered. Additionally, we give $\delta(0)$ for a mixing angle $\zeta = 0$:

1. $\boldsymbol{A}_{\mathrm{PDG}}$, $\boldsymbol{B}_{\mathrm{mean}}$, $\boldsymbol{\tau}_{\mathrm{PDG}}$ (figure 5.2): If one compares this plot with figure 2.4 that uses the same A and τ_n inputs, one can clearly see the sensitivity of the neutrino asymmetry B

on right-handed contributions. Taking into account the new value does not yield much improved limits for ζ and δ,

$$\lambda'_{\min} = -1.2711 \qquad 90\% \text{ CL: } -1.3077 < \lambda' < -1.2678$$
$$\zeta_{\min} = -0.0046 \qquad 90\% \text{ CL: } -0.1978 < \zeta < 0.04170$$
$$\delta_{\min} = 0.061 \qquad 90\% \text{ CL: } \quad \delta < 0.088 \; \Rightarrow \; m_2 > 271 \text{ GeV,}$$
$$90\% \text{ CL: } \delta(0) < 0.080 \; \Rightarrow \; m_2 > 284 \text{ GeV,}$$

but now, the Standard Model prediction $\zeta = \delta = 0$ is not included in the 90 % confidence level contour anymore.

2. $\boldsymbol{A}_{\text{PDG}}$, $\boldsymbol{B}_{\text{mean}}$, $\boldsymbol{\tau}_{\text{Ser}}$ (figure 5.3): With the lower lifetime given by Serebrov, the input parameter set is not compatible with the Standard Model anymore. The constraints are:

$$\lambda'_{\min} = -1.2897 \qquad 90\% \text{ CL: } -1.3092 < \lambda' < -1.2726$$
$$\zeta_{\min} = -0.123 \qquad 90\% \text{ CL: } -0.188 < \zeta_1 < -0.013, \; -0.011 < \zeta_2 < 0.070$$
$$\delta_{\min} = 0.045 \qquad 90\% \text{ CL: } \quad \delta = \delta(0) < 0.079 \; \Rightarrow \; m_2 > 287 \text{ GeV,}$$

3. $\boldsymbol{A}_{\text{PII}}$, $\boldsymbol{B}_{\text{mean}}$, $\boldsymbol{\tau}_{\text{PDG}}$ (figure 5.4): This combination also excludes the Standard Model and predicts an upper mass limit for the right-handed boson W_2. However, this limit has been excluded by other experiments (cf. section 2.2.3 and [Bab06]):

$$\lambda'_{\min} = -1.2915 \qquad 90\% \text{ CL: } -1.3104 < \lambda' < -1.2726$$
$$\zeta_{\min} = -0.136 \qquad 90\% \text{ CL: } -0.2008 < \zeta < -0.0144$$
$$\delta_{\min} = 0.067 \qquad 90\% \text{ CL: } \quad 0.037 < \delta < 0.093$$
$$\Rightarrow \; 264 \text{ GeV} < m_2 < 421 \text{ GeV.}$$

4. $\boldsymbol{A}_{\text{PII}}$, $\boldsymbol{B}_{\text{mean}}$, $\boldsymbol{\tau}_{\text{Ser}}$ (figure 5.5): Combining the lower lifetime with the higher electron asymmetry almost restores the Standard Model at 95 % CL and yields:

$$\lambda'_{\min} = -1.2933 \qquad 90\% \text{ CL: } -1.3119 < \lambda' < -1.2753$$
$$\zeta_{\min} = -0.127 \qquad 90\% \text{ CL: } -0.192 < \zeta_1 < -0.017, \; -0.013 < \zeta_2 < 0.035$$
$$\delta_{\min} = 0.055 \qquad 90\% \text{ CL: } \quad \delta < 0.084 \; \Rightarrow \; m_2 > 278 \text{ GeV,}$$
$$90\% \text{ CL: } \delta(0) < 0.076 \; \Rightarrow \; m_2 > 293 \text{ GeV.}$$

Summary: The existence of two lifetime values and two possibilities for A makes it difficult to give a "final" result. We suggest to use the electron asymmetry A_{PII}, since it only includes the values with corrections smaller than 4 %. However, we do not want to make a decision which is the "correct" lifetime value, and therefore scale the individual errors $\text{d}\tau_i$ such that the values agree statistically[2]. Figure 5.6 shows the current status of right-handed contributions in neutron decay (90 % CL) obtained with A_{PII}, B_{mean}, and $\tau_{\text{mean}} = 882.0(1.4)$ s:

$$\begin{aligned} -1.3113 \; &< \lambda' < \; -1.2735 & \delta < 0.089 \; &\Rightarrow \; m_2 > 271 \text{ GeV} \\ -0.1968 \; &< \zeta < \quad 0.0040 & \delta(0) < 0.062 \; &\Rightarrow \; m_2 > 322 \text{ GeV.} \end{aligned} \qquad (5.5)$$
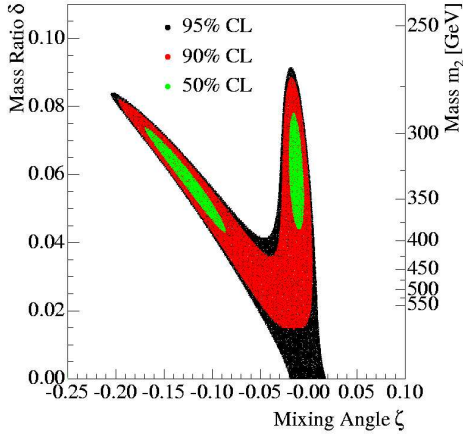
---

[2]The procedure was introduced in section 4.1.2 on page 59.

Figure 5.6: Exclusion plot for the existence of right-handed currents based on the neutron decay parameters A_{PII}, B_{mean}, and $\tau_{\mathrm{mean}} = 882.0(1.4)$ s. The lifetime uncertainty has been scaled by 2.5 to account for the unclear experimental situation when all measurements are considered. The Standard Model prediction $\zeta = \delta = 0$ is included in the 95 % confidence region.

It is interesting to note that the Standard Model is not covered by the 90 % CL contour of any of the studied cases. This shows, that even if the best limits on m_2 will never be reached by analyzing neutron decay data, it still provides a unique opportunity to detect new physics since it is simultaneously sensitive to the mixing angle. However, at the moment we do not consider the deviations to be significant.

5.3   Proton Asymmetry and λ

During the B-beamtime of 2001, the PERKEO II collaboration managed to verify the proton asymmetry with a rather large uncertainty of 4.7 % [Kre04b, Abe05]:

$$C_{2001} = -0.233(11). \tag{5.6}$$

The result from the experiment presented in this thesis, $C = -0.2377(36)$, confirms the previous value but is significantly more precise. With an uncertainty of 1.5 % this constitutes the first precision measurement of the proton asymmetry. Its relative error is even smaller than the error of the electron-neutrino correlation a (3.9 %).

With the world average value of $\lambda = \frac{g_A}{g_V} = -1.2695(29)$ [PDG06] one can calculate an "expected" proton asymmetry using the equation (cf. section 2.3.1)

$$C = x_C \ \frac{4 \ \lambda}{1 + 3\lambda^2}, \tag{5.7}$$

where $x_C = 0.27484$ is a kinematical factor. Our result is in full agreement with the expectation, $C_{\mathrm{PDG}} = 0.2392(4)$. On the other hand, equation (5.7) can also be used to obtain a new λ-value from the proton asymmetry. Our result

$$\lambda_{\mathrm{C}} = -1.282(29) \tag{5.8}$$

is fully consistent with other experiments, but has only a low precision of 2.3 % and is thus not competitive. However, compared to electron asymmetry measurements, the "standard" procedure to get λ, it is a quite interesting method since it employs the different systematics of a coincidence measurement.

Within the Standard Model, A, B, and C are coupled by the relation

$$C = x_C(A + B). \tag{5.9}$$

This can be exploited to test the theory which was impossible so far due to the missing precise proton asymmetry measurement. Now, both sides of the equation agree within the experimental uncertainties,

$$-0.2377(36) = -0.2374(12),$$

if we insert the average values for A and B [PDG06], and the newly measured C. The relation remains true if we replace B by B_{mean}, equation (5.3), or the electron asymmetry by the mean value A_{PII} that only includes PERKEO II results.

5.4   Limits on Scalar and Tensor Interactions

In section 2.1, we have given the most general Lagrangian, equation (2.16), for the weak interaction, including scalar (S), pseudo-scalar (P), vector (V), axial-vector (A), and tensor contributions (T). The existence of the (in general complex) coupling constants g_i, g_i' is related to the partity transformation of the current: Parity invariance holds if one of the constants g_i, g_i' is zero, it is violated if $g_i \neq 0$ and $g_i' \neq 0$. Maximal parity violation – as realized in the Standard Model – corresponds to $|g_i| = |g_i'|$. The pseudo-scalar contributions (g_P, g_P') can be omitted, since one can show that the pseudo-scalar hadronic current $\bar{p}\gamma^5 n$ in equation (2.16) vanishes [Sev06]. Therefore the general description allows altogether eight complex coupling constants, whereas the Standard Model only uses two real ones g_A, g_V (assuming time reversal invariance).

Right-handed Scalar and Tensor Model: We have enough experimental data available to search for limits on non Standard Model contributions, namely additionally scalar and tensor currents. To restrict the number of parameters, we consider a standard *right-handed scalar and tensor model* [Ero91, Sev06] that establishes the following relations between the coupling constants:

$$\frac{g_V'}{g_V} = 1, \qquad \frac{g_A'}{g_A} = 1, \qquad \frac{g_S'}{g_V} = -\frac{g_S}{g_V}, \qquad \text{and} \qquad \frac{g_T'}{g_A} = -\frac{g_T}{g_A}. \tag{5.10}$$

This corresponds to left-handed couplings for the Standard Model currents and right-handed couplings for possible scalar and tensor admixtures. Starting from the general expressions given in [Glu95], we can calculate the correlation coefficients A, B, a, C^3, and the rate function R_{ft} defined in equation (2.72), in terms of g_V, g_A, g_S, g_T. Here we further assume the constants to be real and that the Fierz interference term b vanishes in equation (2.72):

$$A = -2\,\frac{g_A^2 + g_A g_V + g_S g_T + g_T^2}{g_V + 2g_A^2 + g_S + 3g_T^2} = -2\,\frac{\lambda^2 + \lambda + \lambda xy + \lambda^2 y^2}{1 + 3\lambda^2 + x^2 + 3\lambda^2 y^2} \tag{5.11}$$

$$B = 2\,\frac{g_A^2 - g_A g_V + g_S g_T - g_T^2}{g_V + 2g_A^2 + g_S + 3g_T^2} = 2\,\frac{\lambda^2 - \lambda + \lambda xy - \lambda^2 y^2}{1 + 3\lambda^2 + x^2 + 3\lambda^2 y^2} \tag{5.12}$$

---

[3]The expression for the proton asymmetry C was derived using a relation between A and B (valid in a general VAST-model allowing arbitrary couplings, equation (4.31) in [Glu95]) and a Fierz-term $b = 0$.

$$a = \frac{g_V^2 - g_A^2 - g_S^2 + g_T^2}{g_V + 2g_A^2 + g_S + 3g_T^2} = \frac{1 - \lambda^2 - x^2 + \lambda^2 y^2}{1 + 3\lambda^2 + x^2 + 3\lambda^2 y^2} \tag{5.13}$$

$$C = 4x_C \frac{g_A g_V + g_T^2}{g_V + 2g_A^2 + g_S + 3g_T^2} = 4x_C \frac{\lambda + \lambda^2 y^2}{1 + 3\lambda^2 + x^2 + 3\lambda^2 y^2} \tag{5.14}$$

$$R_{ft} = 2 \frac{g_V^2 + g_S^2}{g_V + 2g_A^2 + g_S + 3g_T^2} = 2 \frac{1 + x^2}{1 + 3\lambda^2 + x^2 + 3\lambda^2 y^2}, \tag{5.15}$$

with $x_C = 0.27484$. For the absence of scalar and tensor couplings ($g_S = g_T = 0$) we get back the $V - A$ equations (2.33). Using relations (5.10), the observables can be described in terms of three free parameters, where λ may be different from the Standard Model value:

$$\lambda = \frac{g_A}{g_V}, \qquad x = \frac{g_S}{g_V}, \qquad \text{and} \qquad y = \frac{g_T}{g_A}. \tag{5.16}$$

Limits on Scalar and Tensor Contributions: Since we are interested in the three parameters λ, $x = \frac{g_S}{g_V}$, and $y = \frac{g_T}{g_A}$, we need at least three measured quantitites as input parameters and studied the following combinations:

1. Electron Asymmetry A, neutrino asymmetry B, and lifetime τ_n, where the latter is related to R_{ft} using equation (2.72) with $ft_{0^+ \to 0^+} = 3072.7(8)$ [Har05] and $f^R = 1.71335(15)$ [Wil82, Abe04]. The situation of 2004, when we started working on this subject, is shown in figure 5.7, the three input parameters are taken from [PDG04].

2. Electron Asymmetry A, neutrino asymmetry B, and proton asymmetry C. For the first time, this data set allows to give constraints based on observables measured with one single instrument: PERKEO II.

3. Electron Asymmetry A, neutrino asymmetry B, and $e\nu$-correlation a.

The exclusion plots are again generated as described in section 5.2, with the contours mapped along the λ-axis onto the xy-plane.

We consider altogether six combinations of input parameters, to take into account the two incompatible lifetimes $\tau_{\text{PDG}} = 885.7(8)$ s and $\tau_{\text{Ser}} = 878.5(8)$ s, and the two electron asymmetry A values: The first is the one suggested by the Particle Data Group,
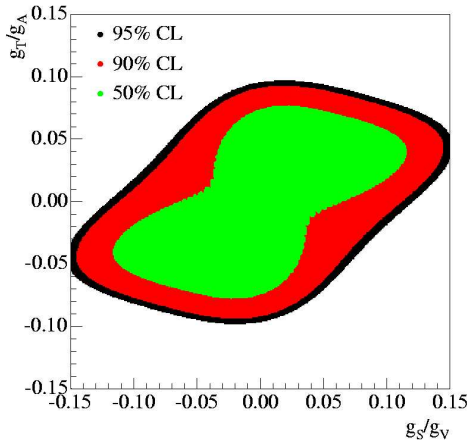

Figure 5.7: Limits on scalar and tensor contributions to the weak interaction, calculated with the average parameters A, B, τ_n of the year 2004 [PDG04], when the work on this thesis was started. Comparison with figure 5.8 directly shows the influence of the newly measured neutrino asymmetry B and its sensitivity to find "new physics". The Standard Model case with $g_S = g_T = 0$ corresponds to the plot center.
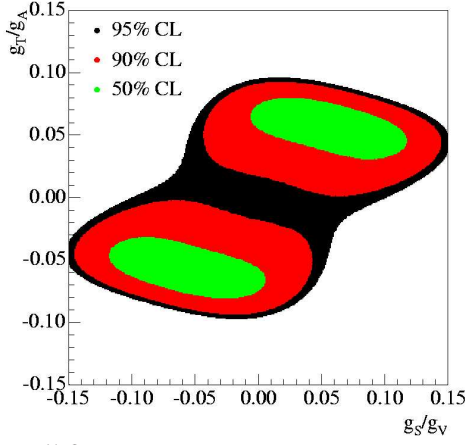
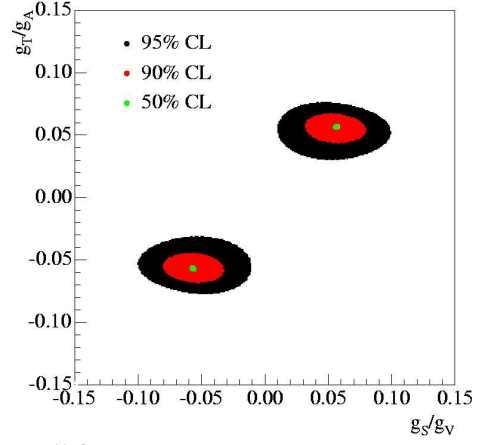Figure 5.8: Constraints on scalar and tensor contributions to the weak interaction, derived from A_{PDG}, B_{mean}, τ_{PDG}.

Figure 5.9: Exclusion plot using A_{PDG}, B_{mean}, and the newly measured neutron lifetime from Serebrov τ_{Ser}, which was published 2005.
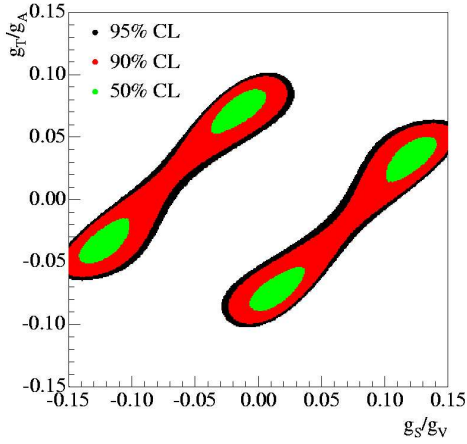
Figure 5.10: Input: A_{PII}, B_{mean}, τ_{PDG}.
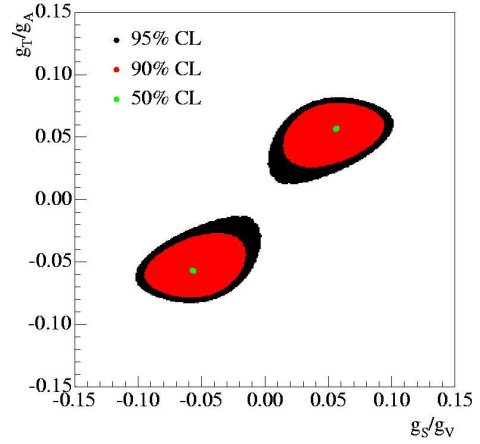
Figure 5.11: Input: A_{PII}, B_{mean}, τ_{Ser}.
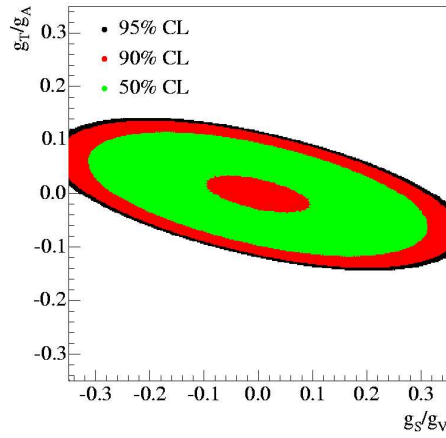
Figure 5.12: Only PERKEO II measurements: A_{PII}, B, and the new proton asymmetry C.
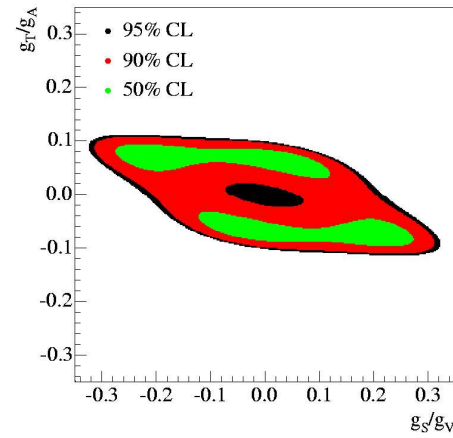
Figure 5.13: Input values: A_{PDG}, B_{mean}, and a. Please note the different scales of the plots.

$A_{\mathrm{PDG}} = -0.1173(13)$, the second only considers PERKEO II measurements with very small corrections: $A_{\mathrm{PII}} = -0.1193(4)$. The corresponding exclusion plots are shown in figures 5.8−5.13 (please note the varying scales), the resulting χ^2-minima and the 90 % confidence level (CL) limits are given below:

1. $\boldsymbol{A}_{\mathrm{PDG}}$, $\boldsymbol{B}_{\mathrm{mean}}$, $\boldsymbol{\tau}_{\mathrm{PDG}}$ (figure 5.8): The plot is very similar to the result published by [Sev06][4], whose limit on g_A/g_V and g_T/g_A is only slightly lower. On the other hand, their constraint on scalar contributions is much better ($|g_S/g_V| < 0.067$). Our result is:

$$
\begin{aligned}
(g_A/g_V)_{\mathrm{min}} &= -1.2705 & 90\%\ \mathrm{CL}:\ -1.2822 < g_A/g_V < -1.2648 \\
(g_S/g_V)_{\mathrm{min}} &= 0.0596 & 90\%\ \mathrm{CL}:\ -0.1444 < g_S/g_V < 0.1444 \\
(g_T/g_A)_{\mathrm{min}} &= 0.0588 & 90\%\ \mathrm{CL}:\ -0.0924 < g_T/g_A < 0.0924.
\end{aligned}
$$

The Standard Model case $g_T = g_S = 0$ is excluded by the 90 % contour in our analysis, wheras it is included in [Sev06]; the positions of minimum χ^2 agree. Since all plots are point symmetric they sometimes show several global minima, but we only give the coordinates of one position.

2. $\boldsymbol{A}_{\mathrm{PDG}}$, $\boldsymbol{B}_{\mathrm{mean}}$, $\boldsymbol{\tau}_{\mathrm{Ser}}$ (figure 5.9): This result, employing the lower neutron lifetime τ_{Ser}, fully excludes the Standard Model and predicts the following limits:

$$
\begin{aligned}
(g_A/g_V)_{\mathrm{min}} &= -1.2765 & 90\%\ \mathrm{CL}:\ -1.2786 < g_A/g_V < -1.2732 \\
(g_S/g_V)_{\mathrm{min}} &= 0.0564 & 90\%\ \mathrm{CL}:\ -0.0796 < g_S/g_V < 0.0796 \\
(g_T/g_A)_{\mathrm{min}} &= 0.0564 & 90\%\ \mathrm{CL}:\ -0.0676 < g_T/g_A < 0.0676.
\end{aligned}
$$

The positions of the global minima almost agree with case 1.

3. $\boldsymbol{A}_{\mathrm{PII}}$, $\boldsymbol{B}_{\mathrm{mean}}$, $\boldsymbol{\tau}_{\mathrm{PDG}}$ (figure 5.10): Here, we employ the mean A-value of all PERKEO II measurements, which is much more precise than A_{PDG}. At the same time, however, it is significantly higher:

$$
\begin{aligned}
(g_A/g_V)_{\mathrm{min}} &= -1.2672 & 90\%\ \mathrm{CL}:\ -1.2834 < g_A/g_V < -1.2639 \\
(g_S/g_V)_{\mathrm{min}} &= 0.0148 & 90\%\ \mathrm{CL}:\ -0.1500 < g_S/g_V < 0.1500 \\
(g_T/g_A)_{\mathrm{min}} &= -0.0732 & 90\%\ \mathrm{CL}:\ -0.0988 < g_T/g_A < 0.0988.
\end{aligned}
$$

Again, the Standard Model is excluded.

4. $\boldsymbol{A}_{\mathrm{PII}}$, $\boldsymbol{B}_{\mathrm{mean}}$, $\boldsymbol{\tau}_{\mathrm{Ser}}$ (figure 5.11): This parameter set uses the PERKEO II A-average, the new mean value for B, and the neutron lifetime of Serebrov. The limits do not include the Standard Model:

$$
\begin{aligned}
(g_A/g_V)_{\mathrm{min}} &= -1.2762 & 90\%\ \mathrm{CL}:\ -1.2795 < g_A/g_V < -1.2735 \\
(g_S/g_V)_{\mathrm{min}} &= 0.0564 & 90\%\ \mathrm{CL}:\ -0.0940 < g_S/g_V < 0.0940 \\
(g_T/g_A)_{\mathrm{min}} &= 0.0564 & 90\%\ \mathrm{CL}:\ -0.0772 < g_T/g_A < 0.0772.
\end{aligned}
$$

---

[4]The authors use more experimental input values from neutron and nuclear decays, whereas we restrict ourselves to neutron decay data only. Please note that they give limits obtained with constant $\chi^2_{\mathrm{min}} + 4$, whereas we use the usual 90 % CL limits: $\chi^2_{\mathrm{min}} + 4.61$

5. A_{PII}, B, C (figure 5.12): All values of this set have been measured by the PERKEO II collaboration using the same instrument. For the first time, we can now give limits on scalar and tensor currents using the proton asymmetry C, since this was previously not known. The results

$$
\begin{aligned}
(g_A/g_V)_{\mathrm{min}} &= -1.263 &\qquad& 90\%\ \mathrm{CL}:\ -1.287 < g_A/g_V < -1.217 \\
(g_S/g_V)_{\mathrm{min}} &= 0.052 &\qquad& 90\%\ \mathrm{CL}:\ -0.366 < g_S/g_V < 0.366 \\
(g_T/g_A)_{\mathrm{min}} &= 0.080 &\qquad& 90\%\ \mathrm{CL}:\ -0.136 < g_T/g_A < 0.136
\end{aligned}
$$

agree with the Standard Model and with the absence of scalar and tensor contributions.

6. A_{PDG}, B_{mean}, a (figure 5.13): In a final step, we examine the sensitivity of the electron-neutrino correlation $a = -0.103(4)$ [PDG06] on g_S and g_T. The Standard Model is again only included at 95 % confidence level, but the constraints are not very precise:

$$
\begin{aligned}
(g_A/g_V)_{\mathrm{min}} &= -1.2462 &\qquad& 90\%\ \mathrm{CL}:\ -1.2789 < g_A/g_V < -1.2243 \\
(g_S/g_V)_{\mathrm{min}} &= 0.216 &\qquad& 90\%\ \mathrm{CL}:\ -0.312 < g_S/g_V < 0.312 \\
(g_T/g_A)_{\mathrm{min}} &= -0.076 &\qquad& 90\%\ \mathrm{CL}:\ -0.108 < g_T/g_A < 0.108.
\end{aligned}
$$

Summary: Due to the unclear situation regarding the neutron lifetime, the current situation in neutron decay is best described by figure 5.14 showing the confidence levels for the following input parameter set: $\tau_{\mathrm{mean}} = 882.0(1.4)$ s, $A_{\mathrm{PII}} = -0.1193(4)$, $B_{\mathrm{mean}} = 0.9807(30)$, $C = -0.2377(36)$, $a = -0.103(4)$, where the lifetime error was scaled by 2.5. The limits are:

$$
\begin{aligned}
(g_A/g_V)_{\mathrm{min}} &= -1.2711 &\qquad& 90\%\ \mathrm{CL}:\ -1.2816 < g_A/g_V < -1.2663 \\
(g_S/g_V)_{\mathrm{min}} &= -0.0188 &\qquad& 90\%\ \mathrm{CL}:\ -0.1300 < g_S/g_V < 0.1300 \\
(g_T/g_A)_{\mathrm{min}} &= -0.0660 &\qquad& 90\%\ \mathrm{CL}:\ -0.0948 < g_T/g_A < 0.0948.
\end{aligned}
$$

The Standard Model case, $g_S = g_T = 0$, is included in the 90 % confidence region, however, even more precise input data is needed to make stronger statements. Especially the solution of the neutron lifetime puzzle is very urgent.

The neutron decay results for tensor interactions are almost as precise as the best limits so far [Sev06]. For scalar couplings, our constraints are much less stringent. However, the existence of scalar currents seems to be almost ruled out by an analysis of ft values from several superallowed β-decays: Assuming CVC hypothesis, the limit is $|g_S/g_V| \leq 0.0013$ [Har05b].
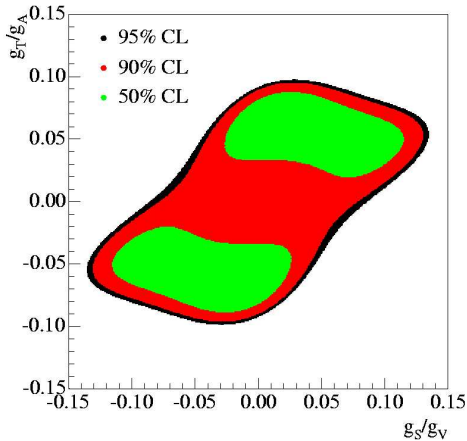

Figure 5.14: Exclusion plot based on the neutron decay parameters A_{PII}, B_{mean}, C, a, and τ_{mean}. The uncertainty of the lifetime τ has been scaled by 2.5 to account for the unclear experimental situation when all measurements are considered. The Standard Model $g_S = g_T = 0$ is included in the 90 % confidence region.

Chapter 6

Summary and Outlook

Correlation coefficients (or asymmetries) in the decay of polarized neutrons relate neutron spin and momenta of the decay products. Their determination with high precision is important to check the Standard Model of Particle Physics and to search for possible hints on "new physics".

Within the framework of this thesis, we have measured the neutrino asymmetry B, the correlation between neutron spin and neutrino momentum, and the proton asymmetry C relating neutron spin and proton momentum. For this purpose, the electron spectrometer PERKEO II was installed at the high flux reactor of the Institut Laue-Langevin (ILL) in Grenoble, France. It was equipped with a sophisticated combined electron-proton detector that allows to measure both particles with the same detector, regardless of their energy difference of three orders of magnitude. The coincident detection of electron and proton is neccessary to determine the neutrino momentum direction which cannot be detected directly in our setup.

Both quantities were measured successfully. The resulting uncertainty of the neutrino asymmetry B is similar to the most precise measurement. Corrections to the value are small, what is an important feature of the PERKEO II spectrometer. In case of the proton asymmetry, we performed the first precision measurement at all. All values agree with previous measurements or Standard Model expectations, and the new results lower the uncertainties of the mean values considerably: The neutrino asymmetry error decreases by 25 %, and the proton asymmetry precision was improved by more than a factor of 3.

Standard Model tests were performed with the new average values: In particular, we examined experimental neutron decay data in order to obtain limits on right-handed admixtures to the weak interaction and on additional scalar and tensor couplings. Due to the unclear situation regarding neutron lifetime, where two incompatible values exist, it is very difficult to give final constraints, since the different values change the results considerably. In all studied cases within the manifest left-right-symmetric model, the Standard Model case is not included in the 90 % confidence level contour, however, we do not consider this deviation to be significant. Future evaluations based on even more precise data with low corrections will have to show if this might be a trace of new physics.

The same holds for limits on possible scalar and tensor couplings: Depending on the parameters used, the results change significantly, and again more precise and consistent observables from neutron decay experiments are needed to clarify the situation. Currently, the general

trend also does not include the Standard Model case within 90 % confidence level, except when only results measured with PERKEO II are used. With the new C-value, a Standard Model test was performed that was not possible before: We can now give constraints on scalar and tensor contributions derived from observables measured with one single instrument, PERKEO II.

6.1   Statistical and systematical Limits

The experiment to measure the asymmetries was limited by several factors. Some of them are "intrinsic", i.e. they arise due to setup, method, or components chosen for the measurement. However, we also had to face "unforeseen" limits: These were not expected and still cannot be fully explained, but they contribute significantly to the overall precision. In this section, we want to summarize the limiting factors:

- The most severe systematic limit on B_{same}, generated from events where electron and proton are measured in the same detector, is the uncertainty due to the imprecisely known displacement between neutron beam and magnetic field maximum. It results in an asymmetry shift, since the magnetic mirror effect is then different for the two detectors. This limit was unforeseen: It only occured because the detectors did not obtain results of the same statistical significance. Normally, the effect cancels when the asymmetries of both detectors are averaged.

  The virtual loss of the second detector was probably due to the quality of the thin carbon foil on high voltage used to accelerate the protons to detectable energies. However, the exact reason is still unknown, although many tests to improve its performance have been performed during the experiment. Therefore, we cannot conclude that this limit should be absent in another experiment of this type. Possibly, one could replace the carbon foils by ultrathin polyimide to improve the stability of the proton detector [Hoe06].

- B_{same} is still limited by statistics, however, improving this should be no problem since statistics was decreased to minimize the displacement effect. If a second detector is available, statistics is doubled anyway.

- The neutrino asymmetry B_{opp}, where electron and proton are measured in opposite detectors, suffers from electron detector calibration. Solely the detetcor gain could be measured to a quite high accuracy (0.5 %), the energy offset was only known on the $5-10$ % level, imposing uncertainties in the percent range on B_{opp}. B_{same} does virtually not depend on energy calibration, whereas the proton asymmetry uncertainty is dominated by detector calibration as well.

  We made an effort to obtain calibration as precisely as possible. No preceding PERKEO experiment examined the detector response function to this extend: We used six conversion electron peaks for calibration and additionally made three two-dimensional detector scans with a high spatial resolution. Anyhow, we are still limited by detector calibration. Using an electron gun to analyze the low energetic part of the spectrum could possibly improve the situation.

- Statistics is the second large contribution to the error of B_{opp}, whose statistical sensitivity is highest at small energies. However, this region cannot be used for fits since it shows a non-linear detector calibration, and high voltage induced background effects occur. Whereas these effects might be improved, undetected electron backscattering changing the asymmetries will always be present below 200 keV as long as standard plastic scintillators are used.

These are the main sources of uncertainty for the present measurement. Accidential coincidences and coincident after pulses from single photomultipliers that limited the previous B-measurement with PERKEO II [Kre04b, Kre05b] are not important anymore. They were suppressed by detecting many stops in the coincidence window, and by requiring a signal of at least two photomultipliers to generate a trigger.

6.2 The Future: PERKEO III and new Instruments

PERKEO IIB, the experiment presented in this thesis, was the last using the electron spectrometer PERKEO II. In almost 12 years, altogether five measurements were performed, three on the electron asymmetry, and two to obtain neutrino and proton asymmetry in a coincidence setup.

The new instrument of the collaboration, PERKEO III, is shown in figure 6.1. It is much larger than its predecessor – the decay volume has a length of about 2.5 m – to gain statistics and to make measurements with a chopped neutron beam possible. This further reduces
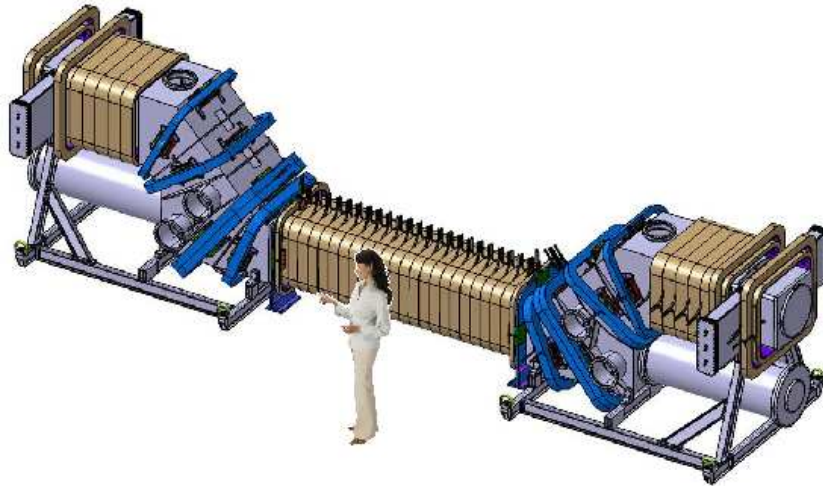
Figure 6.1: Illustration of the new instrument PERKEO III: With an overall length of almost 8 m and a decay volume of 2.5 m, it is much larger compared to PERKEO II. In this way, statistics is increased by two orders of magnitude. However, coincidence measurements are not longer possible due to the much longer proton drift times. Longitudally polarized neutrons enter the spectrometer through beam tubes attached to the lower part. The magnetic field of the central solenoid housing the decay volume defines two hemispheres in and against flight direction. The detectors are placed at the ends of the higher part.

the beam related background, one of the limiting factors in A-measurements so far. The dramatically increased decay rate of about 30 kHz allows direct access to small induced terms and corrections in neutron decay for the first time. An example for such a quantity is the weak magnetism ("induced tensor") form factor f_2. Its existence is predicted by the conserved vector current hypothesis (CVC) but has never been verified in neutron decay. The first measurement with PERKEO III will be done to obtain a value for f_2 [Mae06].

Within the time scale of a couple of years, the next child of the PERKEO family shall be developed and built. It is planned that it will use a neutron guide as decay volume and deliver decay products instead of neutrons to the experiment [Dub07]. With this approach, even higher count rates can be achieved allowing to measure quantities like correlations with the spin of the decay electrons.

However, both new instruments have something in common: It will not be possible to make coincidence measurements, since event rate and proton drift times are much too high to permit a proper assignment of a proton to an electron. Therefore, the measurement of the neutrino asymmetry B, presented in this thesis, was the last coincidence measurement of the PERKEO collaboration for the next years.

Bibliography

[Aba96] S. Abachi et al. (D∅ collaboration), Phys. Rev. Lett. **76**, 3271 (1996)

[Aba04] V. Abazov et al. (D∅ collaboration), Phys. Rev. D **69**, 111101R (2004)

[Abe97] H. Abele et al., Phys. Lett. B **407**, 212 (1997)

[Abe98] H. Abele, habilitation thesis, University of Heidelberg 1998

[Abe02] H. Abele et al., Phys. Rev. Lett. **88**, 21 (2002)

[Abe04] H. Abele et al., Eur. Phys. J. C **22**, 1 (2004)

[Abe05] H. Abele et al., J. Res. Natl. Inst. Stand. Technol. **110**, 377 (2005)

[Abe06] H. Abele et al., Nucl. Instr. Meth. A **562**, 407 (2006)

[And04] S. Ando et al., Phys. Lett. B **595**, 250 (2004)

[Ang98] A. Angelopoulos et al. (CPLEAR collaboration), Phys. Lett. B **444**, 43 (1998)

[Arz00] S. Arzumanov et al., Phys. Lett. B **483**, 15 (2000)

[Aul97] C. S. Aulakh, K. Benakli, G. Senjanović, hep-ph/9703434 (1997)

[Bab06] K. S. Babu, C. Kolda: *The W′ Searches* in [PDG06] (2006)

[Bae96] S. Baeßler, PhD thesis, University of Heidelberg 1996

[Bae03] S. Baeßler et al. in *Quark-Mixing, CKM-Unitarity*, Mattes Verlag, Heidelberg 2003

[Bar95] J. Baro et al., Nucl. Instr. Meth B **100**, 31 (1995)

[Bar97] G. Barenboim et al., Phys. Rev. D **55**, 4213 (1997)

[Bar02] G. Barenboim et al., Phys. Rev. D **65**, 095003 (2002)

[Baz93] A. N. Bazhenov et al., Nucl. Instr. Meth. **332**, 534 (1993)

[Beg77] M. A. B. Bég et al, Phys. Rev. Lett **38**, 1252 (1977)

[Bra00] B. Brand, diploma thesis, University of Heidelberg 2000

[Bre03] M. Brehm, diploma thesis, University of Heidelberg 2003

[Bun06] G. C. Bunatian, hep-ph/0311350 (2006)

[Chr64] J. H. Christensen et al., Phys. Rev. Lett. **13**, 138 (1963)

[Chr70] C. J. Christensen, V. E. Krohn, G. R. Ringo, Phys. Rev. C **1**, 1693 (1970)

[Dei05] M. Deissenroth, diploma thesis, University of Heidelberg 2005

[Dob75] R. Dobrozemsky et al., Phys. Rev. D **11**, 510 (1975)

[Doe90] J. Döhner, PhD thesis, University of Heidelberg 1990

[Dub07] D. Dubbers, talk at workshop *Precision Measurements at Low Energies*, Paul Scherrer Institut (2007)

[Ero70] B. G. Erozolimsky et al., Phys. Lett. B **33**, 351 (1970)

[Ero91] B. G. Erozolimsky, Y. A. Mostovoi, Sov. J. Nucl. Phys. **53**, 260 (1991)

[Fey58] R. P. Feynman, M. Gell-Mann, Phys. Rev. **109**, 193 (1958)

[Fuk03] M. Fukugita, T. Yanagida: *Physics of Neutrinos*, Springer, Heidelberg, 2003

[Glu95] F. Glück, I. Joó, J. Last, Nucl. Phys. A **593**, 125 (1995)

[Glu96] F. Glück, Phys. Lett. B **376**, 25 (1996)

[Glu98] F. Glück, Phys. Lett. B **436** (1998)

[Glu03] F. Glück in *Quark-Mixing, CKM-Unitarity*, Mattes Verlag, Heidelberg 2003

[Glu05] F. Glück, private communication

[Gro90] K. Grotz, H. V. Klapdor: *The Weak Interaction in Nuclear, Particle and Astrophysics*, Adam Hilger, Bristol 1990

[Hae02] H. Häse et al., Nucl. Instr. Meth. A **458**, 453 (2002)

[Har05] J. C. Hardy, I. S. Towner, Phys. Rev. C **71**, 055501 (2005)

[Har05b] J. C. Hardy, I. S. Towner, Phys. Rev. Lett. **94**, 092502 (2005)

[Hoe06] S. A. Hoedl et al., J. Appl. Phys. **99**, 084904 (2006)

[Hol77] B. R. Holstein, S. B. Treiman, Phys. Rev. D **16**, 1369 (1977)

[Jac57] J. D. Jackson et al., Phys. Rev. **106**, 517 (1957)

[Jac02] J. D. Jackson: *Klassische Elektrodynamik*, de Gruyter, Berlin 2002

[Kra66] D. E. Kraus, F. A. White, IEEE Trans. Nucl. Sci. **13**, 765 (1966)

[Kre99] M. Kreuz, diploma thesis, University of Heidelberg 1999

[Kre04] J. Krempel, diploma thesis, University of Heidelberg 2004

[Kre04b] M. Kreuz, PhD thesis, University of Heidelberg 2004

[Kre05] M. Kreuz et al., Nucl. Instr. Meth. A **547**, 583 (2005)

[Kre05b] M. Kreuz et al., Phys. Lett. B **619**, 263 (2005)

[Kuz95] I. A. Kuznetsov, Phys. Rev. Lett. **75**, 794 (1995)

[Lee56] T. D. Lee, C. N. Yang, Phys. Rev. **104**, 254 (1956)

[Leo94] W. R. Leo: *Techniques for Nuclear and Particle Physics Experiments*, Springer, Heidelberg 1994

[Lon80] M. A. Lone et al., Nucl. Instr. Meth. **174**, 521 (1980)

[Lue54] G. Lüders, Dan. Mat. Fys. Medd. **28**, 5 (1954)

[Mae05] B. Märkisch, private communication

[Mae06] B. Märkisch, PhD thesis, University of Heidelberg 2006

[Mar03] J. W. Martin et al., Phys. Rev. C **68**, 055503 (2003)

[May94] T. Mayer-Kuckuk: *Kernphysik*, Teubner, Stuttgart, 1994

[Met95] C. Metz, diploma thesis, University of Heidelberg 1995

[Moh75] R. N. Mohapatra, J. C. Pati, Phys. Rev. D. **11**, 566 (1975)

[Mue96] T. Müller, diploma thesis, University of Heidelberg, 1996

[Mun06] D. Mund, PhD thesis, University of Heidelberg 2006

[Nac86] O. Nachtmann: *Elementarteilchenphysik*, Vieweg, Braunschweig 1986

[NDB02] A. Dianoux et al.: *Neutron Data Booklet*, ILL 2002

[Nuc95] G. Pfennig et al.: *Chart of the nuclides*, Forschungszentrum Karlsruhe 1995

[Pat74] J. C. Pati, A. Salam, Phys. Rev. D **10**, 275 (1974)

[PDG04] Particle Data Group, S. Eidelman et al., Phys. Lett. B **592**, 1 (2004)

[PDG06] Particle Data Group, W.-M. Yao et al., J. Phys. G **33** (2006) 1

[Plo00] C. Plonka, diploma thesis, University of Heidelberg 2000

[Rav95] C. Raven, diploma thesis, University of Heidelberg 1995

[Rei99] J. Reich, PhD thesis, University of Heidelberg 1999

[Sch89] O. Schärpf, N. Stuesser, Nucl. Instr. Meth. **248** (1989)

[Sch95] P. Schmüser: *Feynman Graphen und Eichtheorien für Experimentalphysiker*, Springer, Heidelberg 1995

[Sch04] M. Schumann, diploma thesis, University of Heidelberg 2004

[Ser98] A. Serebrov et al., JETP **86**, 1074 (1998)

[Ser05] A. Serebrov et al., Phys. Lett. B **605**, 72 (2005)

[Sev06] N. Severijns, M. Beck, O. Naviliat-Cuncic, Rev. Mod. Phys. **78**, 991 (2006)

[Sir67] A. Sirlin, Phys. Rev. **164**, 1767 (1967)

[Sol05] T. Soldner, private communication

[Spe06] D. N. Spergel et al., astro-ph/0603449 (2006)

[Sto02] A. Stolarz, P. Maier-Komor, Nucl. Instr. Meth. A **480**, 194 (2002)

[Str78] C. Stratowa et al., Phys. Rev. D **18**, 3970 (1978)

[Sur97] R. Surkau et al., Nucl. Instr. Meth. A **384**, 444 (1997)

[Tay97] J. R. Taylor: *An introduction to error analysis*,
         University Science Books, Sausalito 1997

[Tow98] I. S. Towner, J. C. Hardy in *Physics beyond the Standard Model*,
         World Scientific, 1998

[Wie05] F. E. Wietfield et al., Nucl. Instr. Meth. A **545**, 181 (2005)

[Wil82] D. H. Wilkinson, Nucl. Phys. A **377**, 474 (1982)

[Wu57] C. S. Wu et al., Phys. Rev. **105**, 1413 (1957)

[Zim99] O. Zimmer, Phys. Lett. B **461**, 307 (1999)

Impressions

Acknowledgements